Nano-Optical Studies of Superconducting Nanowire Single-Photon Detectors

John Alexander O'Connor MSc, BSc (Hons)

Submitted for the degree of
Doctor of Philosophy

Heriot-Watt University
School of Engineering and Physical Sciences
November 2011

Abstract

Superconducting single-photon detectors based on superconducting nanowires offer broadband single-photon sensitivity, from visible to mid-infrared wavelengths. They have attracted particular attention due to their promising performance at telecommunications wavelengths. The additional benefits of superconducting nanowire single-photon detectors (SNSPDs) include low dark count rates (Hz) and low timing jitter (sub 100 ps). SNSPDs have been employed in practical photon-counting applications such as quantum key distribution (QKD), operation of quantum waveguide circuits and quantum emitter characterisation. Major challenges in the development of SNSPDs are the improvement of device uniformity and achieving efficient optical coupling. Nano-optical techniques such as confocal microscopy can be used to image localised areas of SNSPDs providing a direct measurement of the device uniformity. The work in this thesis describes both initial nano-optical testing at visible wavelengths in liquid helium and the construction of a fibre based miniature confocal microscope configuration operating at telecommunications wavelengths for use in a closed cycle refrigerator. In both cases localised areas of SNSPDs can be studied whilst maintaining efficient optical coupling. The miniature confocal microscope configuration has sub-nanometre position resolution over a 30 μm x 30 μm area by way of a piezoelectric X-Y scanner. A full width at half maximum (FWHM) optical resolution of 1305 nm at a wavelength of 1550 nm is achieved. SNSPDs based upon niobium nitride (NbN) nanowires fabricated on magnesium oxide (MgO) have been studied. The microscope system has allowed us to map the temporal response (timing jitter and output pulse timing delay) of constricted (non-uniform) SNSPDs. By fitting to a theoretical model, the variations in output pulse timing delay have been shown to be caused by variations in hotspot resistances across the device. This observation has provided insights into the underlying physics of SNSPDs and especially the origins of timing jitter in SNSPDs. This provides a pathway to exploitation of this effect in next-generation device designs for applications such as imaging.

Acknowledgements

First and foremost, I would like to thank my supervisor *Dr Robert Hadfield*, for all of the motivation, help and support that he provided during my PhD. His enthusiasm, inspiration, and guidance played the most significant role in improving my skills as a scientist and individual, while making the PhD experience enjoyable. Without his input I would not have achieved the success I have. For this I am eternally grateful.

I am indebted to *Professor Richard Warburton* for the useful discussions, help and motivation provided at the start of my PhD. The help and initial training I received from *Dr Paul Dalgarno* was invaluable for my improvement as a researcher. I also thank him for the many hours of discussions on music and Formula 1 during the many hours of experiments in his lab.

I would like to thank the three colleagues that I worked closely with during my PhD, *Dr Mike Tanner, Dr Chandra Mouli Natarajan* and *Catherine Fitzpatrick*. We had many astute and interesting discussions and I am grateful for the help, support and contribution to my thesis.

Professor Gerald Buller has my gratitude for useful discussions of my work and for allowing regular access to his TCSPC card which was invaluable for my thesis.

I am grateful to *Dr Burm Baek* and *Dr Sae Woo Nam* (NIST, USA) for their invaluable advice, knowledge and discussions of various issues and understanding that I encountered during my PhD. I would also like to thank *Dr Shigehito Miki* and *Dr Zhen Wang* (NICT, Japan) for providing the SNSPD chips that have been presented in this thesis.

I also thank the members of both the physics and electronics workshops at Heriot-Watt University, in particular *Peter Heron*, *Mark Stewart* and *Andrew Haston* for their expertise in machining and building the parts required for completion of my thesis work.

To the football guys, *Dan R, Dan B, Flo, Jon, John McC, Dave, Tao, Krystian, Rainer, Henry, Aongus, Patrick, Rob* and all the others not mentioned, Friday lunchtimes provided some fun and exercise which was always enjoyable.

Finally I thank my family for the encouragement and support provided during my University career.

ACADEMIC REGISTRY
Research Thesis Submission

Name*:*	John Alexander O'Connor		
School/PGI:	Engineering and Physical Sciences - Physics		
Version: *(i.e. First, Resubmission, Final)*	Final	Degree Sought (Award **and** Subject area)	PhD Physics

Declaration

In accordance with the appropriate regulations I hereby submit my thesis and I declare that:

1) the thesis embodies the results of my own work and has been composed by myself
2) where appropriate, I have made acknowledgement of the work of others and have made reference to work carried out in collaboration with other persons
3) the thesis is the correct version of the thesis for submission and is the same version as any electronic versions submitted*.
4) my thesis for the award referred to, deposited in the Heriot-Watt University Library, should be made available for loan or photocopying and be available via the Institutional Repository, subject to such conditions as the Librarian may require
5) I understand that as a student of the University I am required to abide by the Regulations of the University and to conform to its discipline.

* *Please note that it is the responsibility of the candidate to ensure that the correct version of the thesis is submitted.*

Signature of Candidate*:*		Date:	

Submission

Submitted By *(name in capitals):*	
Signature of Individual Submitting:	
Date Submitted:	

For Completion in the Student Service Centre (SSC)

Received in the SSC by *(name in capitals):*			
Method of Submission *(Handed in to SSC; posted through internal/external mail):*			
E-thesis Submitted (mandatory for final theses)			
Signature:		Date:	

Contents

List of Tables

List of Figures

Glossary

Roman Symbols

C	Capacitance
d	Optical Resolution using NSOM
E	Energy of a Single Photon
e	Charge of an Electron
g	Acceleration due to gravity
$g^{(2)}(0)$	Second Order Correlation Function
h	Planck's Constant
I	Current
I_c	Critical Current
J_c	Current Density
k_B	Boltzmann's Constant
L	Inductance
L_k	Kinetic Inductance
N	Number of Normalised Energy States
NA	Numerical Aperture
n	Refractive Index
n_i	Refractive Index of SIL
n_0	Refractive Index of Air
R	Radius of Sphere
T_c	Transition Temperature
V	Voltage
X	Depth of Surface of Study
z	Distance along Optical Axis
z_R	Rayleigh Range

Greek Symbols

Δ	Energy Gap in a Superconductor
Δt	Timing Jitter
ξ	Superconducting Coherence Length
λ	Wavelength
v	Frequency
v_f	Fermi Velocity
τ	Output Pulse Timing Delay
ω_D	Lattice Vibration Frequency
$\omega(z)$	Illuminated Spot Size
ω_0	Beam Waist

Acronyms

AFM	Atomic Force Microscopy
AC	Alternating Current
BB84	Bennett-Brassard 84 QKD protocol
BCS	Bardeen, Cooper and Schrieffer theory of superconductivity
BK7	Type of glass
CCD	Charge Coupled Device
COW	Coherent One Way QKD protocol
CPW	Coplanar Waveguide
CW	Continuous Wave
DC	Direct Current
DCR	Dark Count Rate
DE	Detection Efficiency
e-beam	Electron Beam
FWHM	Full Width as Half Maximum
GM	Gifford-McMahon
GRIN	Graded Index
I-V	Current – Voltage
IPA	Isopropanol

IR	Infrared
ITO	Indium Tin Oxide
KID	Kinetic Inductance Detector
LiHe	Liquid Helium
LNA	Low Noise Amplifier
MCP	Multi Channel Plate
MIT	Massachusetts Institute of Technology (USA)
NICT	National Institute of Information and Communications Technology (Japan)
NIST	National Institute of Standards and Technology (USA)
NSOM	Near-field Scanning Optical Microscopy
PMT	Photomultiplier Tube
PPG	Pulse Pattern generator
PSPICE	Personal Simulation Program with Integrated Circuit Emphasis
PT	Pulse Tube
Q-cavity	Quality Factor of a Cavity
QBER	Quantum Bit Error Rate
QKD	Quantum Key Distribution
$R_{hotspot}$	Resistance of a Hotspot
RIE	Reactive Ion Etching
SIL	Solid Immersion Lens
SLD	Super Luminescent Diode
SMF	Single Mode Fibre
SNSPD	Superconducting Nanowire Single-Photon Detector
SPAD	Single-Photon Avalanche Diode
STJ	Superconducting Tunnel Junction
TCSPC	Time Correlated Single-Photon Counting
TES	Transition Edge Sensor
TRPL	Time Resolved Photo Luminescence
ZEP 520	Positive Photo Resist

List of Publications by the Candidate

Journals

P. J. Clarke, R. J. Collins, P. A. Hiskett, M. J. García-Martínez, N. J. Krichel, A. McCarthy, M. G. Tanner, **J. A. O'Connor**, C. M. Natarajan, S. Miki, M. Sasaki, Z. Wang, M. Fujiwara, I. Rech, M. Ghioni, A. Gulinatti, R. H. Hadfield, P.D. Townsend, and G.S. Buller, *Analysis of detector performance in a gigahertz clock rate quantum key distribution system.* New Journal of Physics, 2011. **13**(7): p. 075008.

J. A. O'Connor, M.G. Tanner, C.M. Natarajan, G.S. Buller, R.J. Warburton, S. Miki, Z. Wang, S.W. Nam, and R.H. Hadfield, *Spatial dependence of output pulse delay in a niobium nitride nanowire superconducting single-photon detector.* Applied Physics Letters, 2011. **98**(20): p. 201116-3.

M. G. Tanner, C.M. Natarajan, V.K. Pottapenjara, **J.A. O'Connor**, R.J. Warburton, R.H. Hadfield, B. Baek, S. Nam, S.N. Dorenbos, E.B. Urena, T. Zijlstra, T.M. Klapwijk, and V. Zwiller, *Enhanced telecom wavelength single-photon detection with NbTiN superconducting nanowires on oxidized silicon.* Applied Physics Letters, 2010. **96**(22): p. 221109.

K. A. Serrels, E. Ramsay, P.A. Dalgarno, B.D. Gerardot, **J.A. O'Connor**, R.H. Hadfield, R.J. Warburton, and D.T. Reid, *Solid immersion lens applications for nanophotonic devices.* Journal of Nanophotonics, 2008. **2**: p. 021854

R. H. Hadfield, P.A. Dalgarno, **J.A. O'Connor**, E. Ramsay, R.J. Warburton, E.J. Gansen, B. Baek, M.J. Stevens, R.P. Mirin, and S.W. Nam, *Submicrometer photoresponse mapping of nanowire superconducting single-photon detectors.* Applied Physics Letters, 2007. **91**(24): p. 241108.

Conference Proceedings

J. A. O'Connor, P.A. Dalgarno, M.G. Tanner, R.J. Warburton, R.H. Hadfield, B. Baek, S.W. Nam, S. Miki, Z. Wang, and M. Sasaki, *Nano-opticalsStudies of superconducting nanowire single photon detectors,* in *Quantum Communication and Quantum Networking*, O. Akan, et al., Editors. 2009, Springer Berlin Heidelberg. p. 158-166.

R. H. Hadfield, P.A. Dalgarno, **J.A. O'Connor**, E.J. Ramsay, R.J. Warburton, E.J. Gansen, B. Baek, M.J. Stevens, R.P. Mirin, and S.W. Nam, *Nano-optical studies of superconducting nanowire single-photon detectors*, in Proc. SPIE Vol 7236, 723604-1, *Quantum Communications Realized Ii*, Y. Arakawa, M. Sasaki, and H. Sotobayashi, Editors. 2009.

B. Baek, E.J. Gansen, M.J. Stevens, R.P. Mirin, S.W. Nam, R.H. Hadfield, P.A. Dalgarno, **J.A. O'Connor**, E. Ramsay, R.J. Warburton, and IEEE, *Investigation of local photon detection efficiency distributions in nanowire superconducting single-photon detectors*. 2008 Conference on Lasers and Electro-Optics & Quantum Electronics and Laser Science Conference, Vols 1-9. 2008, New York: IEEE. 3233-3234.

Chapter 1 Introduction

1.1 Introduction

Single-photon detectors have emerged as a key enabling technology for many applications at the forefront of science and technology [1] ranging from quantum information processing [2, 3], quantum key distribution (QKD) [4-6], time of flight ranging [6-8], and quantum emitter characterisation [9-11] to high speed communication [12-14]. The energy of a single photon (E) is defined as the product of Planck's constant (h) and the frequency of the photon (v). Typical photodetectors cannot detect a single incident visible or infrared photon due to the low photon energy. The detectors lack the sensitivity to distinguish the signal from the detected single-photon above the noise level.

A perfect single-photon detector provides an electrical signal upon the absorption of a single photon without any ambiguity. In practice real single-photon detectors have imperfect characteristics. Detection efficiency (DE) of single-photon detectors is typically well below 100 %. This can be caused by many factors including the loss of photons in the optical system due to absorption, scattering and reflections and the single-photon detector not producing an electrical signal for every absorbed photon. Electrical noise and stray light in the experimental system can cause false detection events that simulate the detection of an incident photon. These erroneous detection events are known as dark counts [15, 16]. Research in the field of single-photon detectors has not only improved the characteristics of single-photon detectors but also the techniques used to study them. Time Correlated Single-Photon Counting (TCSPC) is probably the most powerful technique used. TCSPC is the detection of single-photons and the measurement of their arrival time with respect to a reference signal. This is repeated a significant number of times to allow precise statistics to be obtained. TCSPC allows the temporal response of the complete experimental system to be measured (see Figure 1.1). An electrical pulse is synchronised with a pulsed source of photons. The electrical pulse in each clock cycle is sent to the TCSPC electronics, acting as the "start" trigger. The photon synchronised with this electrical pulse is emitted into the experimental system. The electrical pulse generated by the detection of

the photon by the single-photon detector provides a "stop" trigger for the TCSPC electronics. The arrival of the count events versus the relative timing delay is plotted as a histogram. Modern TCSPC electronics allow high timing resolution to be achieved by time binning down to 4 ps. This method minimises the contribution of randomly occurring dark counts. The full width at half maximum (FWHM) of the histogram is typically chosen to benchmark the timing jitter of the experimental system. Knowing the timing jitter of each of the components in the experimental system allows the timing jitter of the single-photon detector to be found.

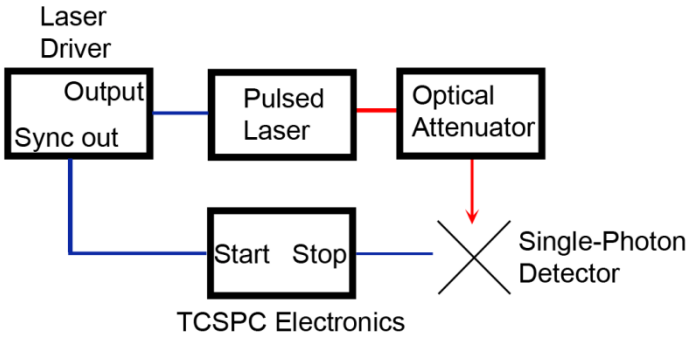

Figure 1.1 – A time correlated single-photon counting (TCSPC) setup.

The TCSPC technique was initially developed to be used with photomultiplier tube (PMT) single-photon detectors [17, 18]. With advances in semiconductor technology, commercially available silicon (Si) single-photon avalanche diodes (SPADs) [19, 20] have superseded PMTs in many applications. Si – SPADs are a mature technology that works well at visible and near infrared (NIR) wavelengths. 45 % *DE* at λ = 800 nm is common [21]. Many important applications are limited by the performance of commercially available single-photon detectors. Improved single-photon detectors at telecommunications wavelengths (λ = 1310 nm and λ = 1550 nm) would be highly desirable for applications such as quantum key distribution (QKD) [4, 22, 23], quantum emitter characterisation, and time of flight ranging. The telecommunications industry has invested heavily in the development of practical and inexpensive optical components at λ =1550 nm. One of the most significant benefits for moving to λ = 1550 nm is the commercial availability of low-loss optical fibres, with typically 0.2 dB/km loss [24].

Single-photon detectors at λ = 1550 nm with high *DE* and low dark count rates are essential for the realization of advanced photon counting experiments at

telecommunications wavelengths. Significant effort has been invested in exploring lower bandgap semiconductor materials (Ge, InGaAs) for SPADs [25, 26] at telecommunications wavelengths. At present, the performance of the best commercially available InGaAs SPADs for telecommunications wavelengths falls far short of that achieved by Si SPADs in the visible. Single-photon detectors based upon superconducting materials have the potential to improve on semiconductor based single-photon detectors at λ = 1550 nm. In principle they offer single-photon sensitivity ranging from X-ray to THz frequencies. The most promising superconducting single-photon detector is based upon a superconducting nanowire of niobium nitride (NbN) and was first presented in 2001 [27]. This superconducting nanowire single-photon detector (SNSPD) operates at ~ 4 K (achievable using liquid helium or modern closed cycle refrigeration technology [28]) and provides single-photon detection with picosecond timing resolution and low dark counts at infrared wavelengths. Many research groups worldwide are now working on the development and exploitation of SNSPDs, leading to rapid advances in the field. More complex and sophisticated SNSPD designs have yielded impressive results. SNSPDs integrated with optical cavities have been reported with intrinsic *DE* of 57 % at λ = 1550 nm [29]. The timing jitter of SNSPDs is excellent. Sub 100 ps FWHM jitter can be routinely achieved and jitter as low as 29 ps FWHM [30, 31] has been reported. The advantages of SNSPDs over semiconductor based SPADs at telecommunication wavelengths show that they are one of the most promising single-photon detector technologies for infrared photon counting applications.

The most common method of efficiently delivering light to SNSPDs is by fibre-coupling. This provides broad illumination (illuminated spot ~ 10s of μm) of the SNSPD and allows the overall properties of the SNSPD to be measured. Fibre-coupling requires precise alignment to the SNSPD and the spacing between the end of the optical fibre and the SNSPD is required to be small so that the light emerging from the fibre does not significantly diverge reducing the *DE* of the SNSPD. The use of lensed or tapered fibres allows for a more tightly confined illuminated spot (~ 3 μm); this still only allows the overall properties of the SNSPD to be investigated. To understand the underlying physics and localised properties of SNSPDs, local illumination is required. Nano-optical techniques utilising microscopy methods and novel optical components

provide a pathway to carry out such studies. A microscopy technique based upon confocal microscopy is a simple and promising method that maintains efficient optical coupling to the SNSPD while providing a sub wavelength sized focal spot [32, 33]. Confocal microscopy is based on a simple two lens system that uses a pinhole to remove all out of focus and off-axis light whilst maintaining efficient coupling. An example of a confocal microscopy configuration designed for low temperature nano-optical testing is shown in Figure 1.2. The focal spot size achieved can be approximated using the Sparrow criterion. Using an objective lens with a high numerical aperture (*NA*) provides an increased optical resolution by decreasing the focal spot size.

In this thesis I have applied these nano-optical methods to gain new insights into the underlying device physics of the SNSPD. The structure of this thesis is as follows: Chapter 2 provides a detailed discussion of single-photon detector technologies, including those based upon semiconductor and superconducting materials. Optical coupling methods, including fibre-coupling and microscopy based illumination techniques are also discussed in detail.

The focus of this thesis is on the design and construction of a miniature confocal microscope configuration [34] operating at telecommunications wavelengths and integrated inside a closed cycle refrigerator (see Figure 1.2). In Chapter 3 the experimental techniques used are described in detail. These techniques include the fabrication process [35] required to produce SNSPDs (devices tested were fabricated by our collaborators S. Miki and Z. Wang from NICT, Japan) and the packaging of the SNSPDs in-house at Heriot-Watt University. Two confocal microscope configurations are detailed. The first version is designed for visible and NIR wavelengths [33] and used liquid helium as the cooling method. The second version is the miniature confocal microscope integrated inside a closed cycle refrigerator and is designed for telecommunication wavelengths [34]. The design and construction of the miniature confocal microscope configuration is detailed with careful consideration of the optics. For both systems a set of X, Y and Z piezoelectric linear positioners and an X-Y piezoelectric scanner are used for either sample (visible - NIR system) or focal spot (miniature system) movement; the operating principle of these are detailed. The optical resolution achieved by both systems is discussed. The electrical and optical measurements used to characterise SNSPDs are also explained.

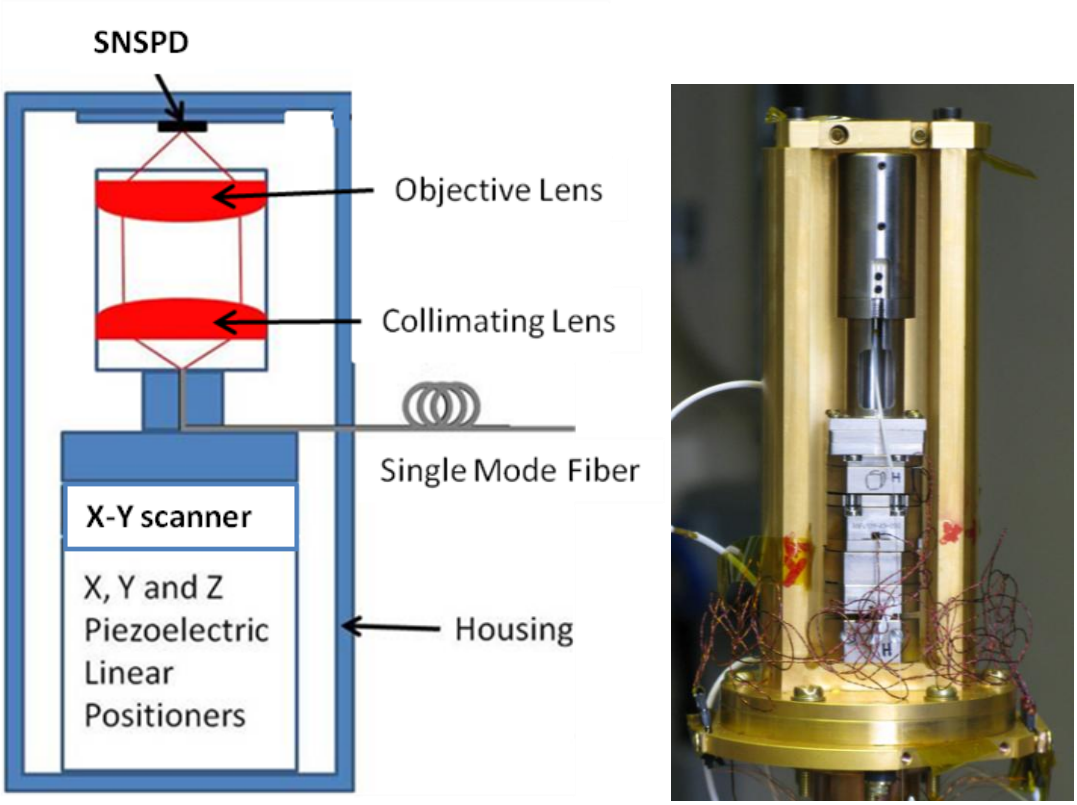

Figure 1.2 – A miniature confocal microscope configuration for low temperature nano-optical testing. Left - Schematic, right – photograph while mounted to a Gifford-McMahon coldhead.

Chapter 4 describes the measurements performed in the visible – NIR confocal microscope configuration operated using liquid helium (LiHe). These measurements compare a 50 % (100 nm wide wires and 200 nm pitch) and a 10 % (100 nm wide wires and 1 μm pitch) fill factor SNSPD. The uniformity of the SNSPDs affects the *DE* across the SNSPDs, which is shown by the 10 % fill factor SNSPD being more uniform and having an increased maximum *DE*. The polarisation dependence of the *DE* of both the 50 % and 10 % fill factor SNSPDs is measured and compared to simulations performed by Vikas Anant at MIT (see Appendix I). These measurements were performed at λ = 950 nm.

Chapter 5 describes measurements at λ = 1550 nm using the miniature confocal microscope integrated into a closed cycle refrigerator. The properties of two constricted SNSPDs are mapped to show the variation in *DE* along with the temporal response (timing jitter and output pulse timing delay) variation of the SNSPD. To understand the variation in temporal response across each of the SNSPDs, the leading edge of the output pulse shapes were fitted to a simple but highly effective phenomenological

PSPICE circuit model [34, 36]. The PSPICE model shows that variations in the resistance of the hotspot formed by the absorption of photons cause variations in temporal response from different locations across the SNSPD. This provides an understanding of the underlying physics of SNSPDs and indicates why constricted SNSPDs have increased timing jitter. This study also points the way for newer SNSPD designs that could exploit this effect. One prospect is that spatial information could be extracted with adequate timing resolution so that this device could be used in practical applications such as imaging.

Chapter 6 provides a conclusion and outlook to my thesis work. Significant improvements have been made since I started this work in October 2007. I summarise my contribution to the research field and provide an outlook on the future directions that research in the field may take.

1.2 Chapter 1 References

1. R. H. Hadfield, *Single-photon detectors for optical quantum information applications.* Nature Photonics, 2009. **3**(12): p. 696-705.
2. J. Chen, J.B. Altepeter, M. Medic, K.F. Lee, B. Gokden, R.H. Hadfield, S.W. Nam, and P. Kumar, *Demonstration of a quantum controlled-NOT gate in the telecommunications band.* Physical Review Letters, 2008. **100**(13): p. 133603.
3. C. M. Natarajan, A. Peruzzo, S. Miki, M. Sasaki, Z. Wang, B. Baek, S. Nam, R.H. Hadfield, and J.L. O'Brien, *Operating quantum waveguide circuits with superconducting single-photon detectors.* Applied Physics Letters, 2010. **96**(21): p. 211101.
4. R. H. Hadfield, J.L. Habif, J. Schlafer, R.E. Schwall, and S.W. Nam, *Quantum key distribution at 1550 nm with twin superconducting single-photon detectors.* Applied Physics Letters, 2006. **89**: p. 241129.
5. H. Takesue, S.W. Nam, Q. Zhang, R.H. Hadfield, T. Honjo, K. Tamaki, and Y. Yamamoto, *Quantum key distribution over a 40-dB channel loss using superconducting single-photon detectors.* Nature Photonics, 2007. **1**(6): p. 343-348.
6. A. McCarthy, R.J. Collins, N.J. Krichel, V. Fernandez, A.M. Wallace, and G.S. Buller, *Long-range time-of-flight scanning sensor based on high-speed time-correlated single-photon counting.* Applied Optics, 2009. **48**(32): p. 6241-6251.
7. N. J. Krichel, A. McCarthy, and G.S. Buller, *Resolving range ambiguity in a photon counting depth imager operating at kilometer distances.* Optics Express, 2010. **18**(9): p. 9192-9206.
8. R. E. Warburton, A. McCarthy, A.M. Wallace, S. Hernandez-Marin, R.H. Hadfield, S.W. Nam, and G.S. Buller, *Subcentimeter depth resolution using a single-photon counting time-of-flight laser ranging system at 1550 nm wavelength.* Optics Letters, 2007. **32**(15): p. 2266-2268.
9. R. H. Hadfield, M.J. Stevens, S.S. Gruber, A.J. Miller, R.E. Schwall, R.P. Mirin, and S.W. Nam, *Single photon source characterization with a superconducting single photon detector.* Optics Express, 2005. **13**(26): p. 10846-10853.
10. R. H. Hadfield, M.J. Stevens, R.P. Mirin, and S.W. Nam, *Single-photon source characterization with twin infrared-sensitive superconducting single-photon detectors.* Journal of Applied Physics, 2007. **101**(10): p. 103104.

11. C. Zinoni, B. Alloing, C. Monat, V. Zwiller, L.H. Li, A. Fiore, L. Lunghi, A. Gerardino, H. de Riedmatten, H. Zbinden, and N. Gisin, *Time-resolved and antibunching experiments on single quantum dots at 1300 nm.* Applied Physics Letters, 2006. **88**(13): p. 131102.
12. E. A. Dauler, B.S. Robinson, A.J. Kerman, V. Anant, R.J. Barron, K.K. Berggren, D.O. Caplan, J.J. Carney, S.A. Hamilton, K.M. Rosfjord, M.L. Stevens, and J.K.W. Yang, *1.25-Gbit/s photon-counting optical communications using a two-element superconducting nanowire single photon detector.* Advanced Photon Counting Techniques, 2006. **6372**: p. U290-U297.
13. B. S. Robinson, A.J. Kerman, E.A. Dauler, R.O. Barron, D.O. Caplan, M.L. Stevens, J.J. Carney, S.A. Hamilton, J.K.W. Yang, and K.K. Berggren, *781 Mbit/s photon-counting optical communications using a superconducting nanowire detector.* Optics Letters, 2006. **31**(4): p. 444-446.
14. B. S. Robinson, A.J. Kerman, E.A. Dauler, D.M. Boroson, S.A. Hamilton, J.K.W. Yang, V. Anant, and K.K. Berggren, *Demonstration of Gigabit-per-second and higher data rates at extremely high efficiency using superconducting nanowire single photon detectors - art. no. 67090Z.* Free-Space Laser Communications Vii, 2007. **6709**: p. Z7090-Z7090.
15. T. Yamashita, S. Miki, K. Makise, W. Qiu, H. Terai, D. Fujiwara, J.M. Sasaki, and Z. Wang, *Origin of intrinsic dark count in superconducting nanowire single-photon detectors.* arXiv:1103.2844v1 [cond-mat.supr-con], 2011.
16. T. Yamashita, S. Miki, W. Qiu, M. Fujiwara, M. Sasaki, and Z. Wang, *Temperature dependent performances of superconducting nanowire single-photon detectors in an ultralow-temperature region.* Applied Physics Express, 2010. **3**(10): p. 102502.
17. W. Becker, *Advanced Time-Correlated Single Photon Counting Techniques*. 2005, Springer.
18. S. K. Poultney, *Single photon detection and timing: experiments and techniques*, Advances in Electronics and Electron Physics, L. Marton and M. Claire, Editors. 1972, Academic Press. p. 39-117.
19. S. Cova, A. Longoni, and A. Andreoni, *Towards picosecond resolution with single-photon avalanche diodes.* Review of Scientific Instruments, 1981. **52**(3): p. 408-412.

20. S. Cova, A. Lacaita, M. Ghioni, G. Ripamonti, and T.A. Louis, *20-ps timing resolution with single-photon avalanche diodes.* Review of Scientific Instruments, 1989. **60**(6): p. 1104-1110.
21. *Perkin Elmer SPAD* *http://optoelectronics.perkinelmer.com/content/RelatedLinks/SpecificationSheets/SPC_PhotoDetectors.pdf (Date Accessed 15th March 2011).*
22. K. J. Gordon, V. Fernandez, P.D. Townsend, and G.S. Buller, *A short wavelength GigaHertz clocked fiber-optic quantum key distribution system.* IEEE Journal of Quantum Electronics, 2004. **40**(7): p. 900-908.
23. H. Takesue, T. Honjo, K. Tamaki, Y. Tokura, and Itu, *Differential phase shift quantum key distribution*. Proceedings of the First Itu-T Kaleidoscope Academic Conference Innovations in Ngn: Future Network and Services. 2008. 229-235.
24. *SMF-28e optical fiber, www.corning.com*.
25. R. E. Warburton, M. Itzler, and G.S. Buller, *Free-running, room temperature operation of an InGaAs/InP single-photon avalanche diode.* Applied Physics Letters, 2009. **94**(7): p. 071116.
26. S. Pellegrini, R.E. Warburton, L.J.J. Tan, J.S. Ng, A.B. Krysa, K. Groom, J.P.R. David, S. Cova, M.J. Robertson, and G.S. Buller, *Design and performance of an InGaAs-InP single-photon avalanche diode detector.* IEEE Journal of Quantum Electronics, 2006. **42**(3-4): p. 397-403.
27. G. N. Gol'tsman, O. Okunev, G. Chulkova, A. Lipatov, A. Semenov, K. Smirnov, B. Voronov, A. Dzardanov, C. Williams, and R. Sobolewski, *Picosecond superconducting single-photon optical detector.* Applied Physics Letters, 2001. **79**(6): p. 705-707.
28. R. Radebaugh, *Refrigeration for superconductors.* Proceedings of the IEEE, 2004. **92**(10): p. 1719-1734.
29. K. M. Rosfjord, J.K.W. Yang, E.A. Dauler, A.J. Kerman, V. Anant, B.M. Voronov, G.N. Gol'tsman, and K.K. Berggren, *Nanowire Single-photon detector with an integrated optical cavity and anti- reflection coating.* Optics Express, 2006. **14**(2): p. 527-534.
30. E. A. Dauler, B.S. Robinson, A.J. Kerman, J.K.W. Yang, K.M. Rosfjord, V. Anant, B. Voronov, G. Gol'tsman, and K.K. Berggren, *Multi-element superconducting nanowire single-photon detector.* IEEE Transactions on Applied Superconductivity, 2007. **17**(2): p. 279-284.

31. J. Zhang, W. Slysz, A. Verevkin, O. Okunev, G. Chulkova, A. Korneev, A. Lipatov, G.N. Gol'tsman, and R. Sobolewski, *Response time characterization of NbN superconducting single-photon detectors.* IEEE Transactions on Applied Superconductivity, 2003. **13**(2): p. 180-183.
32. R. H. Hadfield, P.A. Dalgarno, J.A. O'Connor, E. Ramsay, R.J. Warburton, E.J. Gansen, B. Baek, M.J. Stevens, R.P. Mirin, and S.W. Nam, *Submicrometer photoresponse mapping of nanowire superconducting single-photon detectors.* Applied Physics Letters, 2007. **91**(24): p. 241108.
33. J. A. O'Connor, P.A. Dalgarno, M.G. Tanner, R.J. Warburton, R.H. Hadfield, B. Baek, S.W. Nam, S. Miki, Z. Wang, and M. Sasaki, *Nano-optical studies of superconducting nanowire single photon detectors*. Quantum Communication and Quantum Networking, O. Akan, et al., Editors. 2009, Springer Berlin Heidelberg. p. 158-166.
34. J. A. O'Connor, M.G. Tanner, C.M. Natarajan, G.S. Buller, R.J. Warburton, S. Miki, Z. Wang, S.W. Nam, and R.H. Hadfield, *Spatial dependence of output pulse delay in a niobium nitride nanowire superconducting single-photon detector.* Applied Physics Letters, 2011. **98**(20): p. 201116-3.
35. S. Miki, M. Fujiwara, M. Sasaki, and Z. Wang, *NbN superconducting single-photon detectors prepared on single-crystal MgO substrates.* IEEE Transactions on Applied Superconductivity, 2007. **17**(2): p. 285-288.
36. A. J. Kerman, E.A. Dauler, W.E. Keicher, J.K.W. Yang, K.K. Berggren, G. Gol'tsman, and B. Voronov, *Kinetic-inductance-limited reset time of superconducting nanowire photon counters.* Applied Physics Letters, 2006. **88**(11): p. 111116.

Chapter 2 Background

2.1 Introduction to Photon Counting

2.1.1 Properties of Single-Photon Detectors

Photon counting is a technique used in many applications encompassing quantum information processing [1, 2], quantum key distribution (QKD) [3-5], time-of-flight ranging [5-7], quantum emitter characterization [8, 9] and high speed communication [10-12]. Quite simply, photon counting is counting the number of incident photons on a detector. It is preferable to operate in the single-photon regime which will remove or reduce the possibility of the measured detection event being caused by a multi-photon pulse. A well established and powerful technique commonly used in photon counting is time correlated single-photon counting (TCSPC). TCSPC is the detection of single photons and the measurement of their arrival time with respect to a reference signal. Each application puts different demands on single-photon detector performance. The main properties of single-photon detectors are:

- the spectral range of operation
- the detection efficiency (*DE*)
- the dark count rate (DCR)
- detector "dead time"
- the timing jitter (Δt)

The spectral sensitivity of a single-photon detector (see Figure 2.1) is governed by the choice of material and operating principle of the single-photon detector. In semiconductor or electron multiplier based detectors the energy of the incident light must be equal to or greater than the bandgap of the semiconductor material. In detectors based on superconducting materials the energy of the photon has to be large enough to break the Cooper pairs, by being larger than the superconducting energy gap. At visible wavelengths semiconductor based single-photon detectors are a mature technology with

good operating characteristics, but the performance declines as the wavelength increases towards telecommunication wavelengths. In the telecommunications wavelength range there is considerable demands for improved photon counting technologies.

Figure 2.1 – The spectral sensitivity of a single-photon detector. The "blue" short wavelength, high energy photon produces an output pulse signalling the detection of a photon. The "red" longer wavelength, lower energy photon does not produce an output pulse as the energy of the "red" photon is too small to trigger the detector.

The detection efficiency (*DE*) of a single-photon detector is the proportion of the incident photons that are detected (see equation (2.1)). The best possible case is to achieve a *DE* of unity (100 %), meaning all incident photons are detected. Not all of the incident photons on a single-photon detector are necessarily detected (see Figure 2.2) which means the *DE* is typically less that 100 %. The percentage *DE* is given by

$$DE(\%) = \frac{No\ of\ \ Detected\ \ Photons}{No\ of\ \ Incident\ \ Photons} \times 100\ . \qquad \textbf{(2.1)}$$

Figure 2.2 – The detection efficiency (*DE*) of a single-photon detector. Two of the incident photons (red arrows) produce voltage pulses signalling the detection of a photon. The other (middle) photon does not produce a voltage pulse indicating that the *DE* is less than 100 %.

A dark count is when the single-photon detector gives an output pulse when no photon is incident (see Figure 2.3). These false detection events can have a number of causes: the detector material properties, detector biasing or external noise affecting the system can all contribute to the dark count rate. The specific photon counting application determines what dark count rate can be tolerated.

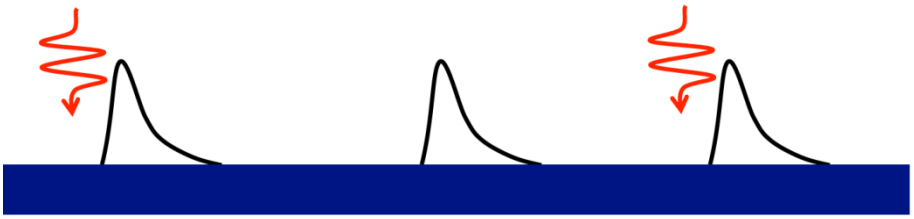

Figure 2.3 – The dark count rate of a single-photon detector. Two of the voltage pulses are triggered by the detection of photons (red arrows). The other voltage pulse (middle) is a dark count as it is not caused by an incident photon. Dark counts are false counts occurring without the detection of an incident photon.

Detector "dead time" (see Figure 2.4) is the time taken after a detection event for the single-photon detector to recover or reset. Ideally this interval should be negligible or very small. The type of detector chosen governs the detector dead time. After the dead time the single-photon detector should be able to detect a further photon without reduced detection efficiency. In practice the counting electronics may also have a significant dead time.

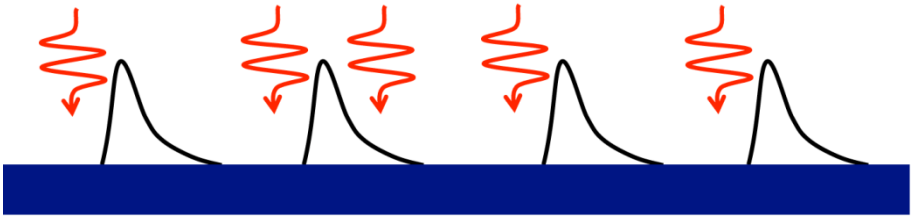

Figure 2.4 – The dead time of a single-photon detector. Four of the incident photons (red arrows) produce voltage pulses which signal the detection of each photon. One photon (middle) is incident while a voltage pulse is still present meaning that it can not be detected. This is because the single-photon detector is in a state where an incident photon will not produce a voltage pulse. The time which the single-photon detector is in the state that an incident photon will not produce a voltage pulse is the detector dead time. The dead time can vary significantly between different single-photon detector types.

The timing jitter of detectors is a limiting factor in many experiments. The timing jitter is the variation or uncertainty in the time between an incident photon being absorbed and an output electrical pulse being generated.

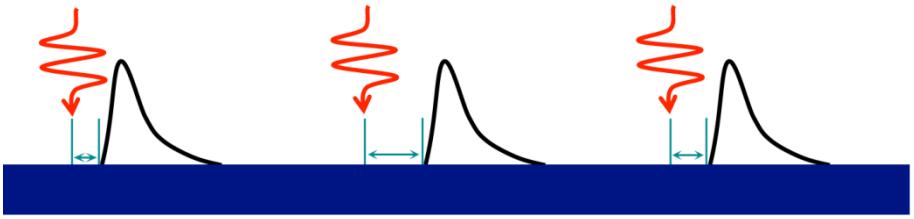

Figure 2.5 – The of timing jitter of a single-photon detector. Each of the incident photons (red arrows) produces a voltage pulse which signals the detection of the photon. Each voltage pulse produced does not start at exactly the same time after the absorption of an incident photon. This timing difference or uncertainty between the time the photon is incident on the detector and the voltage pulse starting is the timing jitter. The timing jitter is governed by the type of the single-photon detector.

The type of detector and material choice (semiconductor, electron multiplier or superconductor) significantly affects each of these properties.

2.1.2 Photon Counting Applications

It is important to consider the requirements on detector performance in different photon counting applications with reference to the properties discussed in section 2.1.1.

Quantum key distribution (QKD) is a method for secure communications using the principles of quantum mechanics to guarantee the security [13-15]. For QKD the detector requirements are high detection efficiency at the operating wavelength, a low dark-count rate, a short detector dead time to allow for faster clock rates and a small timing jitter for increased timing resolution. To date the best results achieved are a secure key transmitted over a 250 km fibre link, with 625 MHz clock rate and quantum bit error rate (QBER) of 1.9 % [16] using the coherent one-way (COW) protocol [17-19], rather than the BB84 protocol presented by Bennett and Brassard [20].

Optical time-of-flight ranging is an accurate depth ranging and three dimensional imaging technique which is useful in several fields, including manufacturing [21], defence [22] and geosciences [23]. Using time-correlated single-photon counting techniques (TCSPC) [24] this method has been shown to work at both short [25] (lab based) and longer [26] (km) distances. Good temporal, range and depth resolution with three dimensional imaging is achieved using a detector with a small timing jitter. This

depth resolution gives the potential to identify multiple targets without prior knowledge of the target profile. Depth resolution of 15 mm has been reported at a target distance of 4.4 km [7].

Transitions between energy levels in an atom, molecule or solid state defect can give rise to the emission of a single-photon. A single-photon emitter, with controlled wavelength, low timing jitter and narrow spectral linewidth would be highly desirable for applications such as QKD. There is significant interest and research into developing a single-photon source using a variety of differing methods including atoms in high Q-cavities [27], single molecules [28], and defects in diamond [29]. A promising approach is the use of quantum dots [30-32], which have been shown to produce single-photons on demand [33, 34] at wavelengths where silicon detectors are efficient (below 1 μm wavelength). For telecommunications wavelengths (1310 nm and 1550 nm) single-photon emitters based on individual quantum dots are not as well developed [35], both due to the difficulties in making low density quantum dots beyond 1310 nm and the limitations of detector technology at these wavelengths. The main characterisation measurements [8, 9] of quantum emitters are coincidence measurements to determine the second order correlation function ($g^{(2)}(0)$) [35, 36] which gives the probability of multiple photons per pulse being emitted. Time-resolved photoluminescence (TRPL) [37, 38] measurements provide measurements of the emission lifetime of the quantum dot. The detector requirements for these measurements are high detection efficiency at the desired wavelength, low dark counts and small timing jitter to provide high resolution.

High speed optical communication using photon counting is under consideration for demanding applications such as ground to space communications [39, 40]. The reasons for this include the improvement in the sensitivity of SNSPD detectors at λ = 1550 nm (where solar background is low) and the capacity to combine signals from numerous spatial modes. Many of the limiting factors in high speed optical communication systems are due to the non-ideal properties of single-photon detectors, including low detection efficiency, poor timing jitter and long reset times. The improvements in detection efficiency from 10 % with a dark count rate of 91 Hz [41] to 57 % at 1 kHz [42] dark count rate both at λ = 1550 nm has allowed more of the input photons to be

detected. Impressive demonstrations have been carried out at λ = 1550 nm using high efficiency SNSPDs. For example data transfer rates have improved from below 500 kbit/s [43, 44] to 781 Mbit/s [10] using optical communication systems. Dauler *et al* [45] have reported very low timing jitter (29 ps) for an SNSPD. This low timing jitter coupled with fast reset times (~3 ns) have helped to improve data transfer rates using SNSPDs from 781 Mbit/s [46] to 1.25 Gbit/s [11].

2.2 Established and Emerging Single-Photon Detector Technologies

Single-photon detectors can be categorized by the medium used for amplification of the detection event. An electron multiplier, a semiconductor and a superconductor are examples of this. A brief discussion of the advantages and disadvantages of each type of detector is given in this section. The potential for improvement will be discussed, with particular focus on SNSPD technology.

2.2.1 Electron Multiplier-based Single-Photon Detectors

Electron multiplier-based detectors such, as photomultiplier tubes (PMTs) [47, 48] and micro-channel plate (MCP) detectors [49], are one of the oldest and most established single-photon detector technologies. They have been implemented in a wide range of photon counting applications.

The simplest PMT contains a photocathode for absorption of photons inside a vacuum tube (see Figure 2.6). The bandgap of the semiconductor material of the photocathode controls the energy of photons that can be detected. The energy of the incoming photon has to be greater than or equal to the bandgap energy). Electrons are released from the photocathode by the photoelectric effect; the small number of released electrons is then multiplied by using a cascade of secondary electron released from a series of electrodes (dynodes), with each one biased with a greater voltage (in the kV range). This gives a macroscopic current that can be detected.

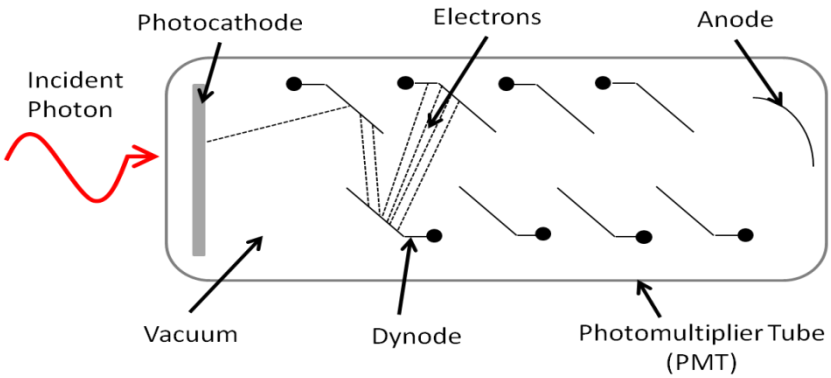

Figure 2.6 – A schematic of a photomultiplier tube (PMT) illustrating the principle of operation.

PMTs with large active areas (up to 10 mm diameter) are available. At visible and NIR wavelengths, dark count rates below 100 Hz and timing jitter of several hundred picoseconds can routinely be achieved. Low multiplication noise permits operation in a linear mode meaning that the number of simultaneously incident photons can be distinguished. The limiting factors of PMTs and MCPs are relatively low detection efficiencies, typically in the range 10-30 %. Up to 40 % detection efficiency has been shown at λ = 500 nm [50]. Insensitivity to infrared light limits the applications that PMTs can be used in. Infrared sensitive photocathodes [51] and hybrid PMTs [52] have been developed to address this problem. The trade-off for this extended spectral range is low detection efficiency, high dark count rates and increased cooling requirements. To date at λ = 1550 nm, an InGaAs PMT has been reported with an efficiency of 2 % with 200 kHz dark count rate with operation at 200 K [53].

2.2.2 Semiconductor based Single-Photon Detectors

Semiconductor based single-photon detectors, especially single-photon avalanche diodes (SPADs) [54] have received a great deal of attention and development in recent years [55-58]. SPADs are based on either a p-n or a p-i-n junction (avalanche photodiode) structure under reverse bias (Figure 2.7). In a sufficiently high electric field a drifting electron in this structure can gain sufficient kinetic energy to create an electron-hole pair due to collisions with the atomic lattice. This process of impact ionisation [59] triggers avalanche multiplication as further collisions create a cascade of

electron-hole pairs. In a SPAD the initial electron-hole pair is generated by the absorption of a photon with energy greater than the semiconductor bandgap.

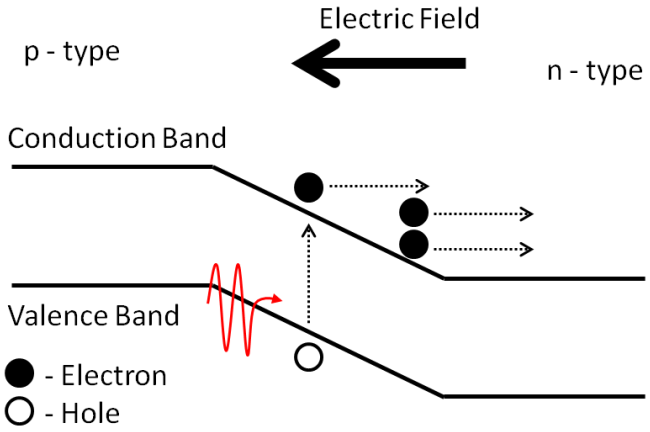

Figure 2.7 – A diagram of impact ionization in a reverse biased p-n junction. This process is fundamental to the operation of semiconductor single-photon avalanche photodiodes (SPADs) [59].

For single-photon detection the p-n or p-i-n junction is reverse-biased above the avalanche breakdown voltage. This is known as Geiger mode. In Geiger mode a single electron-hole pair can be sufficient to trigger the avalanche of electron-hole pairs created by impact ionisation. This avalanche current is self sustaining.

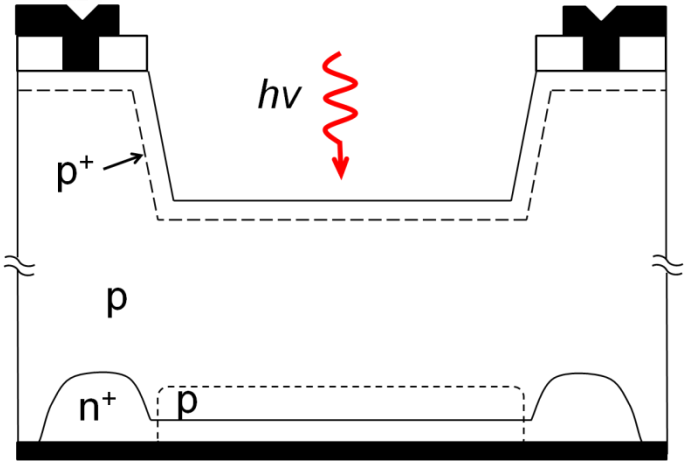

Figure 2.8 – A diagram of the basic structure of a single-photon avalanche diode (SPAD) detector [59].

Figure 2.8 shows an example of a SPAD device architecture. The absorbed incident photon creates the electron-hole pair required for the avalanche process. Impact ionisation and avalanche multiplication generates a measureable output current pulse. To allow the SPAD to detect a subsequent photon, it must be quenched to permit the

detector to return to its quiescent state. A SPAD is quenched when the reverse bias voltage is reduced to below breakdown voltage. Quenching can be implemented either passively [60, 61] or actively [62].

SPADs have smaller active areas compared to PMTs with diameters typically of the order of tens to hundreds of microns. Depending upon the design and readout, timing jitter ranges from tens [55] to hundreds [58] of picoseconds. Silicon based SPADs can have *DE* greater than 50 %, low dark count rates (few tens of Hz) and count rates of a few MHz. The *DE* of Si SPADs falls rapidly at wavelengths above 900 nm and is almost negligible beyond λ = 1000 nm. For telecommunications wavelength performance the absorbing layer must be a narrow-gap semiconductor such as Ge or InGaAs. Performance at telecommunications wavelengths is often significantly reduced due to high DCR. *DE* of less than 50 % and kHz dark count rates are common. Timing jitter is increased to hundreds of picoseconds. High dark counts and afterpulsing mean that InGaAs and similar SPADs are normally operated in a gated mode. This is where the detector is only active for a short pre-determined time. Performance at 1550 nm of 10 % efficiency at 91 Hz dark count rate and 370 ps jitter [41] has been reported.

2.2.3 Superconductor based Single-Photon Detectors

Superconductor based single-photon detectors including transition edge sensors (TES), superconducting tunnel junctions (STJs) and kinetic inductance detectors (KIDs) are an attractive alternative in fields such as astronomy because of their low noise and high sensitivity over a large spectral range (gamma rays to infrared wavelengths). Greater than 90 % efficiency at a wavelength of 1550 nm has been reported in TES detectors with no known intrinsic noise source [63, 64]. The disadvantages of these detectors are typically large timing jitter of the order 100 ns and maximum count rates in the order of hundreds of kHz. Furthermore operation at mK temperatures is required. The first superconducting detector to provide low timing jitter and high counting rates is the superconducting nanowire single-photon detector (SNSPD). *DE* of up to 57 % at 1550 nm wavelength, Δt of 30 ps and maximum count rate of 1 GHz have been reported [42]. SNSPDs can be operated at 4 K and can now be used in conjunction with

closed-cycle refrigerators (section 3.5). These developments mean that SNSPDs are highly attractive for use in a wide range of infrared photon counting applications.

2.3 Superconductivity

Superconductivity was discovered by Heike Kamerlingh Onnes in 1911 [65] while studying mercury at cryogenic temperatures. It was observed that the resistance of mercury suddenly vanished at 4.2 K [66, 67]; this observation marked the start of the field of superconductivity. Superconductivity is a quantum mechanical effect in which a material has no electrical resistance. There is a sharp phase transition between the resistive and superconducting states occurring at a critical temperature T_c (also known as the transition temperature).

In a standard conductor (such as a normal metal), the current flowing can be viewed as a stream of electrons moving across a lattice of positively charged ions. The electron flow is disrupted by scattering (from impurities or phonons) causing some of the energy in the electron flow to be absorbed and converted to vibrational kinetic energy of the lattice (heat). This mechanism for loss of energy is known as electrical resistance. In a superconductor the current flow is not a stream of individual electrons, but a stream of bound electron pairs known as Cooper pairs [68] (named after Leon Cooper). The electron pairing in Cooper pairs is due to the attractive force between electrons that is caused by electron-phonon interactions. The formation of Cooper pairs (see Figure 2.9) becomes ever more favourable below the transition temperature.

The BCS theory of superconductivity was developed by Bardeen, Cooper and Schrieffer in 1957 [69] and predicted the presence of Cooper pairs. This theory also predicts that all Cooper pairs in a material are correlated. To break one Cooper pair, the energy of all other pairs must be changed. The binding energy of a Cooper pair corresponds to an energy gap ($2|\Delta|$) on the order of meV. In the BCS theory Δ is defined as [70]:

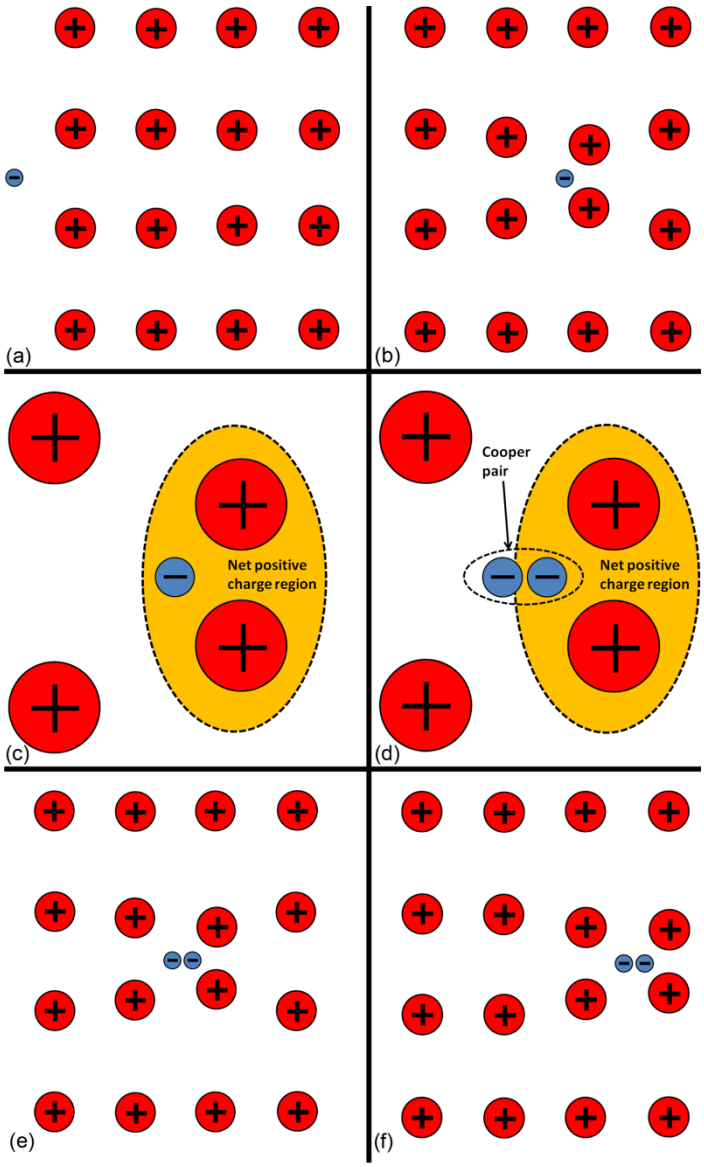

Figure 2.9 – The formation of Cooper pairs in a superconductor. (a) An electron moves through a lattice of positively charged ions. (b) The electron distorts the lattice due to an attraction between the negatively charged electron and the positive ions. (c) The lattice distortion produces a net positive region which contains multiple positive ions and the electron. (d) The net positive region attracts another electron. The attraction between the net positive region and the second electron draws the electrons close together overcoming their mutual repulsion. This arrangement is a low energy configuration and is stable. This pair of electrons is called a Cooper pair. (e) and (f) The Cooper pair moves through the lattice as a supercurrent.

$$|\Delta| = 1.76 k_B T_C = 2\hbar\omega_D . e^{\frac{-1}{N_{(0)}V}} \qquad \textbf{(2.2)}$$

where k_B is the Boltzman constant, T_C is the transition temperature of the superconducting material, h is Planck's constant, ω_D is the lattice vibration frequency (also known as the Debye frequency), $N_{(0)}$ is the number of normalised energy states

and V is the strength of the attractive force between electrons in the Cooper pairs. Equation 2.2 is only valid for $N_{(0)}V << 1$, the weak coupling approximation.

The coherence length (ξ) in a superconductor is a measure of the extent of a Cooper pair in that material. ξ puts a limit on the length scale for superconductivity. For a material sample to superconduct in a specific dimension the length in that direction must be larger than ξ. This also means that at the edge of the superconductor with a dimension longer than ξ, the material does not superconduct until a distance of ξ has been surpassed. The coherence length is defined as [70]**:**

$$\xi = \frac{\hbar v_f}{\pi \Delta} \qquad \textbf{(2.3)}$$

where v_f is the Fermi velocity and Δ is the energy gap.

Table 2.1 lists common superconducting materials along with their superconducting properties (energy gap, transition temperature and coherence length).

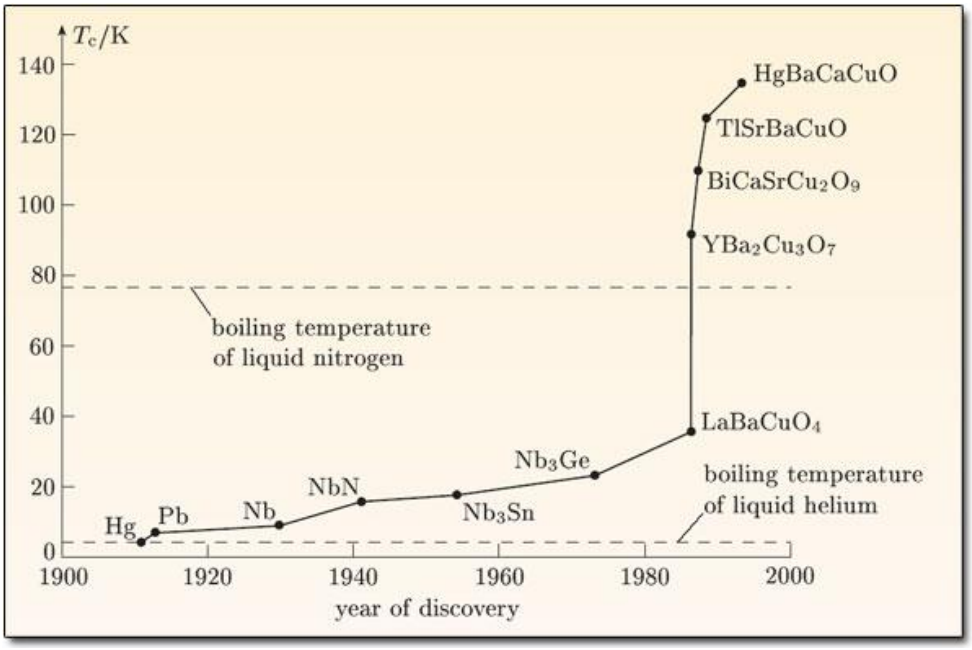

Figure 2.10 – Development of superconducting materials between the years 1900 and 2000 [71].

BCS theory only describes conventional superconductors (metals and alloys). Superconducting materials for which BCS theory does not provide a sufficient explanation are termed "unconventional" superconductors. This includes the class of so-called "high temperature" superconductors. These materials have high transition temperatures that can be achieved using liquid nitrogen (77 K). The mechanisms for these types of superconductors are the subject of considerable debate and have not yet been satisfactorily described.

Material	Symbol	Energy Gap Δ (meV)	Transition Temperature T_C (K)	Coherence Length ξ (nm)
Niobium	Nb	2.32	9.25	40
Niobium nitride	NbN	4.5	17	5
Magnesium diboride	MgB_2	7.1	39	13
Yttrium barium copper oxide	YBCO	6 – 8	93	1.5

Table 2.1 - Table of Superconducting Materials [70, 72-75]

2.3.1 Superconducting Nanowire Single-Photon Detector (SNSPD)

Superconducting nanowire single-photon detectors (SNSPD) are detectors that utilize superconducting properties, and were first introduced by Gol'tsman in 2001 [76]. The layout of a SNSPD is a 100 nm wide nanowire that is patterned using electron beam lithography and reactive ion etching in an ultrathin (~ 4 nm) layer of niobium nitride (NbN). The NbN film has a superconducting transition temperature of ~ 10 K.

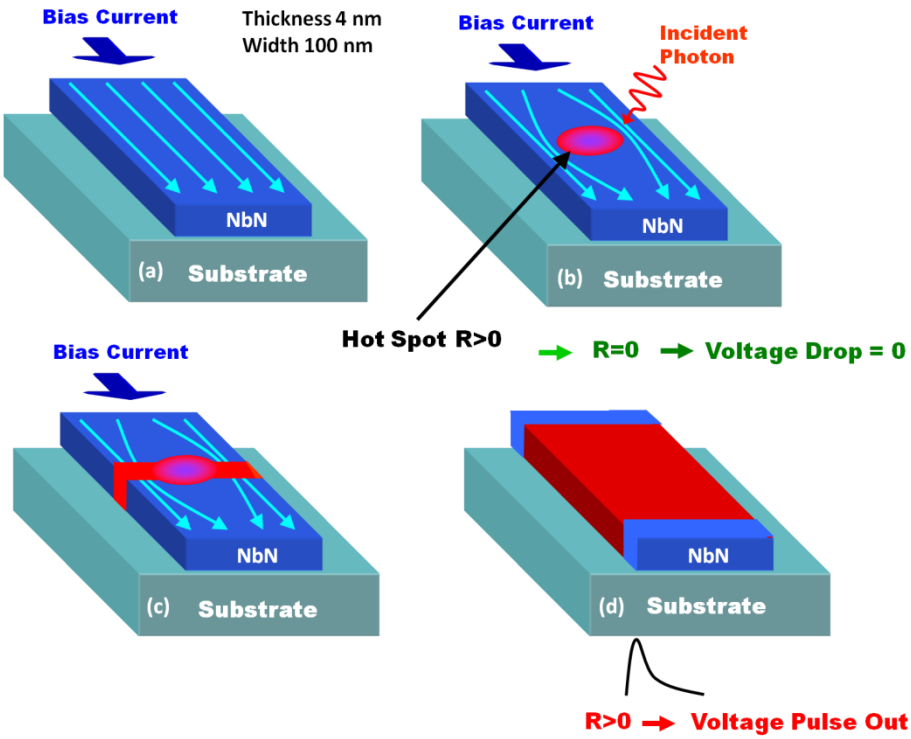

Figure 2.11 – The basic mechanism of hotspot formation in a single wire SNSPD. (a) A nanowire is patterned in an ultrathin (~ 4 nm thick) superconducting film using electron beam lithography and reactive ion etching. The nanowire is current biased to just below its critical current. (b) A photon is incident on the nanowire which is absorbed and breaks the Cooper pairs into electrons producing a resistive "hotspot" (red circular region). The bias current is forced to flow around the hotspot increasing the current density in the regions between the "hotspot" and the edge of the nanowire. (c) The "hotspot" expands to the edge of the nanowire due to the current density at the edges increasing past the critical current density. (d) The hotspot evolves along a length of the nanowire driven by Joule heating creating a resistive region which produces an output voltage pulse, signalling the detection of a photon.

The device is cooled within the range 1.5 – 4 K which is well below its transition temperature. The wire is then current biased to just below its critical current (Figure 2.11 (a)), this is the point when superconductivity breaks down and the device becomes resistive. An incident photon that is absorbed perturbs the current distribution in the wire due to photon-phonon interactions breaking Cooper pairs into electrons (Figure 2.11 (b)). This resistive hotspot (part of the wire will be in the resistive state) perturbs the current density around the hotspot to be greater than the critical current, forcing the wire resistive (Figure 2.11 (c)). The hotspot evolves and grows along the length of wire driven by Joule heating. This change produces a fast voltage output pulse which can be

amplified and recorded (Figure 2.11 (d)). The *DE* and the DCR are dependent on the current biasing. Both the detection efficiency and dark count rate increase with bias current.

Coupling light to a single nanowire is inefficient, which severely limits the detection efficiency. To tackle this optical coupling problem, Verevkin *et al* [77] developed a device consisting of one long nanowire (0.5 mm) folded back over a large area (10 µm x 10 µm) in a meander structure (see Figure 2.12). This increased the optical coupling to the detector as more of the incident light falls over a photosensitive area of the device. To date meander areas of 10 µm x 10 µm [77] and 20 µm x 20 µm [78, 79] have been fabricated, due to their compatibility for fibre coupling to single mode fibre. *DE* at a wavelength of 1550 nm of 3.5 % at 100 Hz dark-count rate has been reported [78].

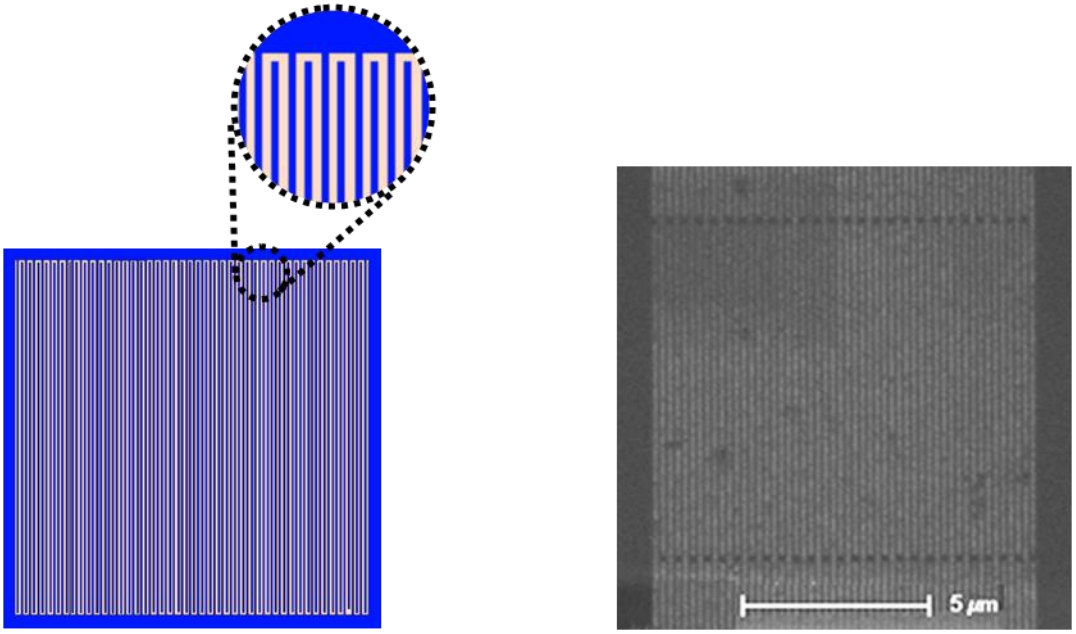

Figure 2.12 – Meander structure, left – schematic of SNSPD, right – Scanning electron micrograph of SNSPD [80].

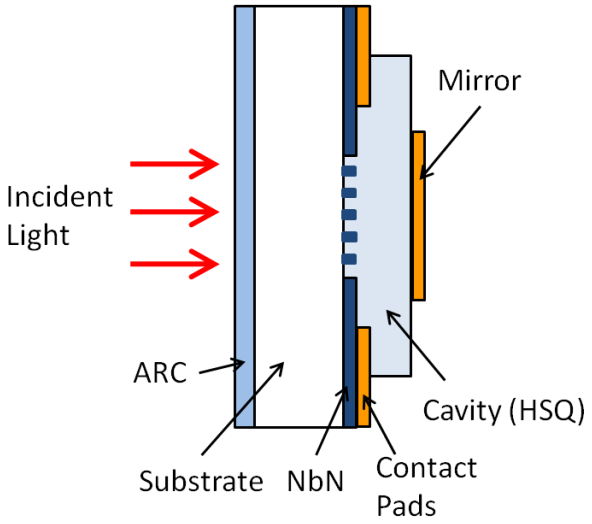

Figure 2.13 – Cavity design for improved optical absorption of incident light in an SNSPD [42]. Incident light is coupled through an anti reflection coating (ARC) and the substrate. The light interacts with the SNSPD layer (NbN) with most of the light being transmitted through the SNSPD layer. This light travels through a cavity (HSQ layer) which is a ¼ wavelength thick and is reflected back by the mirror increasing the probability that light will be absorbed in the SNSPD layer. The cavity is a ¼ wavelength thick so an antinode from the cavity is positioned over the SNSPD layer.

A second issue to consider in SNSPDs is the absorption of optically coupled light to the active area. The problem is that most of the light is either transmitted through or reflected back from the detector. This limits detection efficiency to ~ 20 %. Increasing the number of passes incident light can have on the detector has been shown to be the most promising technique to overcome this problem. The simplest method is to have a mirror to reflect the light back on to the detector. The mirror distance from the nanowire must be a ¼ wavelength (in the medium) for peak absorption; at the desired wavelength. Rosfjord et al [42] have shown detection efficiency of 57 % at 1550 nm wavelength with this method using the design shown in Figure 2.13.

Using a meander layout integrated with an optical cavity, provides efficient optical coupling and increases the likelihood that a photon will be absorbed. Using an oxidised silicon substrate is a simple method to produce a mirror under the superconducting nanowire. *DE* of 7.8 % at λ = 1500 nm, at 1 kHz dark count rate, with 60 ps timing jitter has been reported [81], showing ~ two fold improvement in *DE*.

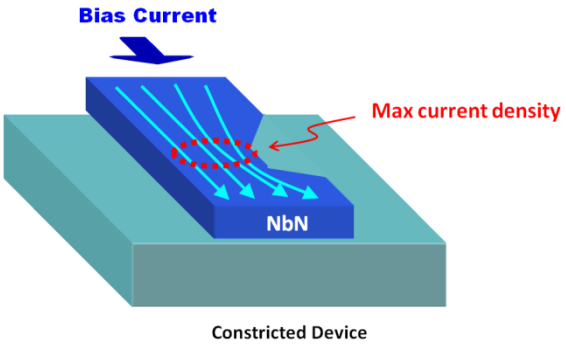

Figure 2.14 – A schematic of a constriction of the nanowire in an SNSPD. The current density at the constriction is higher than the rest of the SNSPD. This increased current density means that the constricted position is the most photosensitive region of the SNSPD.

Now the final limiting factor is the triggering probability in the nanowire; that is to say the probability that an absorbed photon will trigger an output voltage pulse. The uniformity of the nanowire and the photon energy are the main factors which control the triggering probability [81]. The uniformity of the nanowire affects how high the device can be biased, as any constricted regions limit the maximum bias current. A constriction is an effective narrowing of the cross-sectional area of a part of the nanowire (see Figure 2.14). This can be caused by fabrication errors producing either a varying film thickness, or a differing wire width. Variations in film quality and composition can produce the same effect as variations in physical dimensions. The critical current is limited due to the constriction and the maximum current density will occur at this point. The rest of the device that is not constricted has a lower current density compared to the constricted region, and since the triggering probability (and thus sensitivity) increases with bias current, any photons absorbed at non-constricted regions will have a smaller probability of triggering an output voltage pulse. Kinetic inductance and critical current measurements can be used to infer the uniformity of a device (see equation (2.4)), by fitting the data to a theoretical curve (equation (2.5)) of a completely uniform device [82, 83]. Equation (2.5) is derived from the Ginzburg-Landau theory [84] for a thin superconducting strip. The kinetic inductance is given by

$$L \propto 1+\left(\frac{4}{9}\right)\left(\frac{I_C}{I}\right)^2 \qquad \textbf{(2.4)}$$

Introducing a constriction factor C gives

$$\frac{L}{L_{(0)}} = 1 + \left(\frac{4}{9}\right) C^2 \left(\frac{I_C}{I}\right)^2 \quad \textbf{(2.5)}$$

where I_c is the critical current, I is the bias current, L is the inductance and $L_{(0)}$ is the inductance at zero bias current.

Spatial imaging of a significantly constricted device using conventional optical coupling methods, mainly fibre-coupling, is not possible as the incident spot size is larger than the whole device area. Using nano-optical microscopy techniques (specifically a confocal microscopy configuration) the photoresponse map of a constricted device compared to a uniform device has been reported [80]. Optical coupling techniques including fibre-coupling and confocal microscopy are detailed in section 2.4 indicating different routes to achieving improved optical coupling to SNSPDs.

2.4 Optical Coupling for Superconducting Single-Photon Detectors: an Introduction

Effective optical coupling of light to SNSPDs is a vital factor in producing high efficiency detectors. In this section, robust fibre-coupling techniques using standard, tapered and lensed fibres for broad illumination will be explained with their advantages and disadvantages. More advanced optical techniques, namely near-field scanning optical microscopy and confocal microscopy will be described as methods to probe localised areas of SNSPDs with illuminated spot sizes smaller than detector dimensions. Finally solid immersion lens technology is discussed as a modification used to achieve a smaller illuminated spot for more detailed optical probing.

2.4.1 Fibre-Coupling

Optical coupling to SNSPDs is most commonly achieved by the fibre-coupling method (also known as butt-coupling). This is where the polished end of an optical fibre is placed as close to the sensitive area of the detector as possible without coming into

contact with it. The fibre is optically aligned to the active area of the detector and securely clamped in place. Figure 2.15 shows a fibre-coupling scheme which is repeatable and robust enough to survive repeated thermal cycling without losing optical alignment. For telecommunications applications the optical fibre (Corning SMF 28) [85] has a core diameter of 9 microns. Gaussian optics (equations 2.6 and 2.7) provides a limit on the illuminated spot size ($\omega(z)$) on the detector of ~ 10 µm (1/e value). The beam waist $\omega(z)$, as a function of distance (z) from the end of the fibre is given by

$$\omega(z) = \omega(0)\sqrt{1+\left(\frac{z}{z_R}\right)^2} \tag{2.6}$$

where

$$z_R = \frac{\pi\omega_0^2}{\lambda} \tag{2.7}$$

and λ is the free space wavelength.

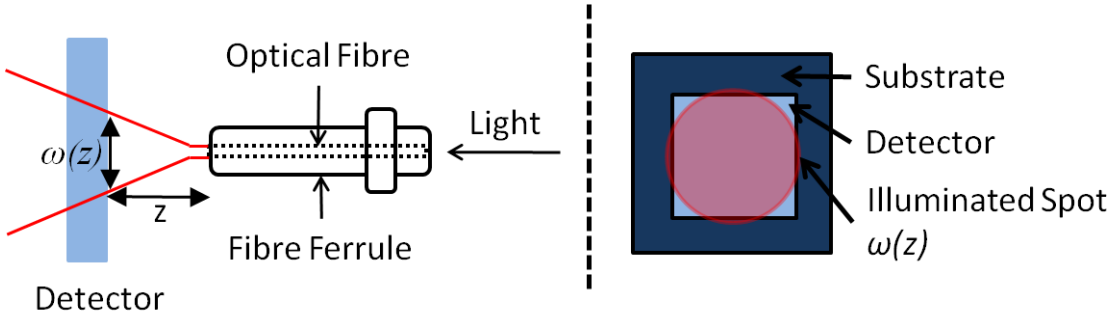

Figure 2.15 – The basic method of fibre-coupling for SNSPDs, left – Divergence of light from the end of an optical fibre onto SNSPD, right - optical alignment of illuminated spot on active area of SNSPD.

These considerations show that the minimum size of detector that will permit efficient fibre-coupling is approximately 10 µm x 10 µm if the spacing z is minimised.

One solution to decreasing the illuminated spot size is to use a tapered fibre (see Figure 2.16). A tapered fibre is an optical fibre with a tapered end which acts like a lens to focus the spot down to a smaller size than that predicted by equation (2.6). Again this limits the minimum size for SNSPDs to 3 µm x 3 µm. For example in reference [86] a 3 µm spot diameter is achieved at λ = 1550 nm at a distance of 14 µm from the fibre tip. Detection efficiency of 24 % at λ = 1550 nm and 1 kHz dark count rate has been reported that using a tapered fibre and a cavity-embedded SNSPD [87].

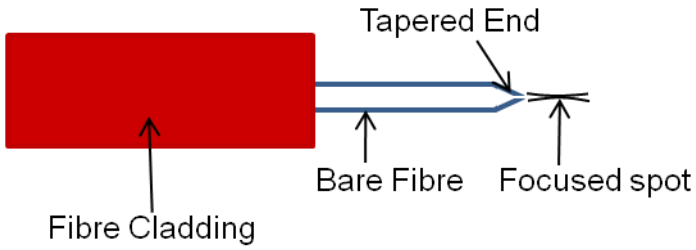

Figure 2.16 – Tapered fibre schematic.

Another possible way to decrease the illuminated spot size from an optical fibre is to use a lensed fibre (see Figure 2.17). A lensed fibre is an optical fibre with a lens spliced onto the end. This focuses the light down to a focal spot. Using a small diameter (125 µm) graded index (GRIN) lens, the illuminated spot size at a distance of 20 µm is 8-10 µm. A detection efficiency of 21 % at λ = 1550 nm has been reported for a cavity integrated SNSPD coupled with a lensed fibre [88].

Fibre coupling using either a standard optical fibre or a lensed fibre is used as an inexpensive, robust and straightforward technique for optically coupling to SNSPDs. One major drawback of fibre coupling is that the optical response of the detector is for the whole active area and localised areas cannot easily be studied for more information about their operation and performance. Another problem with fibre-coupling is that large area (10 µm x 10 µm or greater) devices must be used. These typically have lower uniformity and lower *DE* than smaller area devices.

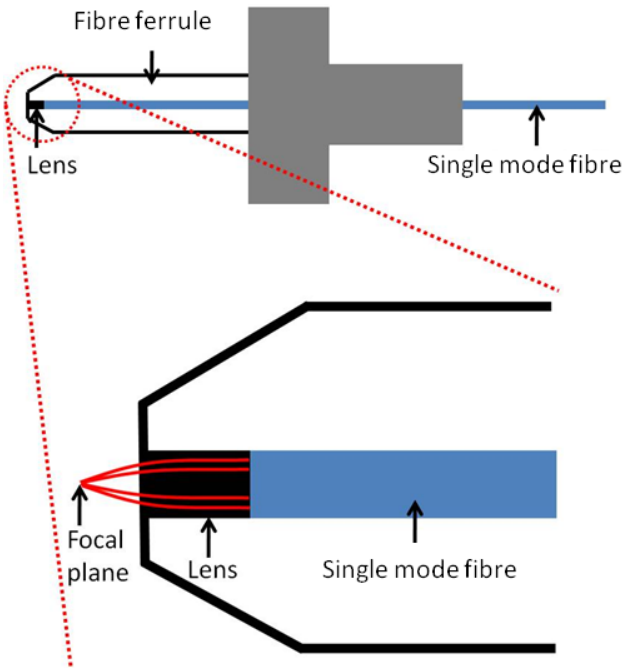

Figure 2.17 – A schematic of a lensed fibre utilizing a GRIN lens. The GRIN (graded index) lens provides focusing of light from the end of an optical fibre which gives increased optical coupling on an SNSPD.

2.4.2 Microscopy Techniques

To study localised areas of SNSPDs, different microscopy techniques are required to decrease the illuminated spot size. Depending upon the illumination, different resolution limits are predicted by the Rayleigh and Sparrow criteria. In this section two different microscopy techniques, near-field scanning optical microscopy [89] (NSOM) and confocal microscopy [90], will be evaluated as to which is the better technique for efficiently optically coupling to SNSPDs.

2.4.3 The Rayleigh Criterion

By utilizing the properties of evanescent waves [91, 92] Abbe's diffraction limit [93] can be surpassed. Abbe's diffraction limit states that the resolution of an optical component is limited by the spread of each image point due to diffraction, except if the aperture of the optical component is big enough to collect all of the light that is

diffracted. The optical component's resolution limit d is expressed by the Rayleigh criterion [94]

$$d = \frac{0.61\lambda}{NA} \tag{2.8}$$

where λ is wavelength, NA is the numerical aperture of the optical component, which gives a theoretical limit of ~ $\lambda/2$. The Rayleigh criterion assumes two incoherent point sources emitting as Airy disks [95]. The minimum distance, d, between the two point sources that can be resolved occurs when the maximum of the Airy function of one source falls on the first minimum of the Airy function of the second source (see Figure 2.18). Under these conditions the point sources are said to be *just resolved* (see Figure 2.19). At a distance greater than d, the sources are *fully resolved* and at distances smaller than d, the sources are *not resolved*. The diffraction limit assumes light is in the far-field, so to break this limit, operation has to be in the near-field.

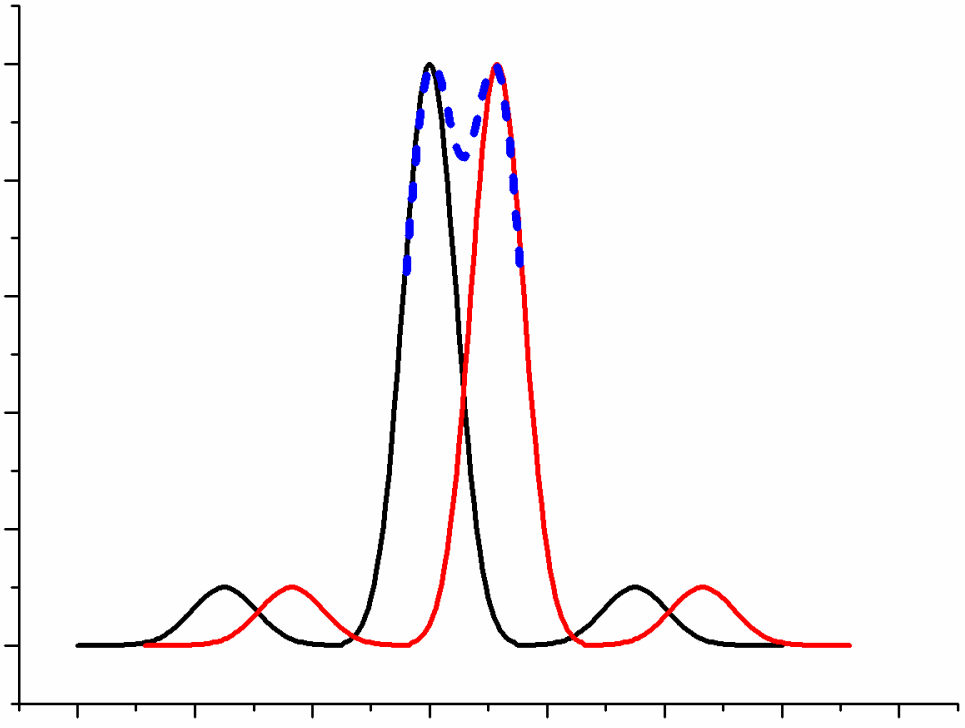

Figure 2.18 – The Rayleigh criterion for overlapping point images. The black and red solid lines are the spatial intensities of two incoherent point sources. The blue dashed line is the observed spatial intensity from both point sources.

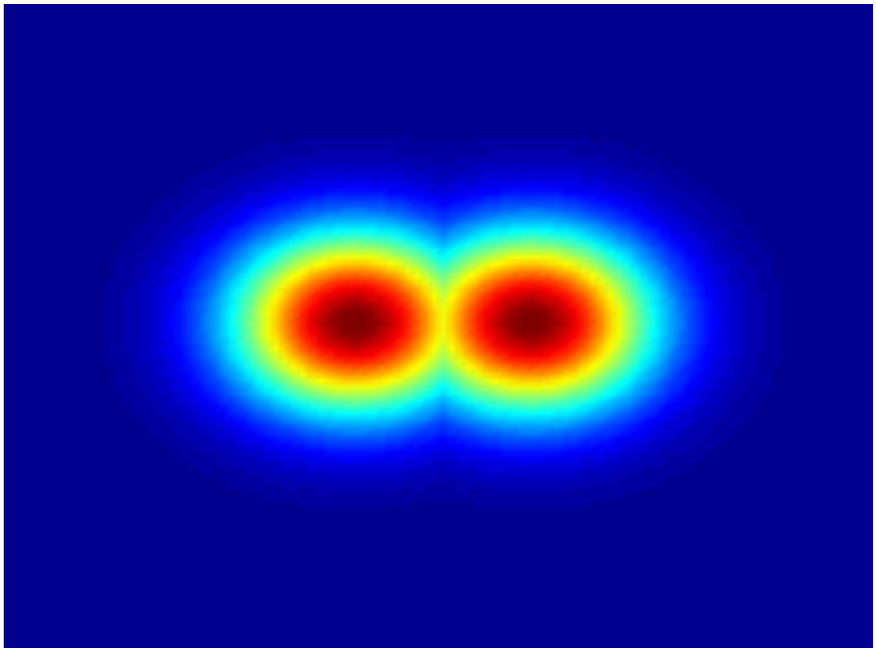

Figure 2.19 – An illustration of the overlapping point images resulting from the Rayleigh criterion.

2.4.4 The Sparrow Criterion

The Sparrow criterion predicts that the spatial resolution limit of light from a sample plane is limited by diffraction. The Sparrow criterion [96] expresses the full width at half maximum (FWHM) of the focal spot

$$FWHM = \frac{0.52\lambda}{NA} \tag{2.9}$$

where NA is the numerical aperture of the objective lens, and λ is the free-space wavelength of the incident light.

The Sparrow criterion varies from the Rayleigh criterion due to the minimum distance which can be resolved (see Figure 2.21) is the point where the saddle point (see Figure 2.18) of the observed intensity has been reduced to a flat top (see Figure 2.20).

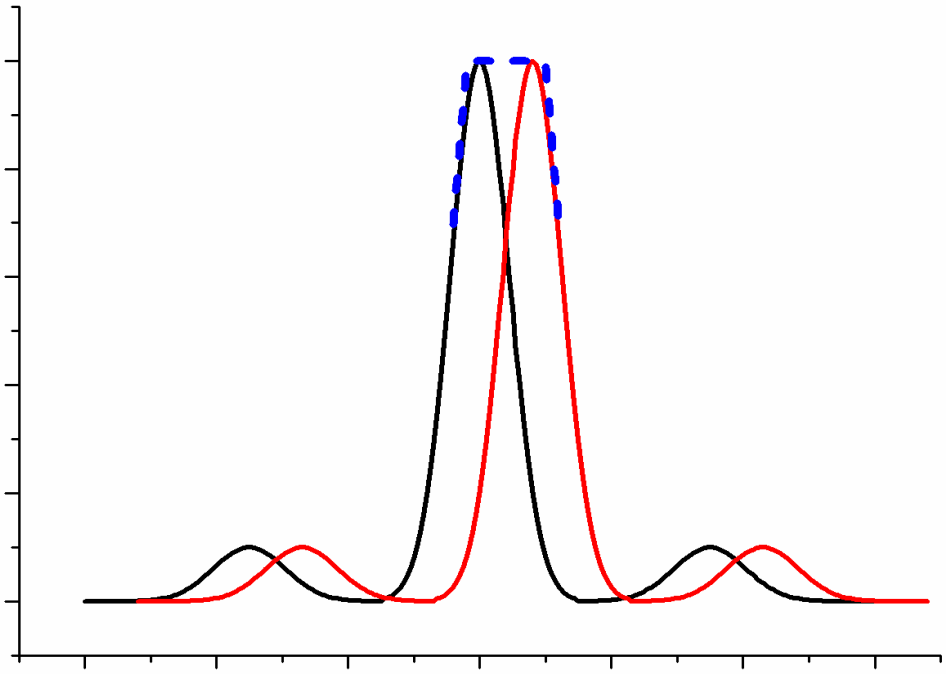

Figure 2.20 – The Sparrow criterion for overlapping point images. The black and red solid lines are the spatial intensities of two incoherent point sources. The blue dashed line is the observed spatial intensity from both point sources.

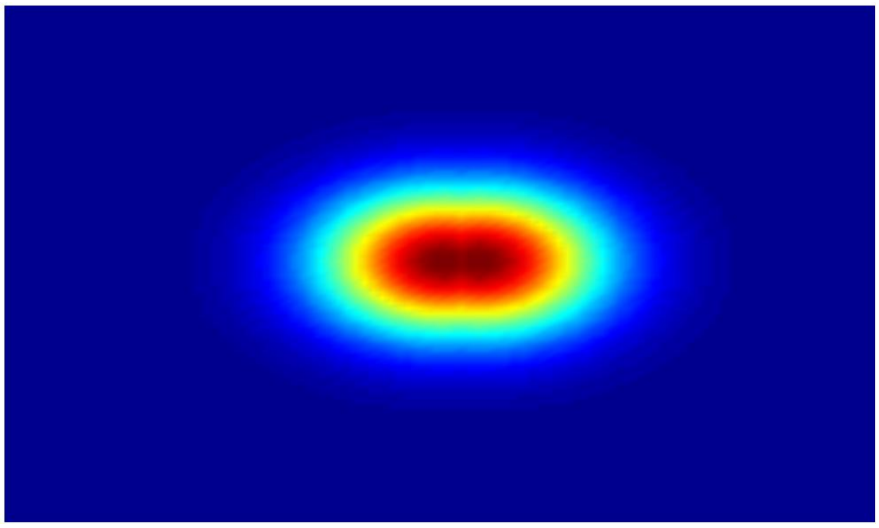

Figure 2.21 – An illustration of the overlapping point images resulting from the Sparrow criterion.

2.4.5 Near-Field Scanning Optical Microscopy (NSOM)

Near-field scanning optical microscopy is a technique that is used for studying structures on the nanoscale. With utilization of the properties of evanescent fields as described in section 2.4.3 a resolution limit predicted by the Rayleigh criterion (equation (2.8)) can be surpassed.

The evanescent fields of the illuminated light are close to the surface under inspection and carry high frequency spatial information about the surface. The intensity of this spatial information drops off exponentially with increasing distance from the surface. This means that the detector must be placed very close to the surface under test and either the sample or the detector moved to image the surface.

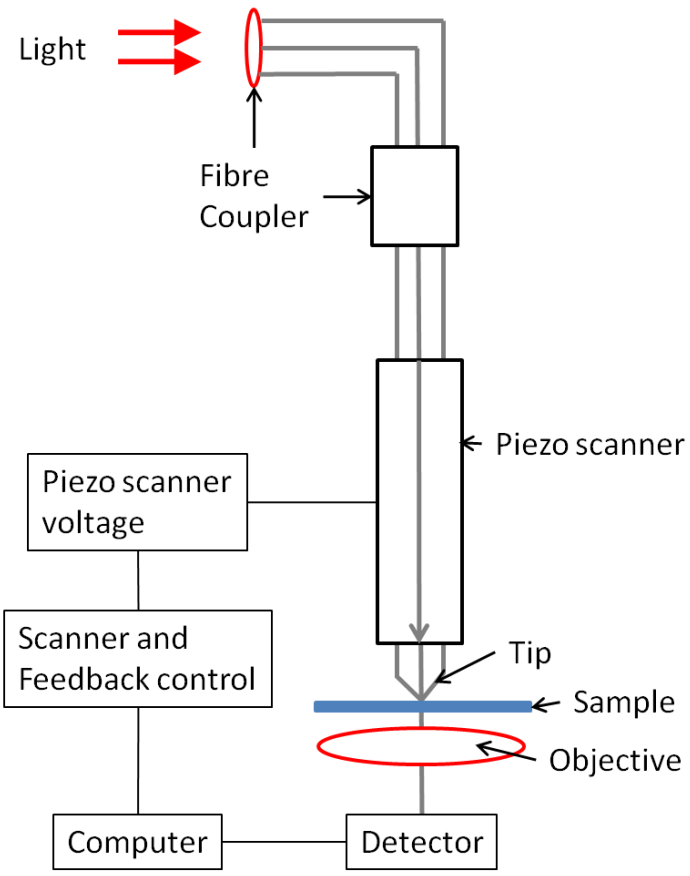

Figure 2.22 – A schematic of a near field scanning optical microscopy (NSOM) setup [97]

The scanning tip is used to illuminate the surface and is either a pulled optical fibre with a metal coating (except at the tip) or a standard AFM cantilever with a hole in the tip.

Common detectors such as SPADs and PMTs can be used. The main advantage of NSOM is the resolution achievable. 20 nm lateral and 2 - 5 nm vertical resolution at 632.8 nm wavelength has been reported [98].

There are several limitations for NSOM. Firstly studies are restricted to surface measurements. In addition the tip can break during scanning, necessitating the replacement of the tip at a considerable time penalty. Furthermore the efficiency of light coupling to the sample surface is highly dependent on the parameters and quality of the tip, which is a major problem when optically coupling to SNSPDs at the single-photon level. The very high resolution achieved by NSOM is offset by the low coupling efficiency. This is why it is not desirable as a method for efficiently coupling light to SNSPDs.

2.4.6 Confocal Microscopy

Confocal microscopy is a technique that provides increased optical resolution and contrast of an illuminated sample. It is widely used in many fields including the spectroscopy of semiconductor quantum dots [99-101] and single molecules [102, 103]. A confocal microscope uses the following simple light collection principle. The theory is that while using point illumination, an aperture (or pinhole) will remove all off-axis and out of focus light providing improved optical resolution compared to wide-field microscopes. The term confocal refers to the optical configuration and thus is valid in the measurements performed in this thesis.

The confocal microscope consists of a simple two lens system. The first lens is a collimating lens, used to collimate the laser beam which is required for optimal performance. The second lens is the objective lens which focuses the laser beam down to a sub-wavelength spot size. The removal of all off axis and out of focus light is achieved by placing an aperture to act as a point source (the end of an optical fibre can be assumed to act as a point source) in the optical system as shown in Figure 2.23, which shows that light is only focused on position A and all other light is eliminated from the system (point B).

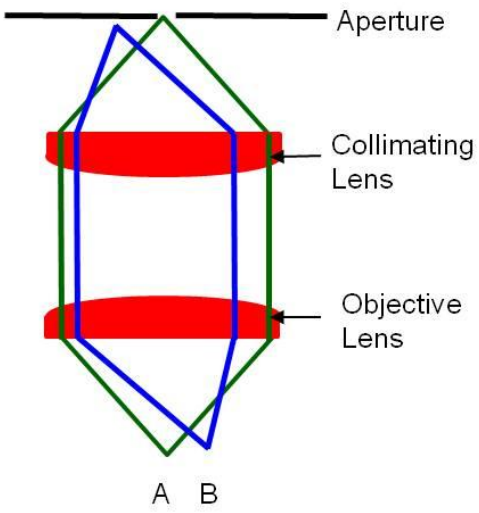

Figure 2.23 – The basic concept of a confocal microscope configuration.

From conventional optics, confocal microscopy provides one of the highest achievable optical spot resolutions. As only the light at the sample plane is imaged, the limit on the spatial resolution in an ideal situation is limited by diffraction. With the aperture (or optical fibre) the system resolution can be approximated using the diffraction limit for a point source. The Sparrow criterion [96] predicts the spatial resolution limit of the confocal microscopy system.

The Sparrow criterion only approximates the focal spot size as the Sparrow criterion assumes that a plane wave is incident upon the optical system, while in fact a Gaussian beam profile is actually incident. This approximation gives a target value for the best achievable diffraction limited spot size. As equation (2.8) describes the limit on the focal spot size, using a larger *NA* lens will allow a smaller focal spot to be attained. Specialized optical components can further decrease the focal spot size achievable; a solid immersion lens (SIL) is one such component.

2.4.7 Solid Immersion Lens (SIL)

Solid immersion microscopy was invented in 1990 by Mansfield and Kino [104], and has gained considerable interest in the field of nano-photonics [105]. It is based on the well-established technique of liquid immersion microscopy, which works by having

both the sample and objective lens in contact with a liquid layer with a refractive index closely matching that of the objective lens. This liquid layer removes two surfaces where refraction occurs, which limits the resolution of an optical microscope. Problems though include an increased probability of dirt and debris contained in the liquid entering the object space. Solid immersion microscopy improved on this technique, by incorporating light that is outside of the critical angle of the system to increase the spatial resolution of the focal spot.

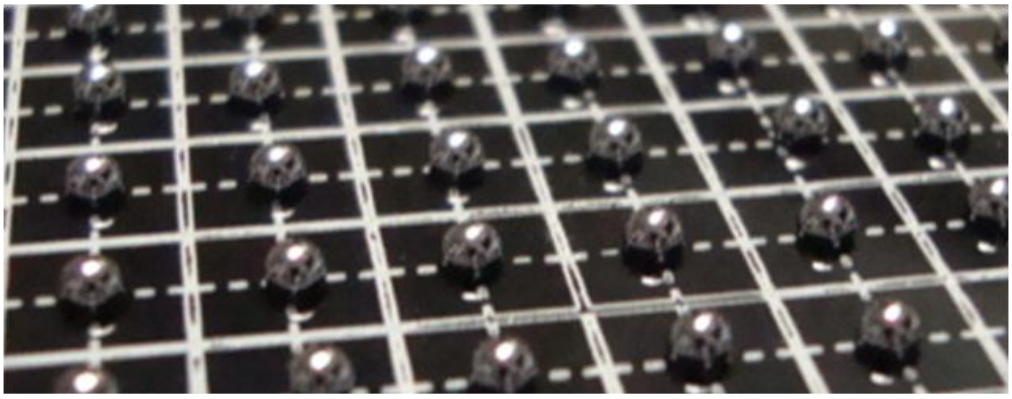

Figure 2.24 – An array of silicon super solid immersion lenses (s-SILs).

Solid immersion lenses (SIL) are used in imaging, characterization and fabrication applications of nanoscale photonic devices [106-109]. Immersion liquids do not have refractive indices that closely match common semiconductors and are undesirable for these applications. There are two types of SIL designs available, the hemispherical SIL and the super SIL.

2.4.8 Hemispherical Solid Immersion Lens (h-SIL)

The SIL proposal came from theory described by Born and Wolf [95]. The theory states that within a high refractive index sphere, of radius *R*, light can be focused without aberrations at two points. These points are the aplanatic points of the sphere.

The first aplanatic position is at the centre of the sphere (see Figure 2.25). The incident rays are at normal incidence to the surface of the sphere, and do not experience refraction at the air-SIL surface. This is the foundation for the design of a

hemispherical SIL (h-SIL). The design is a half sphere with the focus in the centre of the flat surface (see Figure 2.26). An h-SIL is a highly beneficial optical component for studying semiconductor quantum dots, due to the increased collection efficiency and the increased spatial resolution of the system. A magnification factor (and thus a decrease in focal spot size) of the refractive index *n* is introduced into the system. The only limiting factor on focal spot resolution is the *NA* of the objective lens; this improvement can be used to give an approximation of the focal spot size which changes equation (2.9) into

$$FWHM = \frac{0.52\lambda}{nNA} \quad . \qquad \textbf{(2.10)}$$

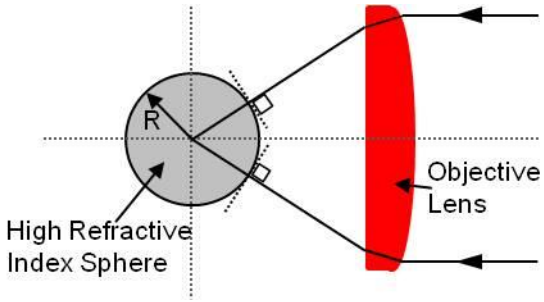

Figure 2.25 – The first aplanatic position of a high refractive index sphere lens.

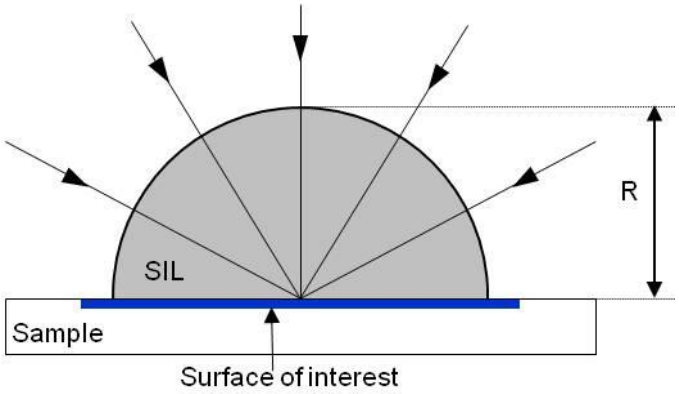

Figure 2.26 – Hemispherical solid immersion lens (h-SIL) diagram.

2.4.9 Super-hemispherical Solid Immersion Lens (s-SIL)

The second aplanatic focal position (Figure 2.27) is taken advantage of in the design of a super-hemispherical solid immersion lens (s-SIL), which is at a position

$z_0 = (n_i / n_0)R$ from the centre of the sphere, where R is the radius of curvature of the sphere, and n_i and n_0 are the refractive indices of the sphere and the air respectively. The incident light rays are refracted at the air-SIL surface to give a tighter focus at z_0. The s-SIL has a virtual focus located at $z_1 = (n_0 / n_i)R$ from the centre of the sphere, which controls the dimensions of the s-SIL (see Figure 2.28). The increased magnification of an s-SIL (also known as a Weierstrass SIL) compared to an h-SIL is a major benefit as is the ability to investigate sub-surface structures.

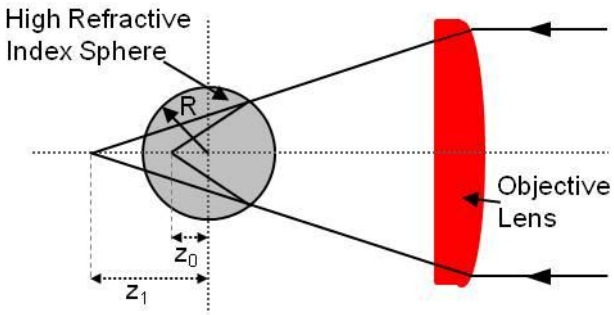

Figure 2.27 – The second aplanatic position of a high refractive index sphere lens.

For effective operation of an s-SIL, it must be designed to achieve the maximum possible *NA* [95, 104, 110], where the maximum *NA* = 1/*n*, where *n* is the refractive index of the sphere. Making the approximate limit of the focal spot size

$$FWHM = \frac{0.52\lambda}{n^2 NA} \qquad \textbf{(2.11)}$$

this simplifies to

$$FWHM = \frac{0.52\lambda}{n} \quad . \qquad \textbf{(2.12)}$$

With consideration of the aplanatic points, the radius of the sphere *R*, *n* its refractive index, *X* the depth of the surface of study, then the physical height of the s-SIL can be calculated using

$$d = R\left(1+\frac{1}{n}\right) - X \quad . \tag{2.13}$$

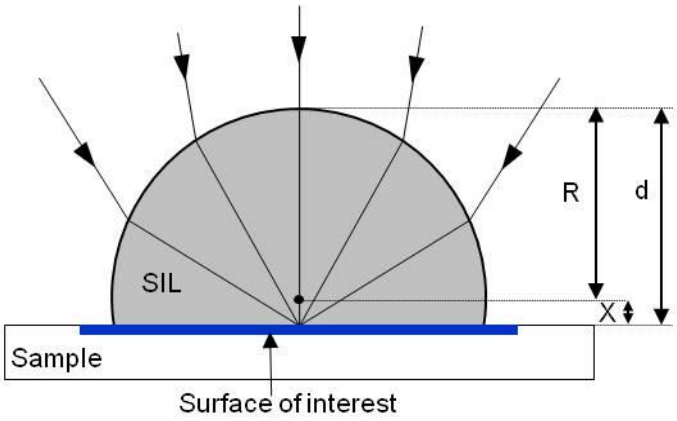

Figure 2.28 – Super hemispherical solid immersion lens (s-SIL) diagram.

Since *n* is wavelength dependent, then the focal position of an s-SIL is wavelength dependent. An h-SIL on the other hand is wavelength independent.

2.5 Conclusion

In conclusion single-photon detectors are a crucial enabling technology in a number of applications at the forefront of scientific research, including QKD, time-of-flight ranging and high speed ground to space communications. Each application places different requirements on detector characteristics in terms of

- Spectral range
- Detection efficiency
- Dark-count rate
- Detector "dead time"
- Timing jitter

There are three main types of single-photon detector. Electron multiplication-based detectors such as photomultiplier tubes (PMTs), and semiconductor-based detectors including single-photon avalanche diodes (SPADs), are both mature technologies with

high performance in the visible spectrum. Superconductor-based detectors, for instance SNSPDs, are at an early stage of development but hold promise for improved performance at telecommunications wavelengths.

The performance of SNSPDs has become more efficient due to the meander design and integration into optical cavities along with robust optical coupling techniques. Fabrication of uniform large area devices is the next step in increasing the performance of SNSPDs. Fibre-coupling is a robust and efficient method for coupling light onto the detectors to achieve good performance. Microscopy techniques, specifically confocal microscopy for efficient optical coupling, can be used along with specialised optical components namely solid immersion lens technology to study localised areas of the detectors.

2.6 Chapter 2 References

1. J. Chen, J.B. Altepeter, M. Medic, K.F. Lee, B. Gokden, R.H. Hadfield, S.W. Nam, and P. Kumar, *Demonstration of a quantum controlled-NOT gate in the telecommunications band.* Physical Review Letters, 2008. **100**(13): p. 133603.
2. C. M. Natarajan, A. Peruzzo, S. Miki, M. Sasaki, Z. Wang, B. Baek, S. Nam, R.H. Hadfield, and J.L. O'Brien, *Operating quantum waveguide circuits with superconducting single-photon detectors.* Applied Physics Letters, 2010. **96**(21): p. 211101.
3. R. H. Hadfield, J.L. Habif, J. Schlafer, R.E. Schwall, and S.W. Nam, *Quantum key distribution at 1550 nm with twin superconducting single-photon detectors.* Applied Physics Letters, 2006. **89**: p. 241129.
4. H. Takesue, S.W. Nam, Q. Zhang, R.H. Hadfield, T. Honjo, K. Tamaki, and Y. Yamamoto, *Quantum key distribution over a 40-dB channel loss using superconducting single-photon detectors.* Nature Photonics, 2007. **1**(6): p. 343-348.
5. A. McCarthy, R.J. Collins, N.J. Krichel, V. Fernandez, A.M. Wallace, and G.S. Buller, *Long-range time-of-flight scanning sensor based on high-speed time-correlated single-photon counting.* Applied Optics, 2009. **48**(32): p. 6241-6251.
6. R. E. Warburton, A. McCarthy, A.M. Wallace, S. Hernandez-Marin, R.H. Hadfield, S.W. Nam, and G.S. Buller, *Subcentimeter depth resolution using a single-photon counting time-of-flight laser ranging system at 1550 nm wavelength.* Optics Letters, 2007. **32**(15): p. 2266-2268.
7. N. J. Krichel, A. McCarthy, and G.S. Buller, *Resolving range ambiguity in a photon counting depth imager operating at kilometer distances.* Optics Express, 2010. **18**(9): p. 9192-9206.
8. R. H. Hadfield, M.J. Stevens, S.S. Gruber, A.J. Miller, R.E. Schwall, R.P. Mirin, and S.W. Nam, *Single photon source characterization with a superconducting single photon detector.* Optics Express, 2005. **13**(26): p. 10846-10853.
9. C. Zinoni, B. Alloing, C. Monat, V. Zwiller, L.H. Li, A. Fiore, L. Lunghi, A. Gerardino, H. de Riedmatten, H. Zbinden, and N. Gisin, *Time-resolved and antibunching experiments on single quantum dots at 1300 nm.* Applied Physics Letters, 2006. **88**(13): p. 131102.

10. B. S. Robinson, A.J. Kerman, E.A. Dauler, R.O. Barron, D.O. Caplan, M.L. Stevens, J.J. Carney, S.A. Hamilton, J.K.W. Yang, and K.K. Berggren, *781 Mbit/s photon-counting optical communications using a superconducting nanowire detector.* Optics Letters, 2006. **31**(4): p. 444-446.
11. E. A. Dauler, B.S. Robinson, A.J. Kerman, V. Anant, R.J. Barron, K.K. Berggren, D.O. Caplan, J.J. Carney, S.A. Hamilton, K.M. Rosfjord, M.L. Stevens, and J.K.W. Yang, *1.25-Gbit/s photon-counting optical communications using a two-element superconducting nanowire single photon detector.* Advanced Photon Counting Techniques, 2006. **6372**: p. U290-U297.
12. B. S. Robinson, A.J. Kerman, E.A. Dauler, D.M. Boroson, S.A. Hamilton, J.K.W. Yang, V. Anant, and K.K. Berggren, *Demonstration of Gigabit-per-second and higher data rates at extremely high efficiency using superconducting nanowire single photon detectors - art. no. 67090Z.* Free-Space Laser Communications Vii, 2007. **6709**: p. Z7090-Z7090.
13. N. Gisin and R. Thew, *Quantum communication.* Nature Photonics, 2007. **1**(3): p. 165-171.
14. N. Gisin, G. Ribordy, W. Tittel, and H. Zbinden, *Quantum cryptography.* Reviews of Modern Physics, 2002. **74**(1): p. 145.
15. R. J. Collins, P.J. Clarke, V. Fernandez, K.J. Gordon, M.N. Makhonin, J.A. Timpson, A. Tahraoui, M. Hopkinson, A.M. Fox, M.S. Skolnick, and G.S. Buller, *Quantum key distribution system in standard telecommunications fiber using a short wavelength single photon source.* Journal of Applied Physics, 2010. **107**(7): p. 073102-6.
16. D. Stucki, N. Walenta, F. Vannel, R. Thew, N. Gisin, H. Zbinden, S. Gray, C.R. Towery, and S. Ten, *High rate, long-distance quantum key distribution over 250 km of ultra low loss fibres.* New Journal of Physics, 2009. **11**(7): p. 075003.
17. N. Gisin, G. Ribordy, H. Zbinden, D. Stucki, N. Brunner, and V. Scarani, *Towards practical and fast quantum cryptography.* arXiv:quant-ph/0411022, 2004.
18. D. Stucki, C. Barreiro, S. Fasel, J.D. Gautier, O. Gay, N. Gisin, R. Thew, Y. Thoma, P. Trinkler, F. Vannel, and H. Zbinden, *High speed coherent one-way quantum key distribution prototype.* arXiv:0809.5264 [quant-ph], 2008.

19. D. Stucki, N. Brunner, N. Gisin, V. Scarani, and H. Zbinden, *Fast and simple one-way quantum key distribution.* Applied Physics Letters, 2005. **87**(19): p. 194108-3.
20. C. H. Bennett and G. Brassard, *Quantum Cryptography: Public key distribution and coin tossing.* Proceedings of the IEEE International Conference on Computers, Systems, and Signal Processing, 1984: p. 175.
21. Chen, F., G.M. Brown, and M. Song, *Overview of three-dimensional shape measurement using optical methods.* Optical Engineering, 2000. **39**(1): p. 10-22.
22. M-C. Amann, T. Bosch, M. Lescure, R. Myllyla, and M. Rioux, *Laser ranging: a critical review of usual techniques for distance measurement.* Optical Engineering, 2001. **40**(1): p. 10-19.
23. C. Mallet and F. Breta, *"Full-waveform topographic lidar: state-of-the-art.* ISPRS Journal of Photogrammetry and Remote Sensing, 2009. **64**: p. 1-16.
24. W. Becker, *Advanced Time-Correlated Single Photon Counting Techniques*. 2005, Springer.
25. J. S. Massa, A.M. Wallace, G.S. Buller, S.J. Fancey, and A.C. Walker, *Laser depth measurement based on time-correlated single-photon counting.* Optics Letters, 1997. **22**(8): p. 543-545.
26. G. S. Buller, R.D. Harkins, A. McCarthy, P.A. Hiskett, G.R. MacKinnon, G.R. Smith, R. Sung, A.M. Wallace, R.A. Lamb, K.D. Ridley, and J.G. Rarity, *Multiple wavelength time-of-flight sensor based on time-correlated single-photon counting.* Review of Scientific Instruments, 2005. **76**(8): p. 083112.
27. H. J. Kimble, M. Dagenais, and L. Mandel, *Photon antibunching in resonance fluorescence.* Physical Review Letters, 1977. **39**(11): p. 691.
28. Th. Basch, W.E. Moerner, M. Orrit, and H. Talon, *Photon antibunching in the fluorescence of a single dye molecule trapped in a solid.* Physical Review Letters, 1992. **69**(10): p. 1516.
29. C. Kurtsiefer, S. Mayer, P. Zarda, and H. Weinfurter, *Stable solid-state source of single photons.* Physical Review Letters, 2000. **85**(2): p. 290.
30. E. Dekel, D. Gershoni, E. Ehrenfreund, D. Spektor, J.M. Garcia, and P.M. Petroff, *Multiexciton spectroscopy of a single self-assembled quantum dot.* Physical Review Letters, 1998. **80**(22): p. 4991.

31. M. Bayer, O. Stern, P. Hawrylak, S. Fafard, and A. Forchel, *Hidden symmetries in the energy levels of excitonic artificial atoms.* Nature, 2000. **405**(6789): p. 923-926.

32. J. A. Timpson, D. Sanvitto, A. Daraei, P.S.S. Guimaraes, H. Vinck, S. Lam, D.M. Whittaker, M.S. Skolnick, A.M. Fox, C.Y. Hu, Y.L.D. Ho, R. Gibson, J.G. Rarity, S. Pellegrini, K.J. Gordon, R.E. Warburton, G.S. Buller, A. Tahraoui, P.W. Fry, and M. Hopkinson, *Single photon sources based upon single quantum dots in semiconductor microcavity pillars.* Journal of Modern Optics, 2007. **54**(2-3): p. 453-465.

33. C. Santori, M. Pelton, G. Solomon, Y. Dale, and Y. Yamamoto, *Triggered single photons from a quantum dot.* Physical Review Letters, 2001. **86**(8): p. 1502.

34. Z. Yuan, B.E. Kardynal, R.M. Stevenson, A.J. Shields, C.J. Lobo, K. Cooper, N.S. Beattie, D.A. Ritchie, and M. Pepper, *Electrically driven single-photon source.* Science, 2002. **295**(5552): p. 102-105.

35. M. B. Ward, O.Z. Karimov, D.C. Unitt, Z.L. Yuan, P. See, D.G. Gevaux, A.J. Shields, P. Atkinson, and D.A. Ritchie, *On-demand single-photon source for 1.3 mu m telecom fiber.* Applied Physics Letters, 2005. **86**(20): p. 201111-3.

36. M. Fox, *Quantum Optics*. 2006: Oxford University Press.

37. S. Seidl, M. Kroner, P.A. Dalgarno, A. Hogele, J.M. Smith, M. Ediger, B.D. Gerardot, J.M. Garcia, P.M. Petroff, K. Karrai, and R.J. Warburton, *Absorption and photoluminescence spectroscopy on a single self-assembled charge-tunable quantum dot.* Physical Review B, 2005. **72**(19): p. 195339

38. P. A. Dalgarno, J. McFarlane, B.D. Gerardot, R.J. Warburton, K. Karrai, A. Badolato, and P.M. Petroff, *Decay dynamics of the positively charged exciton in a single charge tunable self-assembled quantum dot.* Applied Physics Letters, 2006. **89**(4): p. 043107-3.

39. J. A. Mendenhall, L.M. Candell, P.I. Hopman, G. Zogbi, D.M. Boroson, D.O. Caplan, C.J. Digenis, D.R. Hearn, and R.C. Shoup, *Design of an optical photon counting array receiver system for deep-space communications.* Proceedings of the IEEE, 2007. **95**(10): p. 2059-2069.

40. R. Ursin, F. Tiefenbacher, T. Jennewein, and A. Zeilinger, *Applications of quantum communication protocols in real world scenarios toward space.* e & i Elektrotechnik und Informationstechnik, 2007. **124**(5): p. 149-153.
41. C. Gobby, Z.L. Yuan, and A.J. Shields, *Quantum key distribution over 122 km of standard telecom fiber.* Applied Physics Letters, 2004. **84**(19): p. 3762-3764.
42. K. M. Rosfjord, J.K.W. Yang, E.A. Dauler, A.J. Kerman, V. Anant, B.M. Voronov, G.N. Gol'tsman, and K.K. Berggren, *Nanowire single-photon detector with an integrated optical cavity and anti- reflection coating.* Optics Express, 2006. **14**(2): p. 527-534.
43. K. J. Gordon, V. Fernandez, P.D. Townsend, and G.S. Buller, *A short wavelength GigaHertz clocked fiber-optic quantum key distribution system.* IEEE Journal of Quantum Electronics, 2004. **40**(7): p. 900-908.
44. B. S. Robinson, D.O. Caplan, M.L. Stevens, R.J. Barron, E.A. Dauler, and S.A. Hamilton, *1.5-photons/bit photon-counting optical communications using Geiger-mode avalanche photodiodes*. 2005 Digest of the LEOS Summer Topical Meetings. 2005, New York: IEEE. 41-42.
45. E. A. Dauler, B.S. Robinson, A.J. Kerman, J.K.W. Yang, K.M. Rosfjord, V. Anant, B. Voronov, G. Gol'tsman, and K.K. Berggren, *Multi-element superconducting nanowire single-photon detector.* IEEE Transactions on Applied Superconductivity, 2007. **17**(2): p. 279-284.
46. E. Dauler, R. Molnar, A.J. Kerman, and B.S. Robinson, *High-fidelity photon-number-resolution using multi-element superconducting nanowire single photon detectors.* 2008 Conference on Lasers and Electro-Optics & Quantum Electronics and Laser Science Conference, Vols 1-9, 2008: p. 3229-3230.
47. G. A. Morton, *Photomultipliers for scintillation counting.* RCA Review, 1949. **10**: p. 525–553.
48. V. K. Zworykin, G.A. Morton, and L. Malter, *The secondary-emission multiplier-a new electronic device.* Proceedings of the IRE, 1936. **24**: p. 351-375.
49. J. L. Wiza, *Microchannel plate detectors.* Nuclear Instruments & Methods, 1979. **162**(1-3): p. 587-601.
50. *http://jp.hamamatsu.com/resources/products/etd/pdf/m-h7422e.pdf (Date Accessed 15th March 2011).*

51. E. Hergert, *Near-infrared photodetectors enable new applications.* Laser Focus World, 2004. **40**: p. 131-133.
52. R. A. La Rue, K.A. Costello, C.A. Davis, J.P. Edgecumbe, and V.W. Aebi, *Photon counting III-V hybrid photomultipliers using transmission mode photocathodes.* IEEE Transactions on Electron Devices, 1997. **44**(4): p. 672-678.
53. *http://jp.hamamatsu.com/resources/products/etd/pdf/NIR-PMT_APPLI_TPMO1040E02.pdf (Date Accessed 15th March 2011).*
54. S. Cova, A. Longoni, and A. Andreoni, *Towards picosecond resolution with single-photon avalanche diodes.* Review of Scientific Instruments, 1981. **52**(3): p. 408-412.
55. M. Ghioni, A. Gulinatti, I. Rech, F. Zappa, and S. Cova, *Progress in silicon single-photon avalanche diodes.* Selected Topics in Quantum Electronics, IEEE Journal of, 2007. **13**(4): p. 852-862.
56. J. P. Donnelly, E.K. Duerr, K.A. McIntosh, E.A. Dauler, D.C. Oakley, S.H. Groves, C.J. Vineis, L.J. Mahoney, K.M. Molvar, P.I. Hopman, K.E. Jensen, G.M. Smith, S. Verghese, and D.C. Shaver, *Design considerations for 1.06-μm InGaAsP-InP Geiger-mode avalanche photodiodes.* IEEE Journal of Quantum Electronics, 2006. **42**(8): p. 797-809.
57. M. A. Itzler, R. Ben-Michael, C.F. Hsu, K. Slomkowski, A. Tosi, S. Cova, F. Zappa, and R. Ispasoiu, *Single photon avalanche diodes (SPADs) for 1.5 mu m photon counting applications.* Journal of Modern Optics, 2007. **54**(2-3): p. 283-304.
58. *Perkin Elmer SPAD http://optoelectronics.perkinelmer.com/content/RelatedLinks/SpecificationSheets/SPC_PhotoDetectors.pdf (Date Accessed 15th March 2011).*
59. G. S. Buller and R.J. Collins, *Single-photon generation and detection.* Measurement Science & Technology, 2009. **21**(1): p. 012002.
60. R. G. W. Brown, K.D. Ridley, and J.G. Rarity, *Characterization of silicon avalanche photodiodes for photon correlation measurements. 1: Passive quenching.* Applied Optics, 1986. **25**(22): p. 4122-4126.

61. S. Cova, M. Ghioni, A. Lacaita, C. Samori, and F. Zappa, *Avalanche photodiodes and quenching circuits for single-photon detection.* Applied Optics, 1996. **35**(12): p. 1956-1976.
62. P. Antognetti, S. Cova, and A. Longoni, *A study of the operation and performance of an avalanche diode as a single-photon detector*. Proceedings of the 2nd ISPRA Nuclear Electronic Symposium, 1975: p. 453-456.
63. A. E. Lita, A.J. Miller, and S.W. Nam, *Counting near-infrared single-photons with 95% efficiency*. Optics Express, 2008. **16**(5): p. 3032-3040.
64. D. Rosenberg, A.E. Lita, A.J. Miller, and S.W. Nam, *Noise-free high-efficiency photon-number-resolving detectors.* Physical Review A, 2005. **71**(6): p. 061803.
65. S. Reif-Acherman, *Heike Kamerlingh Onnes: Master of experimental technique and quantitative research.* Physics in Perspective (PIP), 2004. **6**(2): p. 197-223.
66. H. Kamerlingh Onnes, *Further experiments with liquid helium. C. On the change of electric resistance of pure metals at very low temperatures, etc. IV. The resistance of pure mercury at helium temperatures.* Communications from the Physical Laboratory of the University of Leiden, 1911. **No. 120b**.
67. H. Kamerlingh Onnes, *Further experiments with liquid helium. D. On the change of electric resistance of pure metals at very low temperatures, etc. V. The disappearance of the resistivity of mercury.* Communications from the Physical Laboratory of the University of Leiden, 1911. **No. 122b**.
68. L. N. Cooper, *Bound electron pairs in a degenerate fermi gas.* Physical Review, 1956. **104**(4): p. 1189.
69. J. Bardeen, L.N. Cooper, and J.R. Schrieffer, *Microscopic theory of superconductivity.* Physical Review, 1957. **106**(1): p. 162.
70. J. R. Waldram, *Superconductivity of Metals and Cuprates*. 1996, Institute of Physics Publishing (Bristol and Philadelphia, Pa.)
71. *University of Cambridge. Teaching and Learning Packages.* *http://www.doitpoms.ac.uk/tlplib/superconductivity/discovery.php (Date Accessed 19th April 2011).*
72. D. Bonnet, S. Erlenkämper, H. Germer, and H. Rabenhorst, *A new measurement of the energy gap in superconducting niobium.* Physics Letters A, 1967. **25**(6): p. 452-453.

73. K. Komenou, T. Yamashita, and Y. Onodera, *Energy gap measurement of niobium nitride.* Physics Letters A, 1968. **28**(5): p. 335-336.

74. V. Moshchalkov, M. Menghini, T. Nishio, Q.H. Chen, A.V. Silhanek, V.H. Dao, L.F. Chibotaru, N.D. Zhigadlo, and J. Karpinski, *Type-1.5 Superconductivity.* Physical Review Letters, 2009. **102**(11): p. 117001.

75. R. T. Kao, S.J. Wang, S.P. Chen, J.Y. Juang, K.H. Wu, T.M. Uen, and Y.S. Gou, *Single electron tunneling and superconducting energy gap in $YBa_2Cu_3O_7$-δ and $TlBa_2Ca_2Cu_3O_9^+$-δ films.* Physica C: Superconductivity, 1997. **282-287**(Part 3): p. 1531-1532.

76. G. N. Gol'tsman, O. Okunev, G. Chulkova, A. Lipatov, A. Semenov, K. Smirnov, B. Voronov, A. Dzardanov, C. Williams, and R. Sobolewski, *Picosecond superconducting single-photon optical detector.* Applied Physics Letters, 2001. **79**(6): p. 705-707.

77. A. Verevkin, J. Zhang, R. Sobolewski, A. Lipatov, O. Okunev, G. Chulkova, A. Korneev, K. Smirnov, G.N. Gol'tsman, and A. Semenov, *Detection efficiency of large-active-area NbN single-photon superconducting detectors in the ultraviolet to near-infrared range.* Applied Physics Letters, 2002. **80**(25): p. 4687-4689.

78. S. Miki, M. Fujiwara, M. Sasaki, B. Baek, A.J. Miller, R.H. Hadfield, S.W. Nam, and Z. Wang, *Large sensitive-area NbN nanowire superconducting single-photon detectors fabricated on single-crystal MgO substrates.* Applied Physics Letters, 2008. **92**(6): p. 061116.

79. S. Miki, M. Fujiwara, M. Sasaki, and Z. Wang, *NbN superconducting single-photon detectors prepared on single-crystal MgO substrates.* IEEE Transactions on Applied Superconductivity, 2007. **17**(2): p. 285-288.

80. R. H. Hadfield, P.A. Dalgarno, J.A. O'Connor, E. Ramsay, R.J. Warburton, E.J. Gansen, B. Baek, M.J. Stevens, R.P. Mirin, and S.W. Nam, *Submicrometer photoresponse mapping of nanowire superconducting single-photon detectors.* Applied Physics Letters, 2007. **91**(24): p. 241108.

81. M. G. Tanner, C.M. Natarajan, V.K. Pottapenjara, J.A. O'Connor, R.J. Warburton, R.H. Hadfield, B. Baek, S. Nam, S.N. Dorenbos, E.B. Urena, T. Zijlstra, T.M. Klapwijk, and V. Zwiller, *Enhanced telecom wavelength single-*

photon detection with NbTiN superconducting nanowires on oxidized silicon. Applied Physics Letters, 2010. **96**(22): p. 221109.

82. C. Shinho, *Inductance measurements in $YBa_2Cu_3O_7$ thin films.* Superconductor Science and Technology, 1997. **10**(8): p. 594.
83. A. J. Kerman, E.A. Dauler, J.K.W. Yang, K.M. Rosfjord, V. Anant, K.K. Berggren, G.N. Gol'tsman, and B.M. Voronov, *Constriction-limited detection efficiency of superconducting nanowire single-photon detectors.* Applied Physics Letters, 2007. **90**(10): p. 101110.
84. V. L. Ginzburg and L.D. Landau, Journal of Experimental and Theoretical Physics., 1950. **20**: p. 1064.
85. *SMF-28e optical fiber, www.corning.com.*
86. *http://www.ozoptics.com/ALLNEW_PDF/DTS0080.pdf (Date Accessed 15th March 2011).*
87. X. L. Hu, T. Zhong, J.E. White, E.A. Dauler, F. Najafi, C.H. Herder, F.N.C. Wong, and K.K. Berggren, *Fiber-coupled nanowire photon counter at 1550 nm with 24% system detection efficiency.* Optics Letters, 2009. **34**(23): p. 3607-3609.
88. S. Miki, T. Yamashita, M. Fujiwara, M. Sasaki, and Z. Wang, *Multichannel SNSPD system with high detection efficiency at telecommunication wavelength.* Optics Letters, 2010. **35**(13): p. 2133-2135.
89. B. Hecht, B. Sick, U.P. Wild, V. Deckert, R. Zenobi, O.J.F. Martin, and D.W. Pohl, *Scanning near-field optical microscopy with aperture probes: Fundamentals and applications.* The Journal of Chemical Physics, 2000. **112**(18): p. 7761-7774.
90. R. H. Webb, Reports on Progress in Physics, 1996. **59**: p. 427.
91. H. Nassenstein, *Superresolution by diffraction of subwaves.* Optics Communications, 1970. **2**(5): p. 231-234.
92. E. A. Ash and G. Nicholls, *Super-resolution aperture scanning microscope.* Nature, 1972. **237**(5357): p. 510-512.
93. E. Abbe, *A contribution to the theory of the microscope and the nature of microscopic vision.* Proceedings of the Bristol Naturalists' Society 1874. **1**: p. 200-261.
94. L. Rayleigh, Philosophical Magazine, 1879. **5**(8): p. 261.

95. M. Born and E. Wolf, *Principles of Optics*. 7th ed. 2002: Cambridge University Press, Cambridge.
96. C. M. Sparrow, *On spectroscopic resolving power.* The Astrophysical Journal, 1916. **44**: p. 76.
97. D. W. Pohl, W. Denk, and M. Lanz, *Optical stethoscopy: Image recording with resolution λ/20.* Applied Physics Letters, 1984. **44**(7): p. 651-653.
98. Y. Oshikane and et al., *Observation of nanostructure by scanning near-field optical microscope with small sphere probe.* Science and Technology of Advanced Materials, 2007. **8**(3): p. 181.
99. V. Zwiller and G. Bjork, *Improved light extraction from emitters in high refractive index materials using solid immersion lenses.* Journal of Applied Physics, 2002. **92**(2): p. 660-665.
100. S. Moehl, H. Zhao, B.D. Don, S. Wachter, and H. Kalt, *Solid immersion lens-enhanced nano-photoluminescence: Principle and applications.* Journal of Applied Physics, 2003. **93**(10): p. 6265-6272.
101. P. A. Dalgarno, J. McFarlane, B.D. Gerardot, R.J. Warburton, K. Karrai, A. Badolato, and P.M. Petroff, *Decay dynamics of the positively charged exciton in a single charge tunable self-assembled quantum dot.* Applied Physics Letters, 2006. **89**(4): p. 043107.
102. M. J. Rossow, J.M. Sasaki, M.A. Digman, and E. Gratton, *Raster image correlation spectroscopy in live cells.* Nature Protocols, 2010. **5**(11): p. 1761-1774.
103. L. M. Davis, B.K. Canfield, J.A. Germann, J.K. King, W.N. Robinson, A.D. Dukes, S.J. Rosenthal, P.C. Samson, and J.P. Wikswo, *Four-focus single-particle position determination in a confocal microscope*, Single Molecule Spectroscopy and Imaging Iii, J. Enderlein, Z.K. Gryczynski, and R. Erdmann, Editors. 2010. p. 757112.
104. S. M. Mansfield and G.S. Kino, *Solid immersion microscope.* Applied Physics Letters, 1990. **57**(24): p. 2615-2616.
105. K. A. Serrels, E. Ramsay, P.A. Dalgarno, B.D. Gerardot, J.A. O'Connor, R.H. Hadfield, R.J. Warburton, and D.T. Reid, *Solid immersion lens applications for nanophotonic devices.* Journal of Nanophotonics, 2008. **2**: p. 021854.

106. B. B. Goldberg, S.B. Ippolito, L. Novotny, L. Zhiheng, and M.S. Unlu, *Immersion lens microscopy of photonic nanostructures and quantum dots.* IEEE Journal of Quantum Electronics, 2002. **8**(5): p. 1051-1059.

107. A. N. Vamivakas, R.D. Younger, B.B. Goldberg, A.K. Swan, M.S. Unlu, E.R. Behringer, and S.B. Ippolito, *A case study for optics: The solid immersion microscope.* American Journal of Physics, 2008. **76**(8): p. 758-768.

108. Z. Liu, B.B. Goldberg, S.B. Ippolito, A.N. Vamivakas, M.S. Unlu, and R. Mirin, *High resolution, high collection efficiency in numerical aperture increasing lens microscopy of individual quantum dots.* Applied Physics Letters, 2005. **87**(7): p. 071905.

109. E. Ramsay, N. Pleynet, D. Xiao, R.J. Warburton, and D.T. Reid, *Two-photon optical-beam-induced current solid-immersion imaging of a silicon flip chip with a resolution of 325 nm.* Optics Letters, 2005. **30**(1): p. 26-28.

110. M. Baba, T. Sasaki, M. Yoshita, and H. Akiyama, *Aberrations and allowances for errors in a hemisphere solid immersion lens for submicron-resolution photoluminescence microscopy.* Journal of Applied Physics, 1999. **85**(9): p. 6923-6925.

Chapter 3 Experimental Techniques

3.1 Introduction

The fabrication, testing and study of superconducting nanowire single-photon detectors (SNSPD) requires many different techniques and methods, including nano-lithography, optical coupling and microscopy, and electrical and optical characterization techniques. In this chapter the multistep nanofabrication process (section 3.2) for producing bare SNSPD chips using electron beam (e-beam) lithography and reactive ion etching (RIE) will be explained. The thermal mounting and electrical connection of bare SNSPD chips using wire bonding is detailed in section 3.3. Nano-optical techniques for studying localized areas of SNSPDs specifically a confocal microscopy configuration will be discussed in detail. The design and ideas behind two different (sections 3.4 and 3.6) confocal microscopy configurations will be detailed. The advantages and disadvantages of each method along with detailed resolution performance measurements are presented. Closed-cycle refrigeration technology used as the method to cool the SNSPDs is detailed in section 3.5. Electrical and optical characterization measurements on SNSPDs (section 3.7), which include current – voltage, kinetic inductance and degree of constriction, and detection efficiency measurements are discussed. Finally scanning measurements (section 3.8) that can be performed using both confocal microscopy configurations including detection efficiency, jitter and pulse timing delay mapping are detailed, giving insight to the underlying device physics of SNSPDs.

3.2 Superconducting Nanowire Single-Photon Detector Fabrication

Superconducting nanowire single-photon detectors (SNSPD) have been explained in section 0. The fabrication process for producing SNSPDs (see Figure 3.2 to Figure 3.6) is a multi step process employing many nano-fabrication techniques. Our collaborators Dr Shigehito Miki and Dr Zhen Wang at the National Institute of Information and Communications Technology (NICT) in Japan fabricated the bare SNSPD chips used.

SNSPDs consist of an ultrathin niobium nitride (NbN) film patterned into a wire on a magnesium oxide (MgO) substrate. For a fast response speed from the SNSPD, the ultrathin film must be of high quality. High quality thin films of NbN must be epitaxially grown and for this purpose a substrate which is lattice matched to NbN is required. NbN has a lattice constant of 4.38 Å [1], which is closely matched to the lattice constant of MgO of 4.13 Å [2]. Reactive dc-magnetron sputtering is the technique used to deposit the NbN film [3]. The sputtering process is performed in an atmosphere of Argon (Ar) and Nitrogen (N_2) gas with a relative ratio of 5:1. Sputtering occurs via the bombardment of ions or neutral particles, in this case ionized argon (Ar^+) atoms. A target of niobium (Nb) is contained inside the Ar and N_2 atmosphere, and a negative voltage (typically greater than -300V) is applied to the target. This accelerates the Ar^+ ions towards the target. NbN is formed as Nb atoms are dislodged from the target. The single crystal MgO substrate is used to promote and seed the epitaxial growth of the ultrathin NbN film (see Figure 3.1). This process is continued until the desired film thickness (~ 4 nm) is reached. The critical temperature T_c is measured using a 4-point probe resistance measurement. This measurement is carried out to determine firstly if the film superconducts and secondly that T_c is high enough for a practical device to operate successfully.

Figure 3.1 – The NbN film is grown on a MgO substrate.

Figure 3.2 – The ZEP 520 electron beam resist is spun on top of the NbN film.

The patterning of the meander structure of the nanowire is the next step. A layer of electron beam resist is spin coated onto the NbN film (see Figure 3.2). Spin coating is a

method of quickly coating a sample with an even layer with the use of centrifugal force. The sample is attached to a rod in the centre of the spin coater and is then rotated at the desired speed (typically 20 - 80 Hz), the resist is dropped onto the sample where most is thrown off of the sample. The remaining resist is spread out evenly across the sample under the centrifugal force produced by the spinning. The electron beam resist used is ZEP 520. This is a positive resist which means that the exposed sections of ZEP 520 are removed when developed. Electron beam (e-beam) lithography is used to pattern the meander structure into the ZEP 520 (see Figure 3.3). The e-beam breaks cross-links between polymer molecules; this allows the exposed areas to be removed with a developer. ZEP 520 is a good choice for this as it allows nanoscale features to be made.

Figure 3.3 – The meander pattern of the SNSPD patterned in ZEP 520 electron beam resist.

At this point the meander pattern is in the ZEP 520 but not the NbN. Reactive ion etching (RIE) is used to remove the exposed areas of NbN (see Figure 3.4). RIE uses chemically reactive plasma (Tetrafluoromethane, CF_4) to etch materials from sample surfaces. The plasma contains high energy ions which react with and remove the surface material. In this case, the NbN film is patterned into a meander (see Figure 3.5). The ZEP 520 electron beam resist is removed by dissolving in dimethylacetamide.

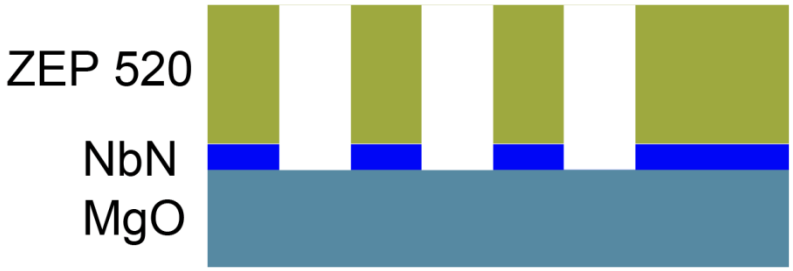

Figure 3.4 – Reactive Ion Etch of NbN through the ZEP 520 electron beam resist mask.

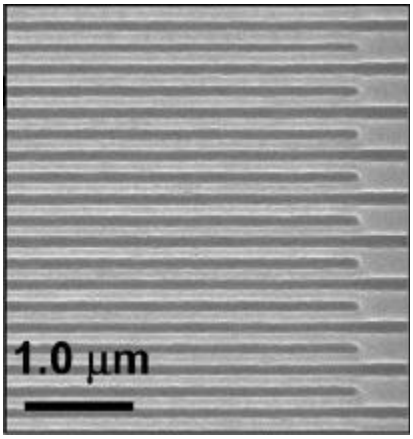

Figure 3.5 – A scanning electron micrograph (SEM) of a SNSPD [4]

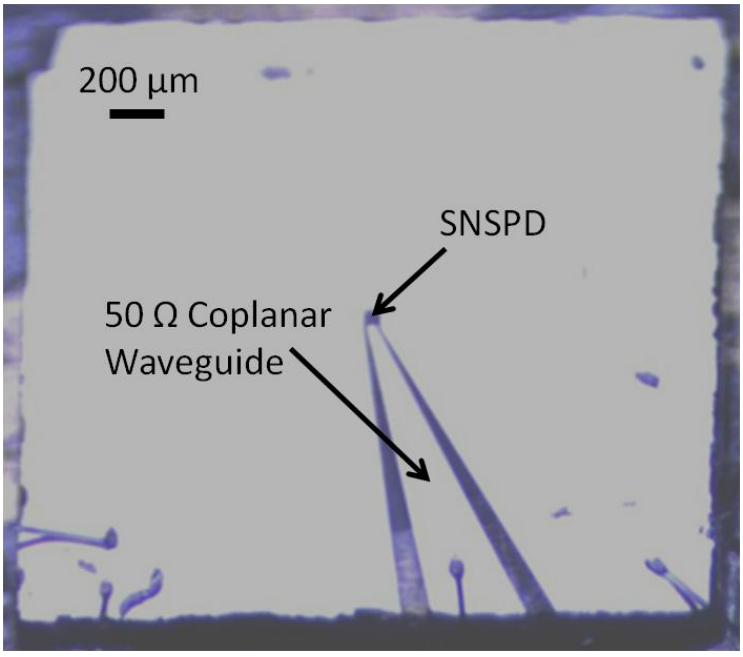

Figure 3.6 – An optical stereo microscope image of a SNSPD device embedded in a 50 Ω coplanar waveguide for readout of high speed pulses.

3.3 Sample Preparation and Contacting

SNSPD chips were prepared and mounted for testing at Heriot-Watt University. Bare SNSPD chip preparation and electrical contacting is required to operate the detector. SNSPD chips with a MgO substrate must be stored in a desiccator. This is because MgO reacts with moisture in the air to form magnesium hydroxide ($Mg(OH)_2$) which is detrimental for the SNSPD. A processed chip as described in section 3.2 may have some small specks of dirt or remains of photoresist on its surface. These could either

short circuit the device; or cover the photosensitive area of the device preventing optical coupling. Rinsing the chip in acetone and isopropanol (IPA) removes the dirt and dissolves and removes any remaining resist. Optical inspection using a high magnification stereo microscope is used to check the surface after cleaning to determine if cleaning has to be repeated.

Efficient thermal contact of the SNSPD chip with a copper sample mount is required for effective cooling when used both in liquid helium and closed cycle systems. Thermal contact is achieved by one of two methods. In the first method, a beryllium copper clip is securely clamped to the sample mount and tightly grips a corner of the chip. This not only provides thermal contact but also firmly holds the chip in place. For applications where anything sticking out higher than the top of the chip prevents the operation or investigation of the device another method must be chosen. In the second method a thermally conducting paste to stick down and firmly hold the chip in position. Ideally a paste that survives a large number of thermal cycles is chosen. Thermally conducting silver paste is a solution but one problem with silver paste is that if too much is used some particles can migrate to the surface of the chip short-circuiting the device. Using clear nail varnish overcomes this problem and can be removed by soaking the sample in acetone.

Electrical connection is achieved by ultrasonic wire bonding (wirebonder model Kulicke & Soffa Model 4123) of aluminium (Al) wires (diameter ~ 100 μm) to the 50 Ω coplanar waveguide (CPW) which connects to the SNSPD. Al wire is preferred to gold (Au) wire as no sample heating is required. Delicate test samples (such as superconducting devices) may be damaged by heating during bonding. Wire bonding is a technique used for contacting mm scale devices, including semiconductor devices and printed circuit boards. Wire bonding, specifically wedge bonding provides a sturdy and repeatable electrical connection. The aluminium wire is threaded through the tip of the needle of the wirebonder, the tip (see Figure 3.7) is brought in contact with the bond pad.

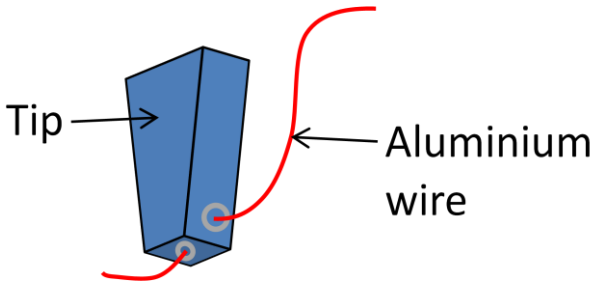

Figure 3.7 – A schematic of the ultrasonic wire bonding tip

Ultrasonic energy is applied to the wire while it is under contact with the desired amount of force. This produces the first bond. The tip is then moved to the second position that is to be connected and the procedure is repeated to make the second bond. At this point the wire is clamped breaking the wire to leave the completed bond. Bonds are made on the central connection of the 50 Ω coplanar waveguide and the ground connection (see Figure 3.6 and Figure 3.8). This provides the sample mount with external electrical connections used for reading out signals from the SNSPD. The electrical connections from the sample mount to the readout circuitry used for counting photons are made using coaxial cable. In each of the confocal microscopy configurations a different type of coaxial cable was implemented. Medical grade coaxial cable was used in the liquid helium confocal microscopy configuration as it is flexible and has a small diameter (0.127 mm). Without these properties, the cable would prevent the piezoelectric linear positioners and scanner from moving. Semi flexible brass coaxial cable was used in the miniaturized confocal microscope configuration as moveable optics was chosen. Brass coaxial cable was chosen as it has good high speed electrical properties coupled with a low thermal conductivity, which is ideal for studying SNSPDs.

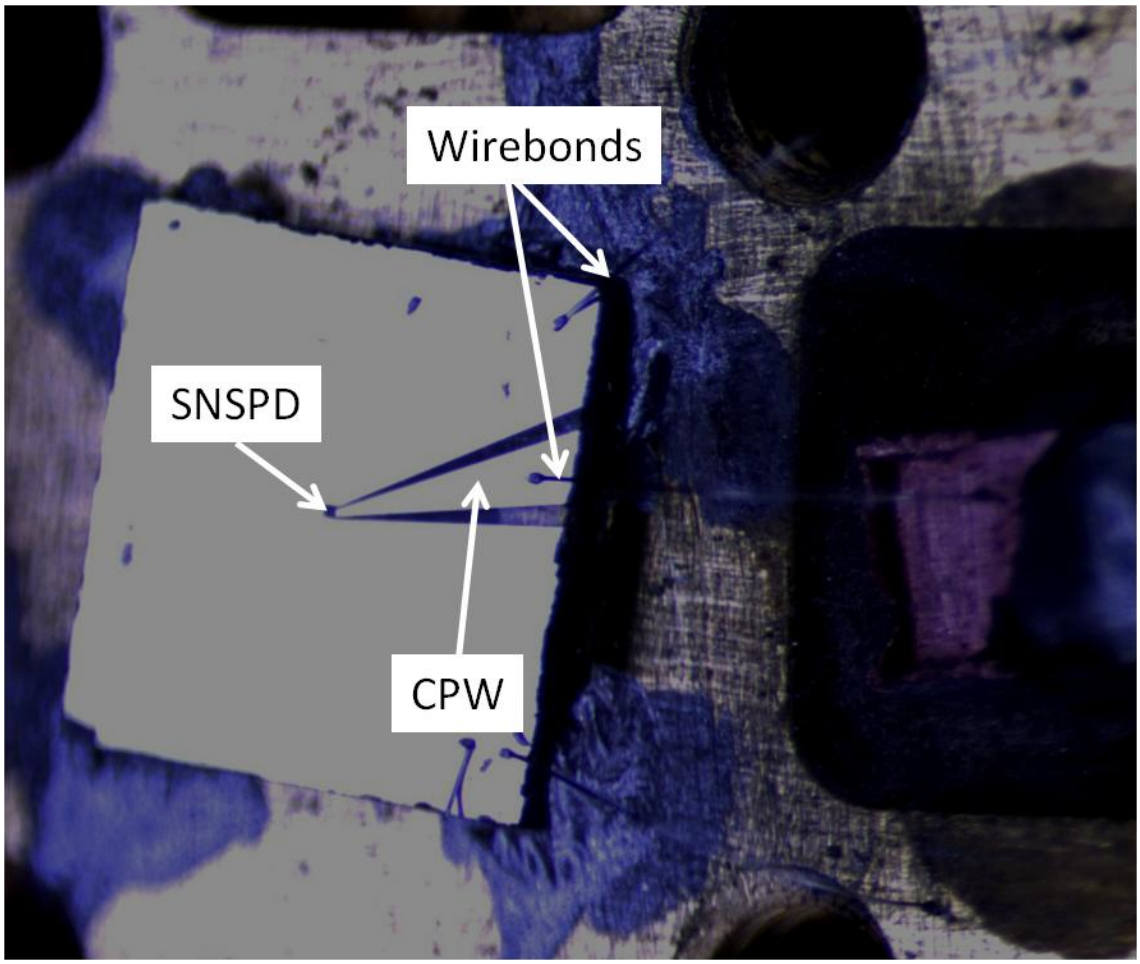

Figure 3.8 – A stereo optical microscope image of wirebonded SNSPD on a gold plated copper sample mount.

3.4 Confocal Microscopy Configuration

Confocal microscopy has previously been explained in section 2.4.6. It provides a high optical resolution using conventional optical components whilst still maintaining efficient optical coupling. Confocal microscopy is used here as a basis for achieving high spatial resolution and efficient optical coupling to a SNSPD sample.

3.4.1 Optics

Using the end of an optical fibre as a point source and a simple two lens optical system a confocal microscopy configuration can be produced. For the two lens optical system aspheric lenses are chosen due to their reduced aberrations (spherical aberrations are

reduced or eliminated, but other optical aberrations are increased). The choice of optical components is crucial to achieving the desired performance. The important characteristics that require close matching are numerical aperture (*NA*) and clear aperture values. Standard single mode optical fibres have a *NA* ~ 0.14 [5]. To ensure efficient optical coupling the *NA* of the collimating lens should be equal to or greater than the *NA* of the optical fibre. As seen in the Sparrow Criterion (equation 2.9) for high optical resolution the objective lens (second lens) should have a large *NA*. The clear aperture (see Figure 3.9) is the maximum amount of light that an optical component will allow through and is usually quoted as a diameter.

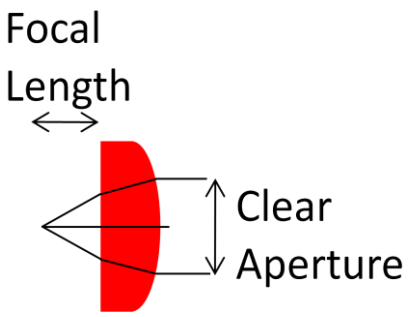

Figure 3.9 – An illustration of the clear aperture of aspheric lens.

For efficient coupling the clear aperture of both the collimating and objective lenses must be similar. These considerations put limits on the achievable resolution. A Thorlabs™ C280 lens was chosen as the collimating lens and Thorlabs™ C390 lens was chosen as the objective lens. The clear apertures for the lenses are 5.5 and 3.6 mm respectively, this difference was accepted as it allowed the objective lens to have a high *NA* of 0.68. These lenses were chosen for use in the experiments in Chapter 4 performed at visible and near infrared wavelengths.

A microscope head is used to deliver the light to the confocal microscopy configuration (see Figure 3.10 and Figure 3.11). Within the head there is a 5 mm thick piece of uncoated BK7 glass which, due to the refractive index mismatch between glass and air (1.4 and 1 respectively), acts as a beam-splitter. Light from the end of the optical fibre is collimated by the collimating lens using a Z-axis translation mount (Thorlabs™ SM1Z) which has sub µm accuracy. The objective lens is centred in the collimated beam on the optical axis. To achieve high optical spot resolution, the optical system

must be correctly focused. The reflected light from the sample travels back up the microscope and is reflected by the beam-splitter and focused onto a CCD camera or a power meter. By observing the reflected signal either a focused spot is observed on the camera or is determined by a peak in the reflected signal power (see Figure 3.12). This peak in the reflected signal drops off away from the focal point of the system; this is controlled by moving the sample in the Z-axis.

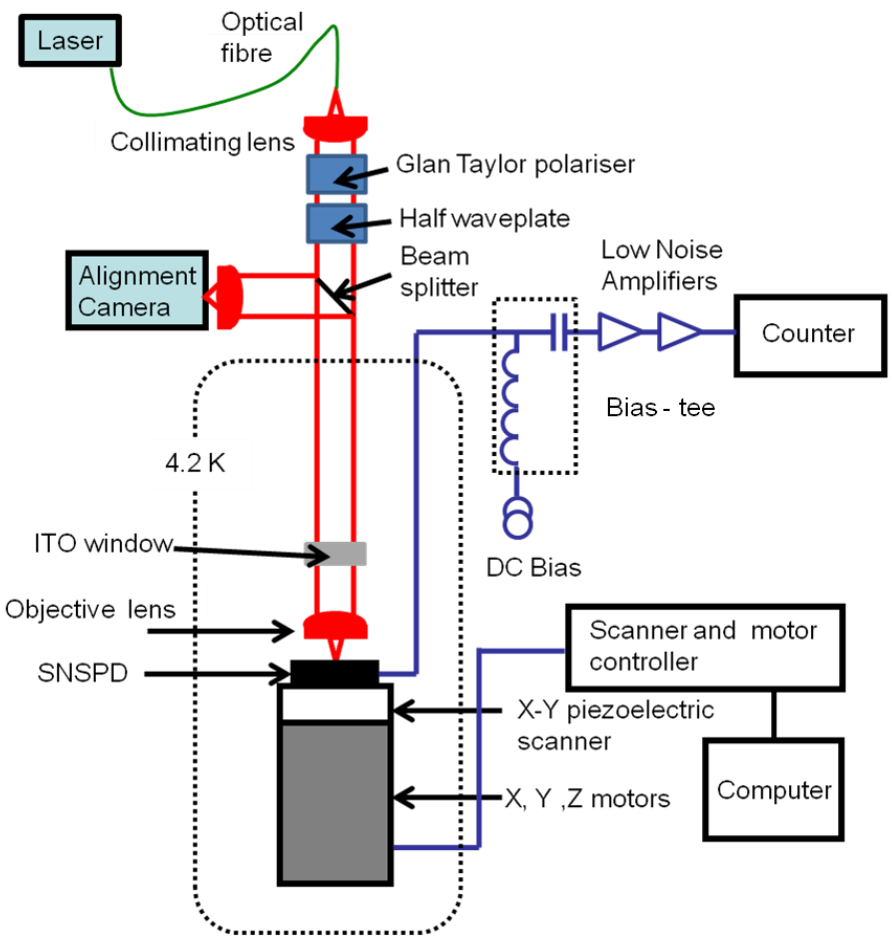

Figure 3.10 – A schematic of the liquid helium confocal microscope configuration. The collimating lens and the objective lens make up the confocal microscope configuration. The Glan Taylor polariser and the half waveplate are used to control the polarisation state of the incident light. The cooled ITO (Indium Tin Oxide) window removes undesirable blackbody radiation. The X, Y and Z motors are piezoelectric linear positioners and are used for focusing and aligning the focal spot from the confocal microscope configuration to the SNSPD with the aid of the alignment camera. A piezoelectric X-Y scanner is used to raster scan the focal spot across the area of the SNSPD or to precisely locate the focal spot on a specified position on the SNSPD. The SNSPD is biased and the fast output voltage pulses are read out through the bias – Tee, with the fast output voltage pulses being amplified with low noise room temperature amplifiers. The counter detects the amplified voltage pulses.

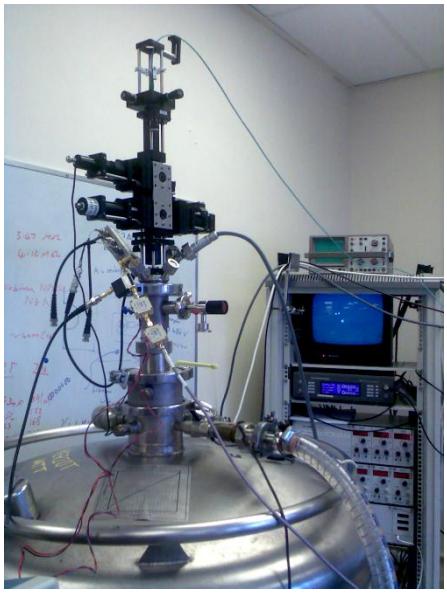

Figure 3.11 – A photograph of liquid helium confocal microscopy configuration. The upper part of the microscope head is visible. The lower part is inserted into the liquid helium dewar.

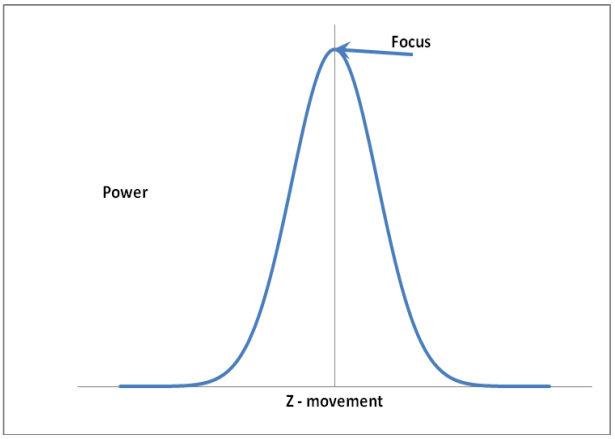

Figure 3.12 – Variation in reflected power in relation to focal position.

3.4.2 Sample Positioners and Scanner

Figure 3.13 shows the sample under test mounted on a set of X,Y,Z linear piezoelectric positioners (Attocube™ ANP 101 series), and a large area X-Y piezoelectric scanner (Attocube™ ANS 100 series). The linear positioners are used for alignment and focusing of the sample. The linear positioners have a maximum movement range of 5 mm, with a minimum movement step size of ~ 50 nm at room temperature and

~ 5 nm at 4 K. The X-Y scanner covers a 40 µm x 40 µm area at 300 K and a 30 µm x 30 µm area at 4 K.

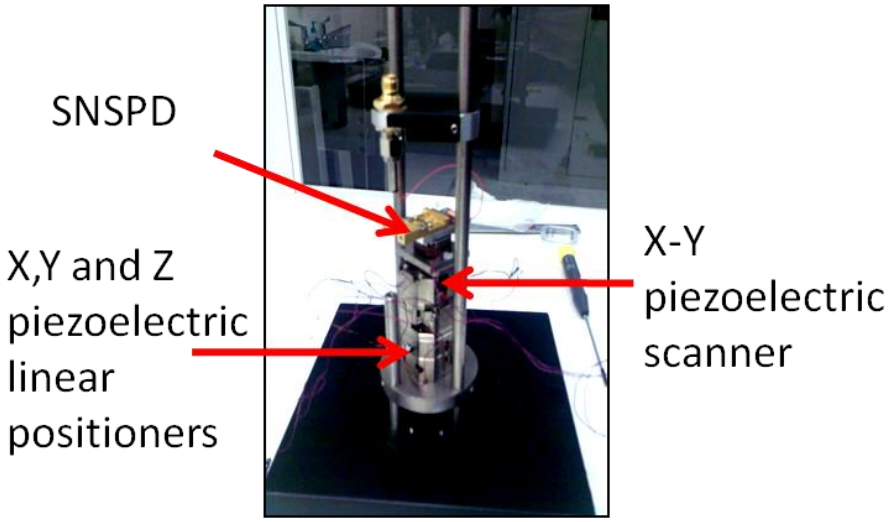

Figure 3.13 – A SNSPD sample mounted atop a stack of X, Y and Z piezoelectric linear positioners, and a piezoelectric X-Y scanner.

Each linear positioner contains a stack of multiple piezoelectric elements which moves using a slip-stick operation. A saw-tooth voltage pulse is applied to the motor. As the voltage slowly increases the piezoelectric stack expands moving the motor stage. Upon the sudden voltage decrease, the piezoelectric stack quickly shrinks but the motor stage does not move (see Figure 3.14). The applied saw-tooth voltage maximum value (Vmax) varies between 0 – 70 V. The applied voltage pulse is repeated for further movement at a desired frequency (up to 1 kHz). The use of piezoelectric stacks means that the movement of the motors contains some non-linearity and hysteresis when used with a constant voltage pulse stream. Since the linear positioners are used for alignment and focusing at a specific position this is not a problem.

The X-Y piezoelectric scanner contains one piece of piezoelectric material for each axis. An applied voltage expands the piezoelectric material and moves the scanner stage. Upon reduction of the applied voltage, the scanner stage moves back towards its start position. The applied voltage increases from 0 V and reaches a maximum of 60 V at room temperature and 150 V at 4 K, providing maximum movement of 40 µm and 30 µm at room temperature and 4 K respectively. This movement is repeatable and has negligible hysteresis. The movement resolution is sub-nm step sizes [6].

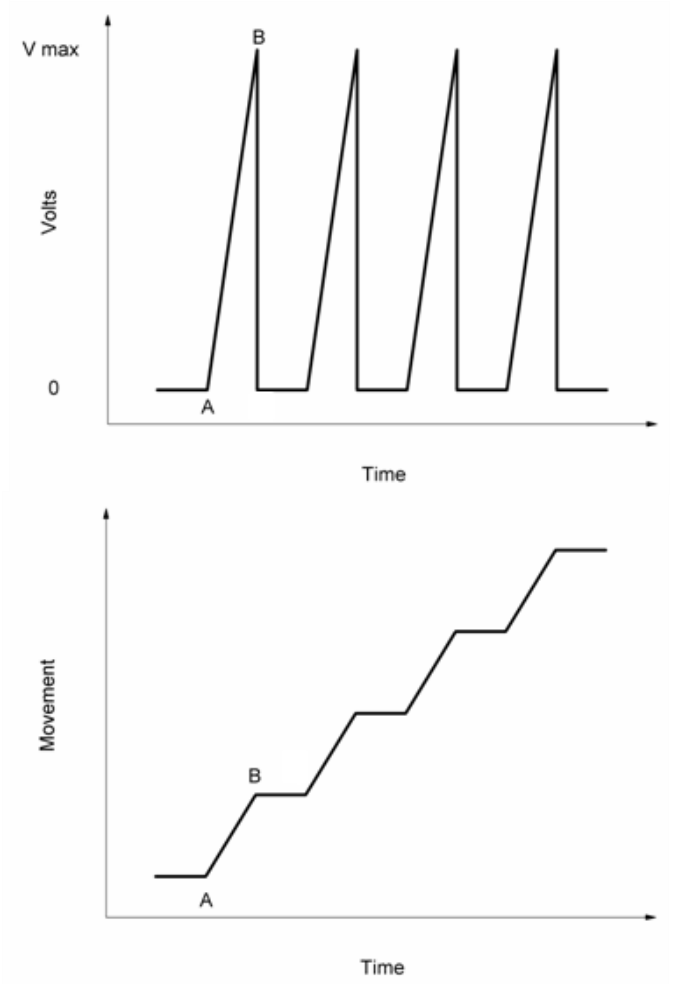

Figure 3.14 – Control and movement of the piezoelectric linear positioners. Top - Applied sawtooth voltage to piezoelectric linear positioners, Bottom – Piezoelectric linear positioner stage movement with the applied sawtooth voltage.

The linear positioners with the sample attached were tightly secured to the bottom of the microscope. The whole lower part of the microscope was then carefully placed inside a steel tube. The steel tube was put under vacuum (~ 10^{-5} mbar) and some He exchange gas was introduced to provide a thermal link to the steel tube. The steel tube was lowered into a liquid helium dewar which is used to achieve cooling down to 4 – 5 K. Due to the microscope head being outside the liquid helium dewar an optical window was required for the delivery of light. This can introduce blackbody heating of the sample. To reduce the blackbody heating, a cooled ITO (indium tin oxide) window was placed in the collimated beam to reflect the "hot" blackbody radiation allowing a lower sample temperature to be achieved. The top part of the microscope was at room temperature and thus is also a source of blackbody radiation. Using this method a

sample can be maintained at a temperature of 4 – 5 K for approximately 3 weeks in a 60 litre liquid helium dewar.

3.4.3 Resolution Tests

In order to determine the optical performance of the system and to find possible ways to improve the resolution crucial room temperature resolution tests were carried out. It has been observed that there is no difference in resolution achieved when comparing room temperature and cryogenic temperature measurements in the liquid helium confocal microscopy configuration.

To carry out the resolution tests, the focal spot is scanned across an interface between a reflective and transparent surface, whilst measuring the transmitted signal (see Figure 3.15). The transmitted signal is measured using a silicon (Si) photodiode. The differential of the transmitted signal provides a direct measurement of the spot size as it is scanned across the interface. The X-Y scanner is used to move the spot across the interface and the movement is controlled by applying a DC voltage from a lock-in amplifier. A lock-in amplifier (Signal Recovery™ Model 7265) is used to add an AC component of 127.483 Hz and 0.01 V amplitude to the DC voltage. This AC component dithers the position and the photodetector signal can be locked in giving a direct measure of dT/dx, where T is the transmitted signal and x is the position. This method reduces the noise in the system, giving a more accurate measurement. A lock-in frequency of 127.483 Hz was chosen as it is not an integer multiple of 50 Hz or 1 Hz (the frequency of electrical mains noise and a significant room vibration respectively).

In the resolution measurements a 4 μm period aluminium/glass checkerboard was used. A 470 nm wavelength CW laser and a silicon photodetector were also selected. Novel optical components were also chosen, these included h-SILs (section 2.4.8), s-SILs (section 2.4.9) and pupil-function engineering components [7] (annuluses and centre blocked apertures see Figure 3.19). Systematic resolution measurements were carried out with and without the novel optical components that theoretically (from the Sparrow criterion [8]) give a decreased spot size. dV/dx is measured rather than dT/dx because

the photodetector gives a current output which undergoes a pre-amplification stage converting it to a voltage whilst magnifying the size of the signal. Normalization of *dV/dx* is analogous to using a normalized *dT/dx*.

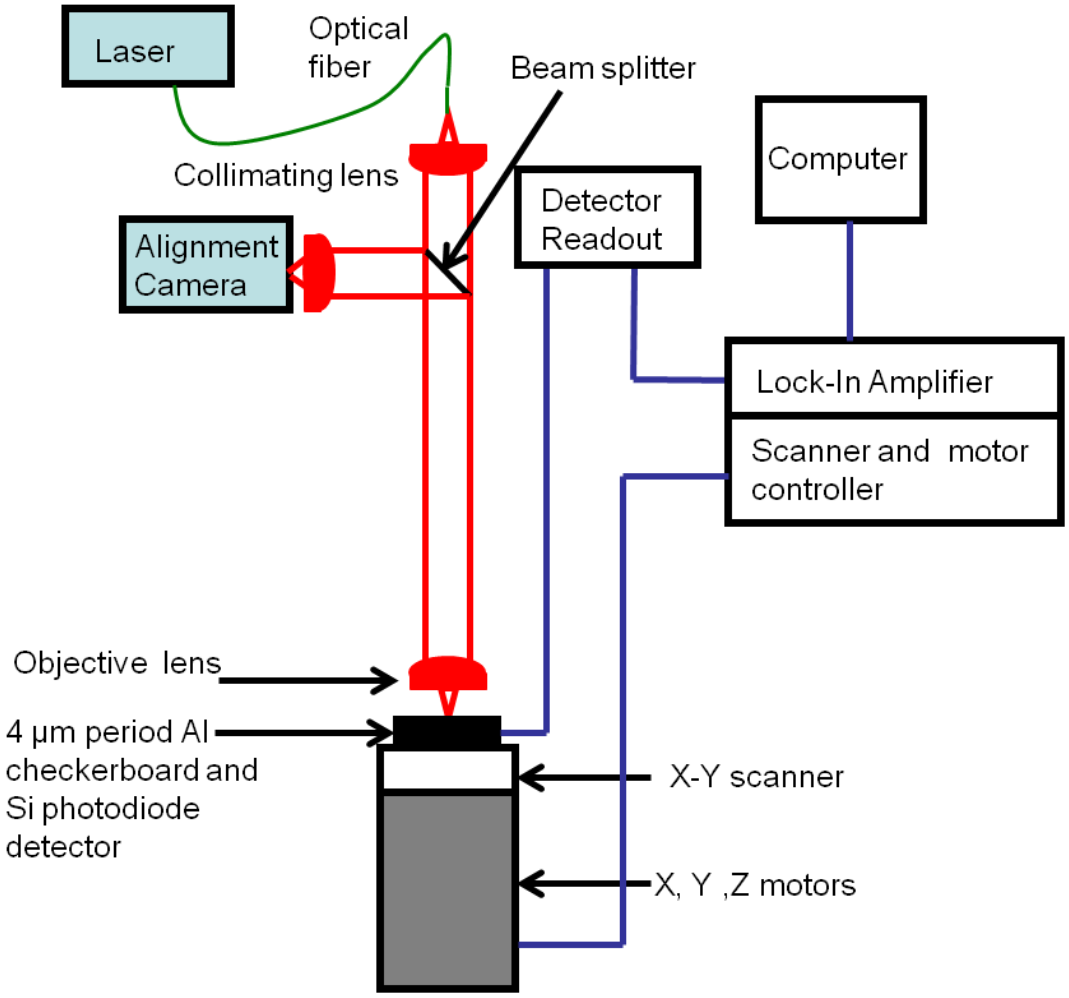

Figure 3.15 – The resolution test setup for the liquid helium confocal microscopy configuration.

The first configuration was to just have an objective lens. This lens, a C110TM lens, has an *NA* of 0.4; this is different from the lens previously chosen - this will be explained below. From the Sparrow criterion the spot size limit is 611 nm at λ = 470 nm.

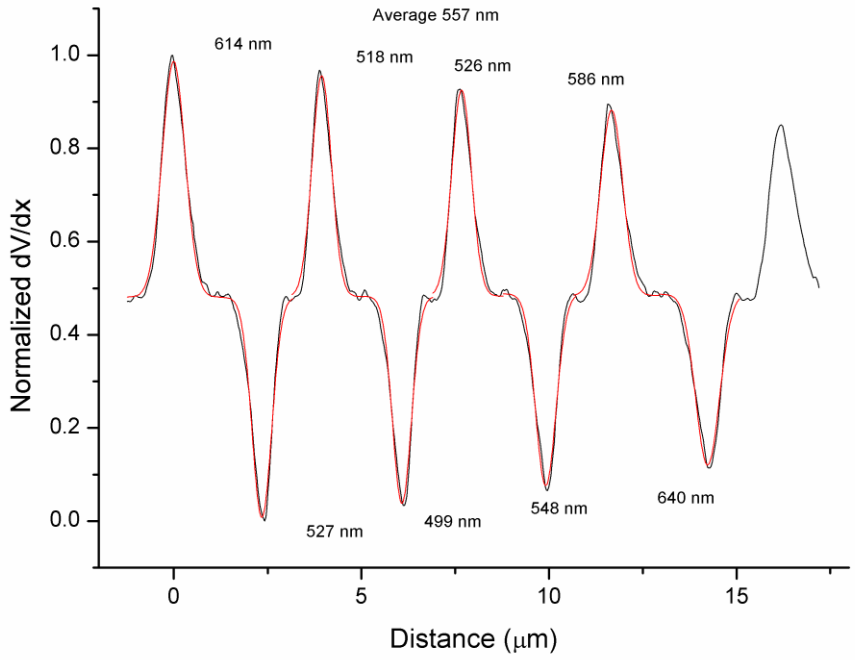

Figure 3.16 – A resolution test of the confocal microscope configuration using 470 nm wavelength laser, an objective lens with NA = 0.65 and a 4 μm period checkerboard. The red curve is the Gaussian fit. FWHM value of 556 ± 48 nm was achieved

The Gaussian curves of each edge profile are fitted and the average full width at half maximum (FWHM) value is 556 ± 48 nm at λ = 470 nm (see Figure 3.16), which matches within the experimental error the theoretical value predicted by the Sparrow criterion for a plane wave.

The next configuration tested was using an objective lens with an *NA* of 0.65 and a hemispherical solid immersion lens (h-SIL). h-SILs (as detailed in section 2.4.8) provide a reduction in the focal spot by a factor of the refractive index *n*. A glass h-SIL with n = 2 and a height of 1 mm was selected. The working distance of the objective lens has to be equal to or greater than the height of the h-SIL; in this case the working distance is 1.56 mm. To get optimum functionality from the h-SIL, careful focusing on the first aplanatic position is required. Focusing is achieved by first focusing onto the top of the h-SIL, and the light is then focused through the h-SIL to the first aplanatic point.

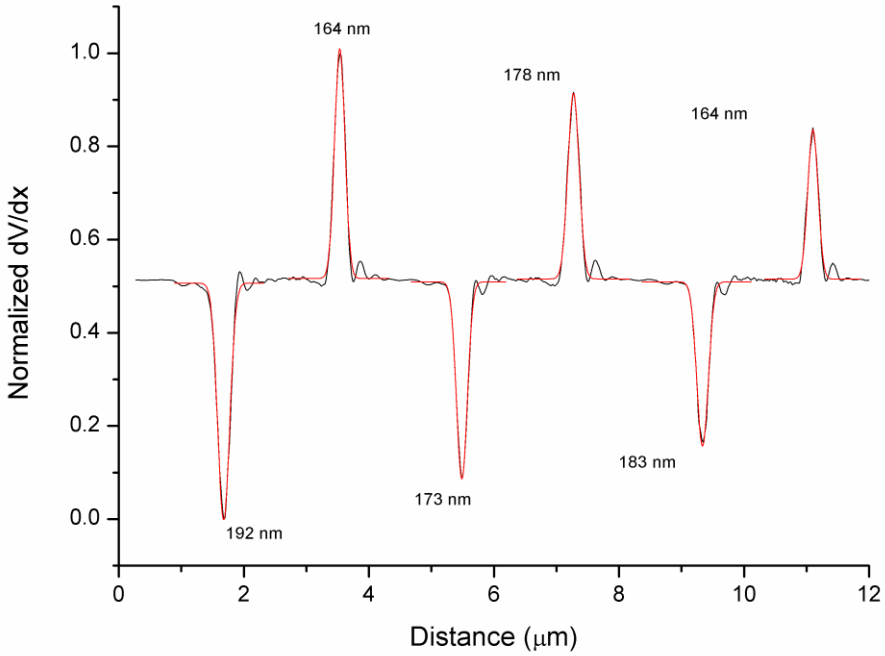

Figure 3.17 – A resolution test using a 470 nm wavelength laser a hemispherical solid immersion lens, an objective lens with NA = 0.65 and a 4 μm period checkerboard. The red curve is the Gaussian fit. FWHM of 176 ± 11 nm was achieved.

The averaged value of the FWHM of the Gaussian fit is 176 ± 11 nm at λ = 470 nm (see Figure 3.17), which is comparable to the theoretical estimate of 188 nm. This shows the advantages of using h-SILs to reduce the focal spot size.

Using a super-hemispherical solid immersion lens (s-SIL) as detailed in section 2.4.9 requires careful selection of the objective lens. With the maximum possible *NA* being inversely proportional to the refractive index *n* (*NA* = 1/*n*), using a high *n* s-SIL reduces the maximum *NA* of the objective lens used. The s-SILs used here are made from zirconia with *n* = 2.15, giving a maximum possible *NA* of 0.46. For commercially available lenses the best match found is an *NA* of 0.4. This is the reason for using an objective lens with a *NA* of 0.4, as we can compare the resolution achieved with and without a s-SIL. As for the h-SIL precise focusing of the system is required for optimal performance. The only difference between an h-SIL and an s-SIL is that when focusing through the s-SIL there is a virtual focus at the first aplanatic position; this must also be focused through as the second aplanatic position is the desired focus.

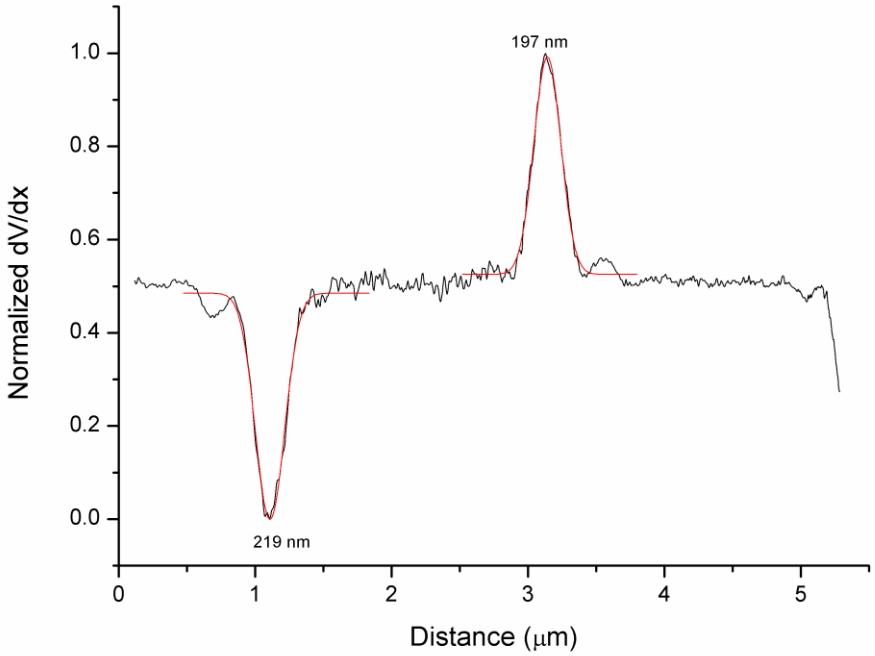

Figure 3.18 – A resolution test using a 470 nm wavelength laser, a super-hemispherical solid immersion lens (s-SIL), an objective lens with *NA* = 0.4 and a 4 μm period checkerboard. The red curve is the Gaussian fit. FWHM of 208 ± 16 nm was achieved.

The measured FWHM spot size using a zirconia s-SIL and objective lens with 0.4 *NA* is 208 ± 16 nm (see Figure 3.18), which is significantly larger than the predicted value of 129 nm at λ = 470 nm. It was concluded that the available s-SILs do not work at short wavelengths, most likely due to either defects in the manufacturing process, or more likely chromatic aberrations. These defects are most likely to cause aberrations at short wavelengths and thus the s-SILs are not as effective as predicted. This conclusion was reached after first determining that the s-SIL was not defective, as the same effect was seen in other tested s-SILs from the same batch. Likewise at λ = 633 nm the same degradation in resolution was observed, but at λ = 950 nm the s-SIL worked as expected.

This unexpected result prevented us from trying to reduce the spot size by rotating the linear polarization of the light. This technique only works by using high incident ray angles as seen with the use of s-SILs. The polarization rotation method produces a highly asymmetric spot profile, which would produce a decrease in spot size in the

direction perpendicular to the electric field [9]. This has been observed in two-photon systems [10], giving a reduction to 70% of the value predicted by the Sparrow Criterion.

The use of pupil-function engineering in reducing the spatial spot size compared to the clear-pupil situation has been reported [7, 11]. The basic principle behind pupil-function engineering is to keep the input light rays at high *NA* and to reject those at low *NA*. This is achieved by the manipulation of the irradiance distribution within the pupil-plane on the objective lens. This manipulation is carried out on the three-dimensional (3D) electromagnetic energy distribution. The manipulation will give a tighter central focal spot and result in a greater depth of focus. However this method may also lead to the introduction of detrimental side lobes which can lessen the advantages of this technique for imaging.

To determine the improvement in resolution, ease of use and the extent of the lobes a 2 mm diameter annulus and a 2 mm diameter centre blocked aperture (see Figure 3.19) were tested by placing them separately in the collimated beam path.

The implementation of the annulus or centre blocked aperture component is tricky and takes time and care to achieve optimum performance. The component is centred in the optical axis of the collimated beam (between the collimating and objective lens). This has to be very accurate as slight misalignment reduces the effectiveness of the component.

The use of an h-SIL and objective lens with an *NA* of 0.65 yielded the smallest focal spot in the previous tests (Figure 3.17). Due to this the annulus or centre blocked aperture is inserted to this system to determine the improvement in resolution.

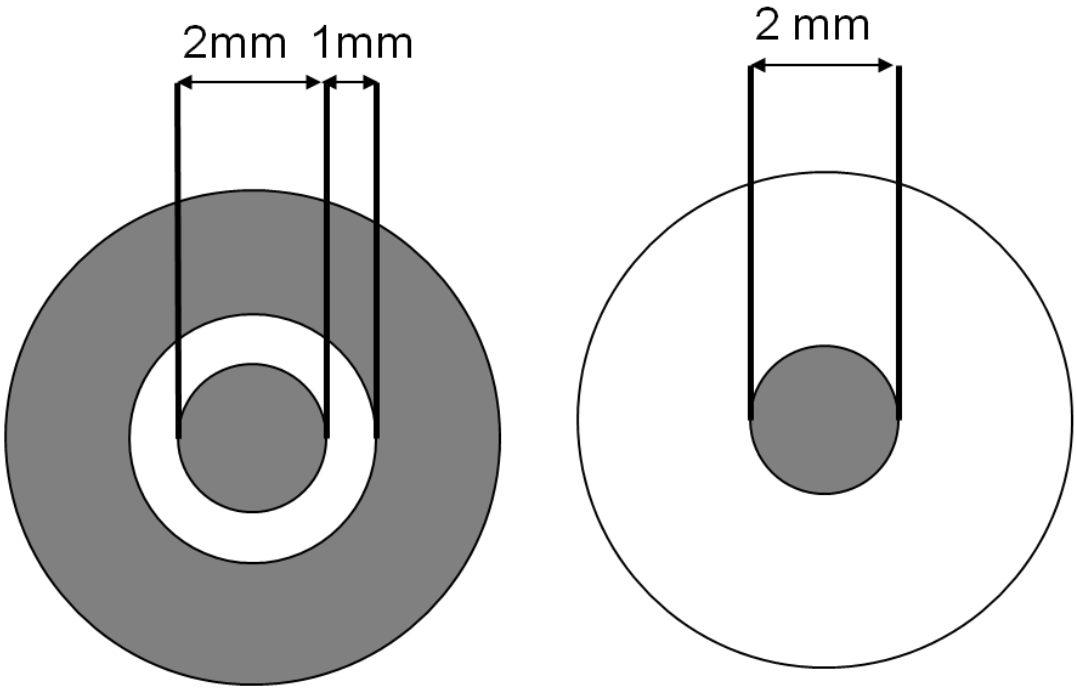

Figure 3.19 – Components used for pupil function engineering. Left - 2 mm diameter annulus, Right - 2 mm diameter centre blocked aperture. Grey regions block light, white regions allow the transmission of light

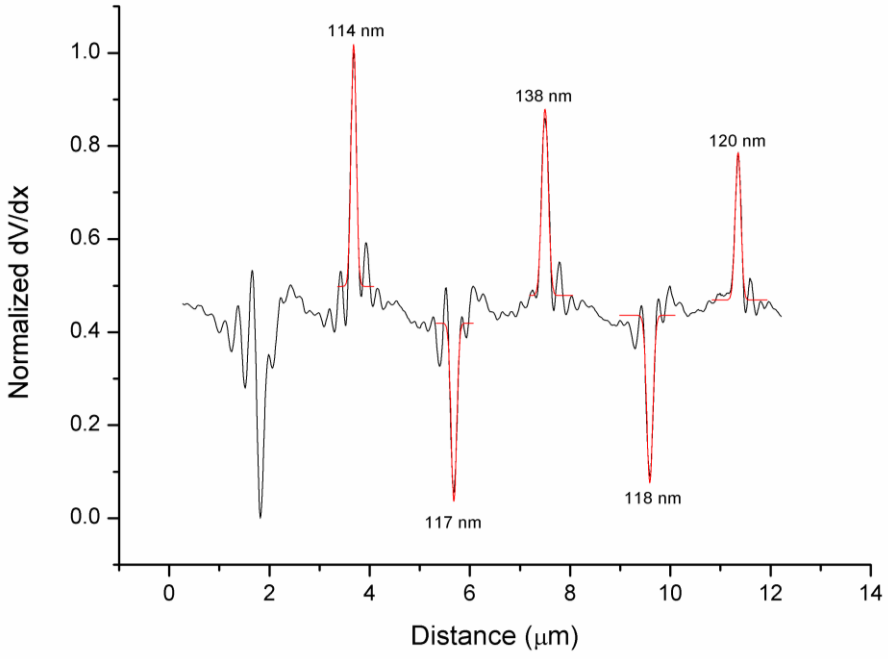

Figure 3.20 – A resolution test using a 470 nm wavelength laser, a hemispherical solid immersion lens (h-SIL), an objective lens with *NA* = 0.65, a 2 mm diameter annulus and a 4 μm period checkerboard. The red curve is the Gaussian fit. FWHM of 121 ± 10 nm was achieved.

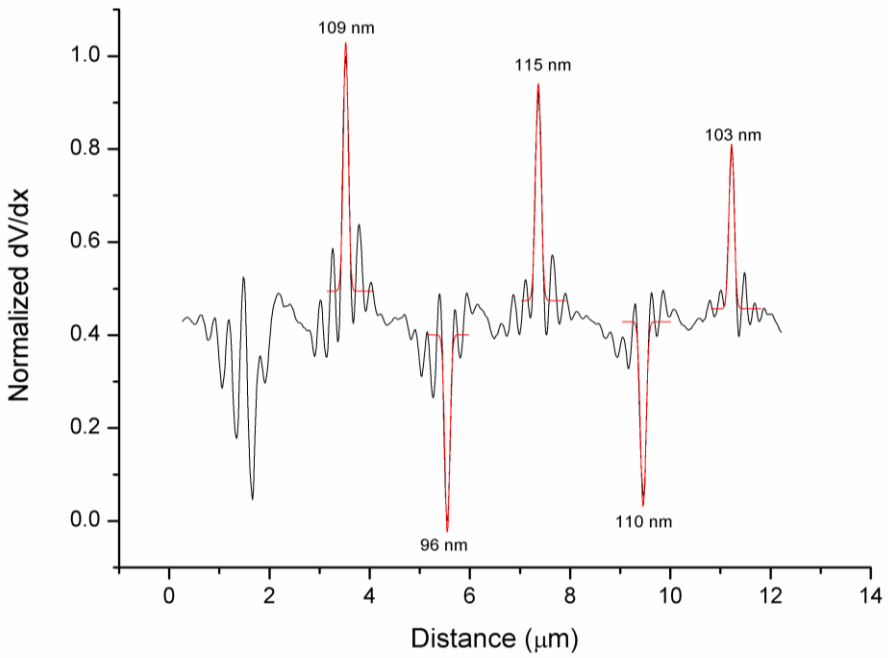

Figure 3.21 – A resolution test using a 470 nm wavelength laser, a hemispherical solid immersion lens, an objective lens with NA = 0.65, a 2 mm diameter centre blocked aperture and a 4 μm period checkerboard. The red curve is the Gaussian fit. FWHM of 107 ± 9 nm was achieved.

The measured FWHM of the centre Gaussian is 121 ± 10 nm at λ = 470 nm (see Figure 3.20), which is a reduction of ~ 30 % compared to the clear-pupil case (176 nm). The side lobes are partially visible and do not have a significant role in the spot profile as the central Gaussian part of the profile dominates the spot.

Using the centre blocked aperture produces a reduction of ~ 40 % in the FWHM spot size compared to the clear-pupil case. The FWHM spot size is 107 ± 9 nm at λ = 470 nm (see Figure 3.21) which is ~ λ/5, where λ is the wavelength of light (470 nm in this case). This is a considerable reduction in the spot size. The side lobes are more pronounced compared to when an annulus is employed (Figure 3.20) but these lobes are small and will not affect the performance of the optical system.

In conclusion it is possible to achieve an optical resolution of ~ 100 nm FWHM at λ = 470 nm using a combination of SILs and pupil-function engineering components. The pupil-function engineering components introduce significant side lobes which can affect the focal spot profile, and the implementation of these components is difficult and has not been tested at cryogenic temperatures. s-SILs have been shown not to operate

as expected at short wavelengths. In contrast h-SILs work as desired and provide the best optical resolution without the aid of pupil function engineering of 176 ± 11 nm at λ = 470 nm.

3.5 Closed-Cycle Refrigerators

The use of superconducting materials in single-photon detectors was for a long time looked upon with trepidation. The superconducting state could only be achieved using liquid helium (LiHe). LiHe systems suffer from several problems. The LiHe boils off so unless there is a helium liquefier on site the helium will need to be replaced regularly at great expense. The helium loss of LiHe limits measurement time and is impractical in a commercial product. To avoid the problems caused by using LiHe, refrigerator systems based on closed-cycle cooling have become practical and commonplace [12-14]. Two different closed-cycle refrigerator technologies, Gifford-McMahon (GM) and pulse tube coolers are explained in this section.

3.5.1 Gifford-McMahon (GM) Refrigerator

GM refrigerators were first developed in the 1950s by Gifford and McMahon [15, 16]. The coldhead of a GM refrigerator operates in the same way as a Stirling cooler. A pressure oscillation of helium gas coupled with a moving displacer provides the cooling mechanism [17]. The displacer is moved to the cold part of the system and displaces the helium gas through the regenerator to the warm part of the system (see Figure 3.22). The gas is then compressed by the piston in the compressor, and the heat of the compressed gas is removed by heat exchange with the ambient environment. The displacer is now moved away from the cold part of the system transferring the cold helium gas through the regenerator to the cold part of the system; this cold helium gas cools the system by absorbing heat. A regenerator is like a thermal capacitor. It allows two fluids (in this case both helium) of differing temperatures to flow between different sections or volumes of a system. This is achieved without a pressure drop or heat exchange between the two fluids. If this did not happen the cooling from a closed-cycle refrigerator would be very inefficient and ineffective. This process is repeated with a

frequency of 1 – 2 Hz, which cools the system down. The compressor and the coldhead are connected using high pressure gas lines and an electrical cable to drive the displacer. Modern GM refrigerators are two stage coolers with a warmer first stage (40 – 60 K) used for cooling radiation shields so they reflect and block room temperature blackbody radiation, and a colder second stage with a base temperature of 3 – 4 K.

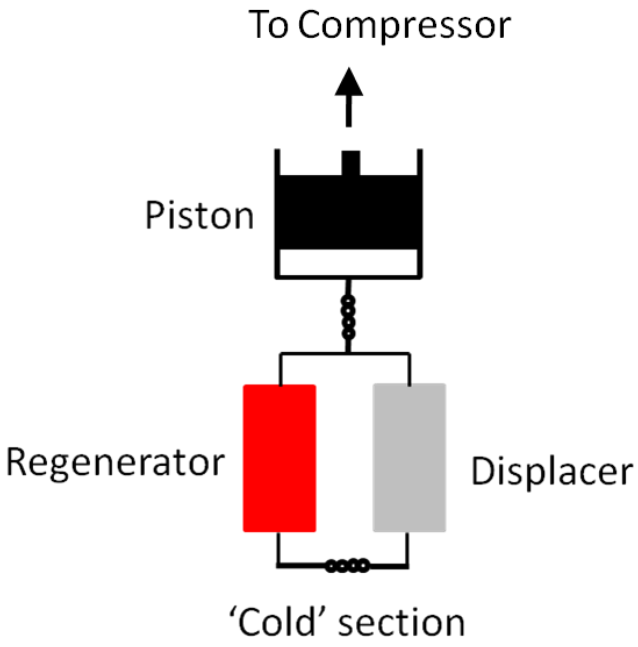

Figure 3.22 – A schematic of the Gifford-McMahon (GM) refrigerator coldhead [17]

3.5.2 Pulse Tube Refrigerator

The moving displacer in the GM refrigerator has a few drawbacks. The displacer has a limited lifetime, it is a source of vibrations, and provides contributions to axial heat conduction and shuttle heat loss. To solve these problems a closed-cycle refrigerator without the displacer was developed. This cooler, known as a pulse tube refrigerator, was invented in the 1960s by Gifford and Longsworth [18]. Further improvements by Mikulin *et al* [19] and Radebaugh *et al* [20] have led to the state-of-the-art pulse tube refrigerators available today (see Figure 3.23).

The piston compresses the helium gas in the pulse tube, and since there is an increase in the gas pressure in the pulse tube, the warm gas flows to the reservoir through the

orifice. The helium gas flow stops when the pressures in the pulse tube and the reservoir are equal. The warm helium gas loses its heat by way of heat exchange with the ambient environment. The piston now decompresses and adiabatically expands the helium gas in the pulse tube. The cold helium gas flows from the reservoir through the orifice and into the pulse tube, where is absorbs heat from the system. This process is repeated to achieve cooling.

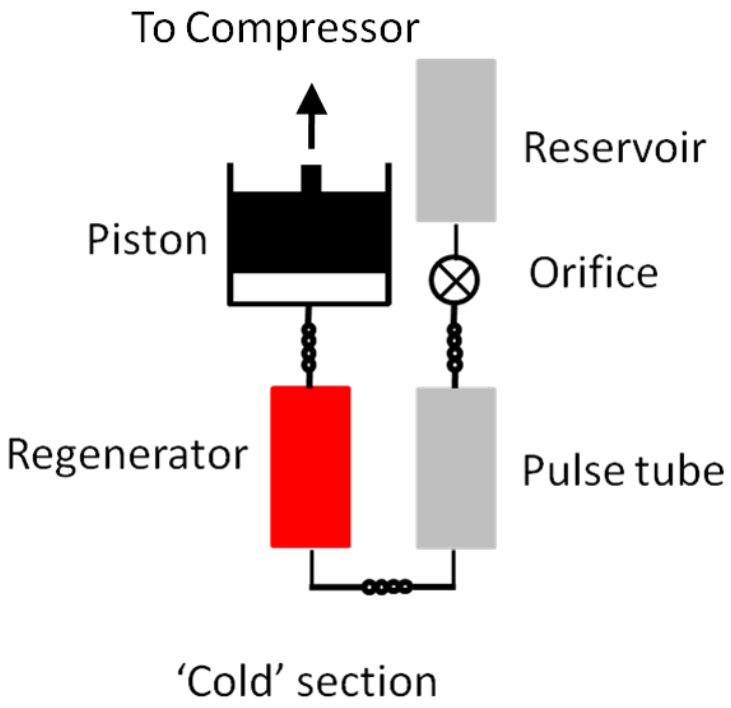

Figure 3.23 – A schematic of the pulse tube (PT) refrigerator coldhead [17]

3.6 Miniature Confocal Microscope Configuration

The confocal microscope configuration detailed in section 3.4 would require significant alteration for telecommunication wavelength SNSPD characterization measurements. These alterations would include the complete change of optics in the microscope head and the collimating and objective lenses. Another major alteration would be to change the alignment camera from a silicon CCD to one which is sensitive to telecommunications wavelengths. A further problem is the time constraints limiting measurement time and a higher than desired sample temperature (4 - 5K compared to 3K) when using a confocal microscope configuration inserted in a dewar of liquid

helium, causing an elevated dark count rate due to blackbody radiation. In order to solve these problems it was determined that integrating a miniaturized version of the microscope in a closed-cycle refrigerator would be beneficial. A miniaturized fibre based confocal microscope has been presented by Högele *et al* [21]. This NIR miniature confocal microscope operated at cryogenic temperatures which were achieved using liquid helium.

A miniature confocal microscope was designed for telecommunications wavelength operation in a GM closed-cycle refrigerator. The miniature microscope was designed around the piezoelectric motors and scanner detailed in section 3.4.2. One major difference between the microscope detailed in section 3.4 and the miniaturized design is the utilization of a fixed sample and moveable optics. A fixed sample was chosen to make changing samples easier and less time consuming.

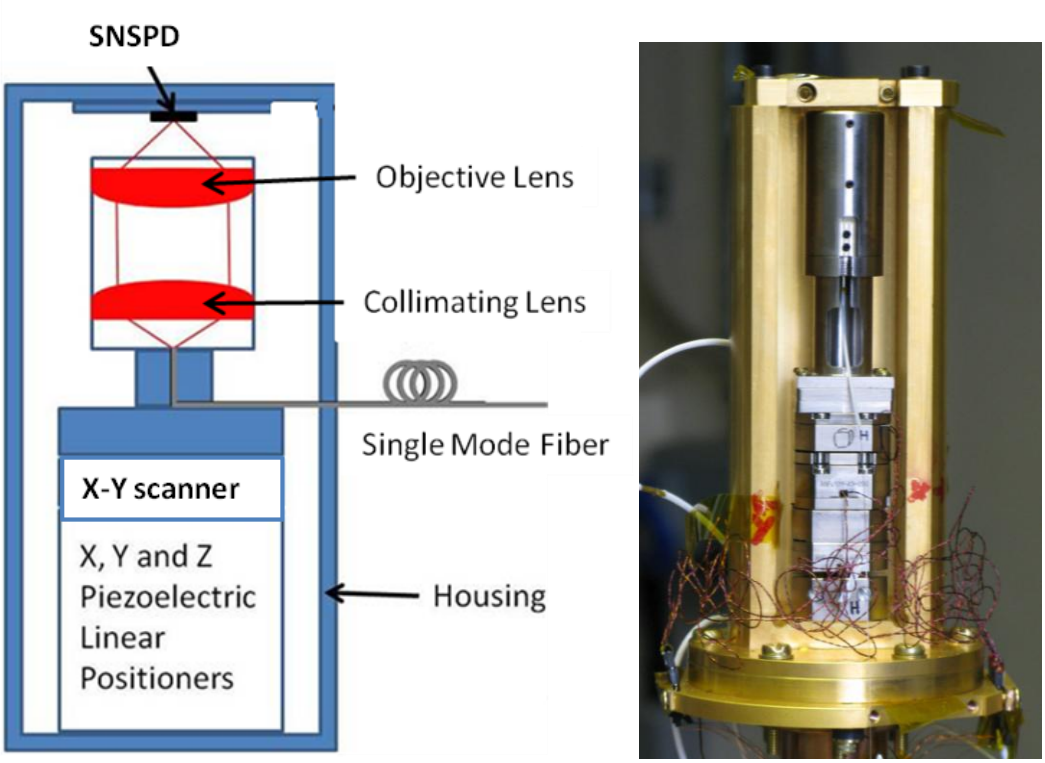

Figure 3.24 – Miniature confocal microscopy configuration setup, left - schematic, right – photograph while mounted to a Gifford-McMahon coldhead.

3.6.1 Optics Choices and Alignment

To achieve comparable resolution to that predicted by the Sparrow Criterion at telecommunications wavelength compared to visible wavelengths, the aspheric lenses were again used but with differing anti-reflection coatings.

Optical alignment and collimation of the beam emerging from the end of the optical fibre are achieved differently compared to the previous set-up (section 3.4). Instead of using a Z-axis translation stage, the collimating lens is mounted in an optics holder tube using a grub screw and the fibre ferrule is manually aligned to the correct distance for collimation. Once the ferrule containing the optical fibre is in the desired position, it is secured using two grub screws; this is a robust and secure method for collimation. The objective lens is then fixed to the end of the optics holder tube again using a grub screw. The optics are fastened to the motor and scanner stack using a connector piece.

Using commercially available optics, a collimating lens (Thorlabs™ 352280-C) with NA = 0.15, clear aperture of 3.6 mm and a focal length of 18.4 mm was chosen. A high NA objective lens will provide the highest possible resolution but in addition for efficient coupling the clear apertures must be closely matched. As a compromise the objective lens (Thorlabs™ 352330-C) had a clear aperture of 5.5 mm, a focal length of 3.1 mm but NA = 0.68. Both lenses have appropriate anti-reflection coatings (-C type) minimising reflections over the wavelength range 1050 – 1620 nm.

Due to the lack of free-space optics, alignment and focusing of the optics cannot be performed with a CCD camera. Reflected light from the device under test is coupled back into the optical fibre. An optical circulator is used to collect this reflected light onto a power meter. As illustrated in Figure 3.12 the system can be focused, and by monitoring variations in reflective surfaces, either manually or by taking a computer controlled reflection map (see Figure 3.25), precise positioning of the focused spot can be achieved.

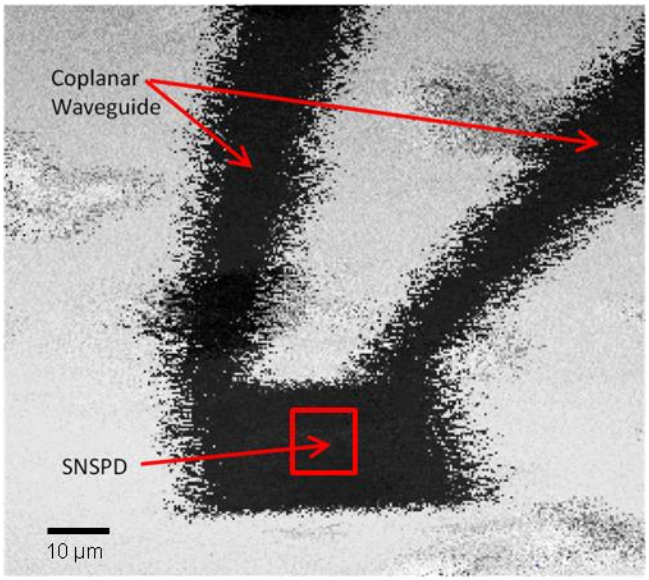

Figure 3.25 – A reflection map showing SNSPD active area (red square) and the coplanar waveguide. The focal spot from the miniature confocal microscope configuration is raster scanned using the X and Y piezoelectric linear positioners. A map is acquired by reading the reflected signal.

3.6.2 Resolution Tests

As shown and detailed in section 3.4.3, resolution tests are used to determine the optical performance of the system. Due to the integration of the miniature confocal microscope configuration into a GM closed-cycle refrigerator, optical performance with and without the coldhead operating were determined. Optical resolution with the coldhead under operation is made worse due to the introduction of vibrations from the coldhead, causing a widening of the focal spot.

As the miniature confocal microscope configuration is fibre based the resolution tests need to be carried out at both room temperature and at ~ 3 K, operating in transmission mode is difficult. Due to these factors, resolution tests were carried out in reflection mode. The measurements work the same way, the only difference is that the light reflected from the checkerboard is coupled back into the optical fibre, and this light is directed onto an InGaAs photodiode, rather than a Si photodiode.

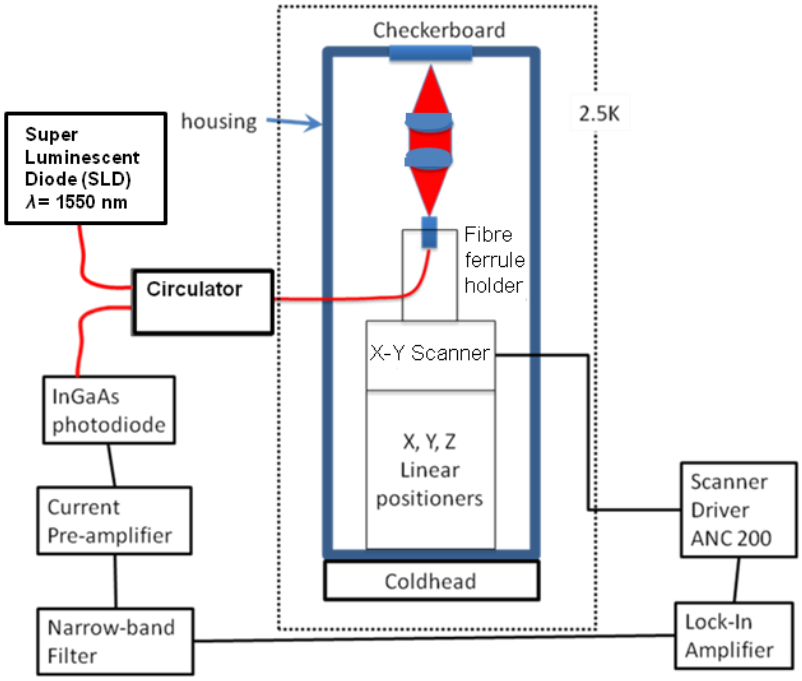

Figure 3.26 – The setup for performing resolution tests in reflection mode on the miniature confocal microscope configuration at λ = 1550 nm.

In Figure 3.26, some other differences should be noted; a super luminescent diode (SLD) of wavelength 1550 nm was used rather than a CW laser source (Fabry-Perot laser source). This is because the vibrations from the coldhead produce a small path difference in the reflected signal, this was causing interference so a SLD was used as it has a short coherence length (8 µm) compared to the CW laser source (~ 10s of meters). A fibre based optical circulator was selected rather than a beamsplitter as reflections back into the SLD were causing fluctuations in the output power. The circulator removed this effect. The narrowband filter (110 – 150 Hz) was used as there was electrical noise on the signal caused by grounding problems; this noise had an amplitude comparable to the signal level so the lock-in amplifier was unable to recover the signal.

The situation with the coldhead switched off yielded a FWHM resolution of 1094 ± 127 nm at λ = 1550 nm using an objective lens with NA = 0.68 (see Figure 3.27) from the fitted Gaussians. This agrees within experimental error with the predicted value of 1185 nm from the Sparrow criterion.

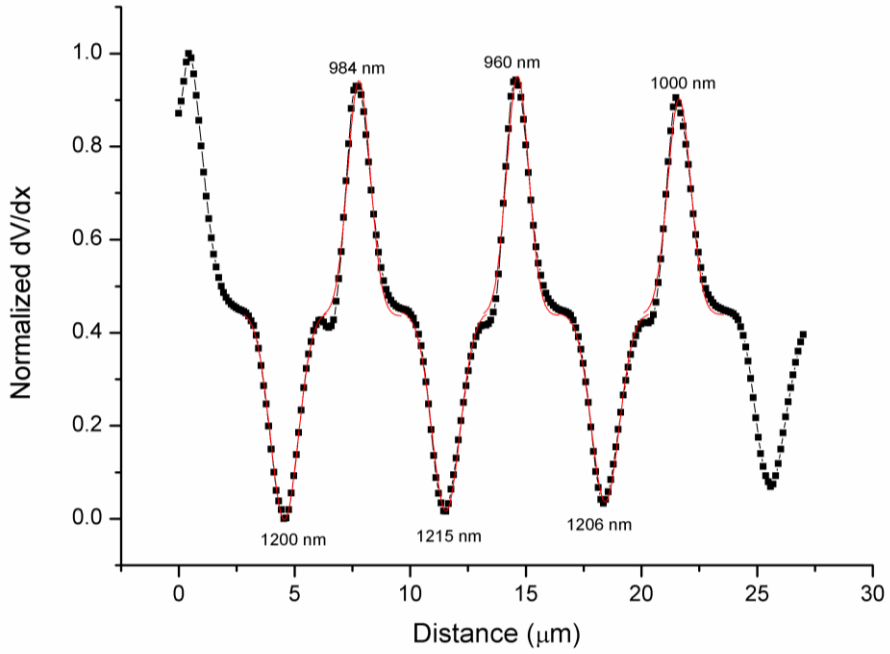

Figure 3.27 – Resolution test data in the miniature confocal microscope configuration at a wavelength of 1550 nm and an objective lens with *NA* = 0.68 with no vibrations from the coldhead and using a 4 μm period checkerboard. The red curve is the Gaussian fit. A FWHM resolution of 1094 ± 127 nm was obtained.

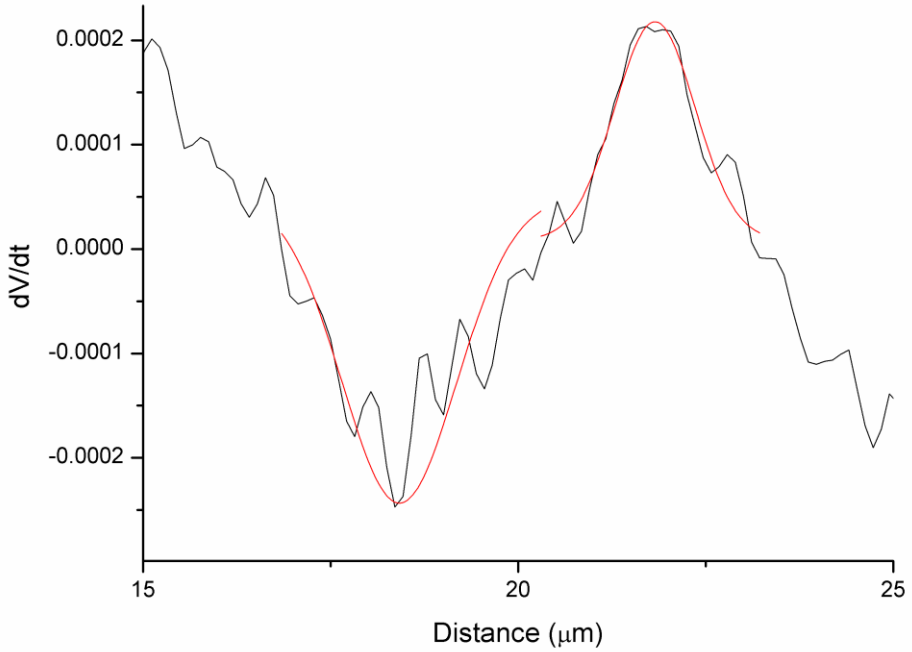

Figure 3.28 – Resolution test data in miniature confocal microscope configuration at a wavelength of 1550 nm and an objective lens with *NA* = 0.68 with vibrations from the coldhead and using a 4 μm period checkerboard. The red curves are the Gaussian fits. A FWHM resolution of 1305 ± 363 nm was obtained.

The vibrations from the coldhead caused a broadening of the FWHM spot to 1305 ± 363 nm at λ = 1550 nm using an objective lens with NA = 0.68 (see Figure 3.28). This is an increase of ~ 200 nm which is a ~ 20 % increase in spot size. The edge profile contains noise which made getting an accurate fit more difficult. This value of ~ 1300 nm FWHM spot size is larger than predicted but is smaller than SNSPD device areas (10 µm x 10 µm and 20 µm x 20 µm [4, 22]), and provides the ability to study localized areas of SNSPDs.

3.7 Low Temperature Electrical and Optical Characterization

The performance of SNSPDs is characterized using both electrical and optical measurements. These measurements give information on the critical current I_c, inductance L, degree of constriction C and the detection efficiency of SNSPDs and provide a pathway to improving SNSPD performance. In the following sections the method and theory behind each characterization measurement is explained.

3.7.1 Current – Voltage (I-V) Characteristic Measurements*

Current-voltage (I-V) characteristic measurements carried out on SNSPDs give an indication of the overall performance expected. An I-V measurement simply measures the voltage across the SNSPD as the applied bias current is varied (see Figure 3.29). The bias current is swept from zero to a maximum value which is greater than the critical current and then it is swept to the equivalent negative maximum value and then back to zero. Figure 3.30 shows a standard I-V curve for both an unshunted and shunted SNSPD. A shunt is a resistor which has a resistance significantly lower than the resistance of the SNSPD in the non-superconducting or resistive state. Typically a 50 Ω shunt is used. The shunt is placed in parallel to the SNSPD (connected on the outside of the closed-cycle refrigerator). The purpose of a 50 Ω shunt is to divert the applied current bias away from the SNSPD when it is resistive allowing it to recover into the superconducting state.

* This measurement setup was constructed by Chandra Mouli Natarajan

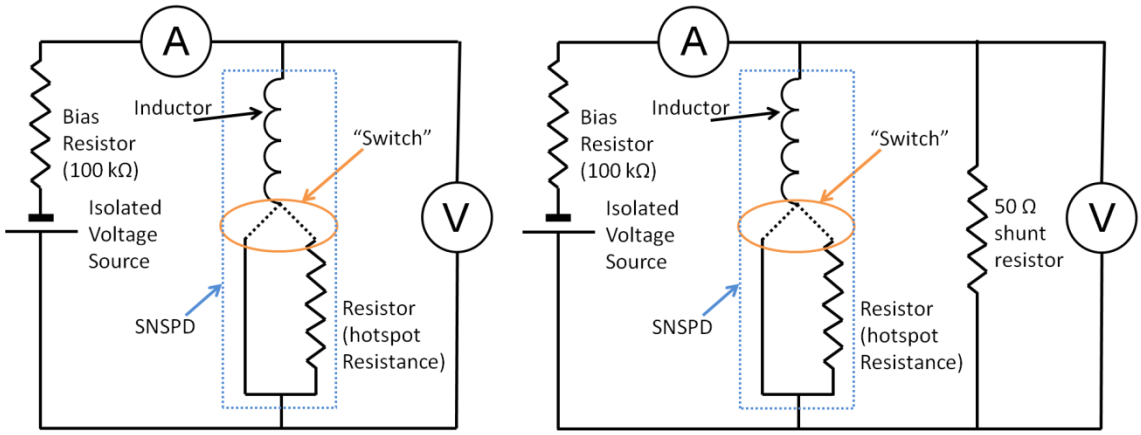

Figure 3.29 – The electrical circuit for the current-voltage (I-V) characteristic measurement on a SNSPD.

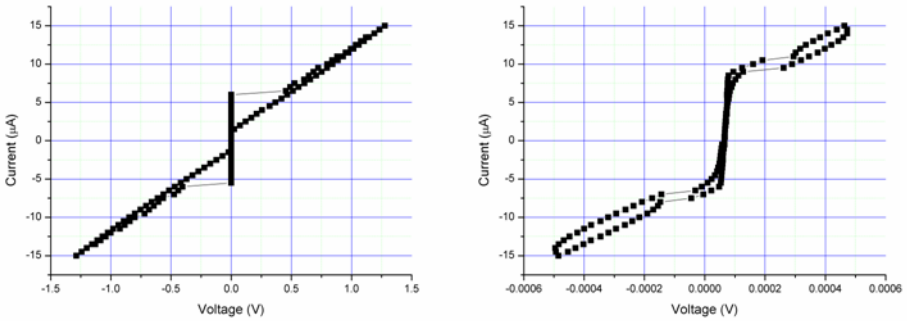

Figure 3.30 – SNSPD I-V characteristics, Left - No shunt. Right – With 50 Ω shunt.

The most useful information gained from the I-V curve is the critical current I_c, which gives the maximum current that can be supported by the SNSPD before it switches to the resistive state and is the point where the voltage across the SNSPD increases from zero. A larger I_c allows for greater current biasing and thus increased performance. Amongst devices of fixed cross-section, the device with greatest I_c will also support the highest current density J_c and be most sensitive to single photons. The hysteresis observed in the unshunted case is because when the bias current is swept from the maximum value to zero, the current in the SNSPD needs to drop below I_c before it recovers into the superconducting state. This hysteresis is not observed when using a shunt resistor.

3.7.2 Kinetic Inductance[+]

Kinetic inductance L is a measure of the inertial mass of mobile charge carriers (Cooper pairs) in the superconductor. The measured value will change with a varying bias current as the inertia of the charged carriers opposes a change in bias current. By measuring L for a range of current biases from zero up to I_c (calibrated by a resistive state measurement) a range of L against I values can be plotted. L is measured using a vector network analyzer (AEA Via Bravo 6014-5000) which measures the amplitude and phase of the reflected signal over a range of specified frequencies (100 kHz to 60 MHz). The inductance of the wires that connect the network analyzer to the SNSPD have a noticeable inductance which affects the measurement; this is why one measurement in the resistive state is taken. Subtracting this curve from the curves in the superconducting state removes the L of the wires from the curve to leave only the L_k of the SNSPD. The frequency versus phase graph for each current bias point shows an exponential decay and L is found by fitting to the curve.

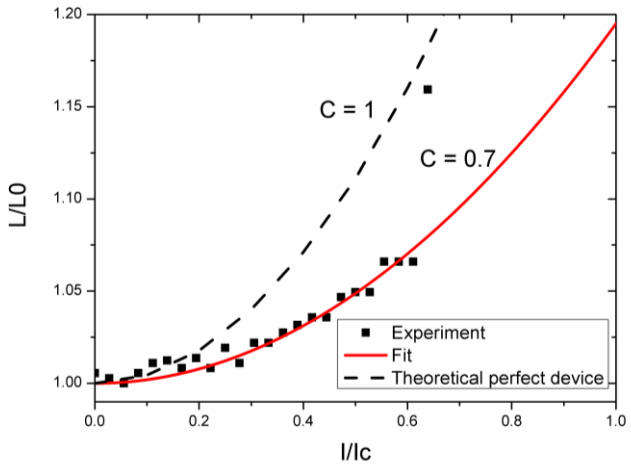

Figure 3.31 – The upturn in normalised kinetic inductance (L/L_0) with normalised bias current of (I/I_C) theoretically uniform SNSPD (black dashes) and a practical SNSPD with C = 0.7 (black squares and red line (fit)). L_0 = kinetic inductance at I = 0; I_c is the critical current.

With the L values obtained from the fits, plotting I/I_c versus L/L_0 (see Figure 3.31), where L_0 is the kinetic inductance at zero bias current, the curve can be fitted to the theoretical equation 3.1.

$$\frac{L}{L_{(0)}} = 1 + \left(\frac{4}{9}\right) C^2 \left(\frac{I_C}{I}\right)^2 \quad . \tag{3.1}$$

[+] This measurement setup was constructed by Dr Michael Tanner and Christopher Coward

From this equation, the constriction factor *C* is the only free fitting parameter and gives the extent of constrictions compared to the uniform case, with *C* values varying from 0 to 1. The *C* value gives an indication to how well the SNSPD will detect photons and is (along with I-V measurements) a rapid way to screen many devices in order to determine which hold the most promise for optical coupling.

3.7.3 Detection Efficiency

Detection efficiency (*DE*) measurements at one specific dark count rate (DCR) will be described in section 3.8.1. A more rigorous method of performing *DE* measurements is to measure the count rate for a specific DCR at varying photon fluxes and fitting the data [23]. Using a pulsed laser source and calibrated programmable optical attenuators, the setup shown in Figure 3.32 is used to measure the detected count rate at varying DCRs. The DCR is controlled by changing the current biasing of the SNSPD using the programmable battery powered voltage source.

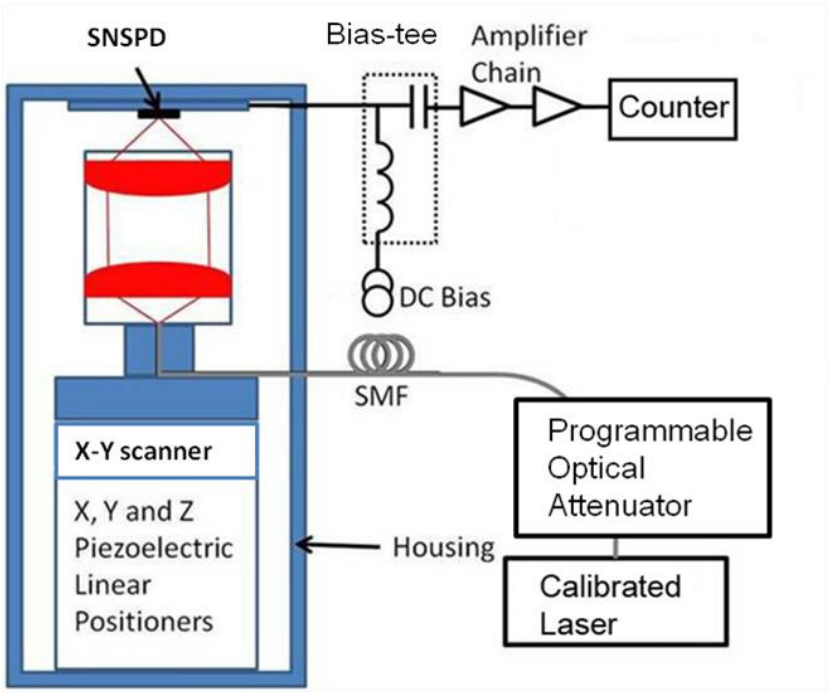

Figure 3.32 – Measurement setup for determining the detection efficiency of a SNSPD mounted in the miniature confocal microscope configuration.

A family of curves (with count rate measured as a function of photon flux) corresponding to different current bias points (and DCRs) is shown in Figure 3.33. By fitting to these curves, the *DE* of the detector is found. This shows that with higher current bias (approaching I_c) a higher *DE* is observed but also so is an increased DCR (see Figure 3.33 bottom).

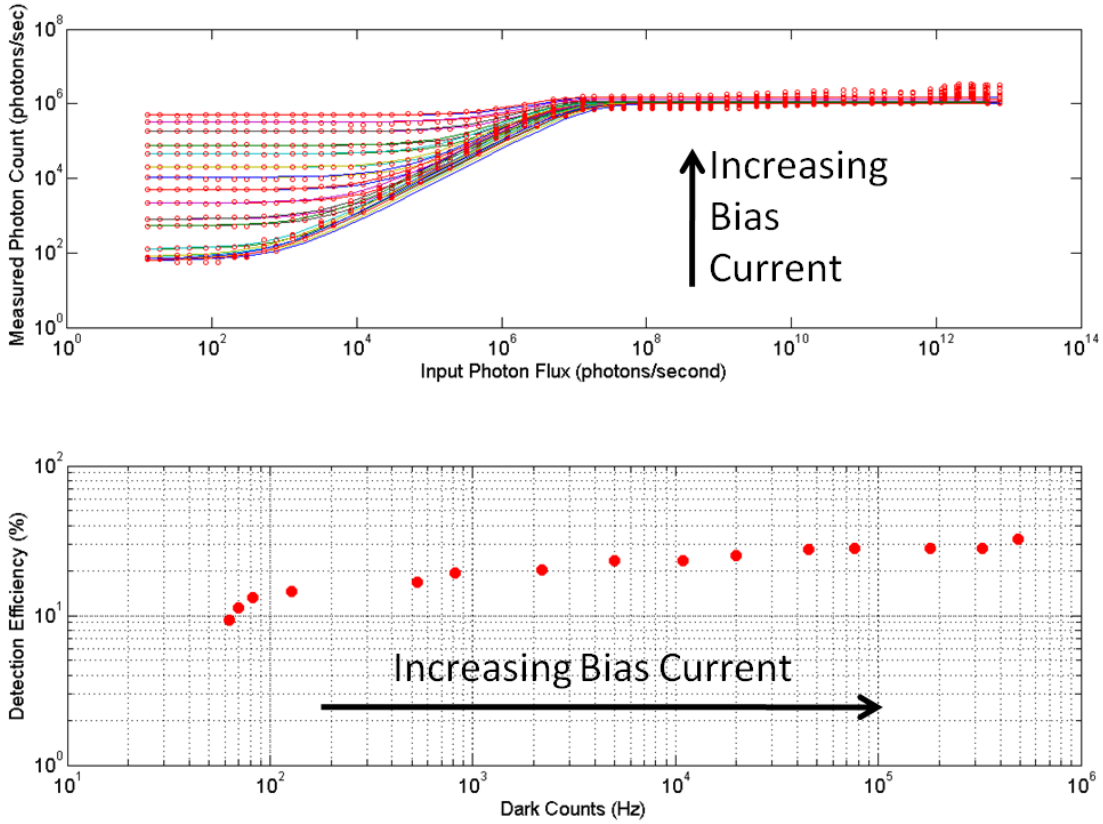

Figure 3.33 – The detection efficiency (*DE*) of an SNSPD measured with a 1 MHz gain switched laser diode at 1550 nm wavelength. Top - Raw data when varying input photon flux and increasing bias current. Bottom - Dark count rate (DCR) versus *DE*.

For a comprehensive picture of device performance, *DE* measurements should be performed at all desired wavelengths.

3.8 Scanning Measurements

Using both the LiHe and the miniature confocal microscope configurations, scanning measurements of device properties can be performed. Nano-optical scanning measurements provide localized information of the SNSPD, including detection

efficiency, jitter and pulse timing delay. For this to work the focal spot is raster scanned across the device active area and the desired data is measured and recorded. From the data three-dimensional (3D) maps can be produced to clearly show the variation in performance across the whole device area. By using the X-Y scanner, the scan step size can be significantly smaller than the focal spot size, and is reliably reproducible unlike using the slip-stick piezoelectric linear positioners which can be hysteretic giving an unreliable step size repeat.

3.8.1 Detection Efficiency Mapping

Detection efficiency (*DE*) mapping, (sometimes called photoresponse mapping) provides localized *DE* across an SNSPD. *DE* is defined as the ratio of the number of detected photons to the number of incident photons:

$$DE(\%) = \frac{No\ of\ \ Detected\ \ Photons}{No\ of\ \ Incident\ \ Photons} \times 100 \quad . \tag{3.2}$$

The SNSPD is current-biased to give a chosen dark count rate (DCR) and a calibrated laser source is used to illuminate the SNSPD. At each point the number of counts per second is recorded, which can be plotted to give the general trends on detection efficiency across the device. It is more useful to convert the count rate at each point to *DE*. To convert count rate to *DE*, the photon flux (the number of incident photons) is required and can be easily calculated from the incident power and wavelength of the calibrated laser source using equation 3.3:

$$Photon\ \ Flux = \frac{Incident\ \ Power}{Energy\ of\ \ Photon} \quad . \tag{3.3}$$

Since there is a known DCR in this measurement, the equation for *DE* is modified to include the DCR:

$$DE(\%) = \frac{No\ of\ \ Detected\ \ Photons - DCR}{No\ of\ \ Incident\ \ Photons} \times 100 \quad . \tag{3.4}$$

This method provides an insight to the uniformity of the SNSPD, and can optically detect the presence of constrictions which were discussed in section 0. Figure 3.34 [24] shows two photoresponse maps, (a) is the map of a uniform SNSPD with little variation across the device area and (b) is the map of an SNSPD with a significant constriction which dominates the rest of the device giving photoresponse only at one position.

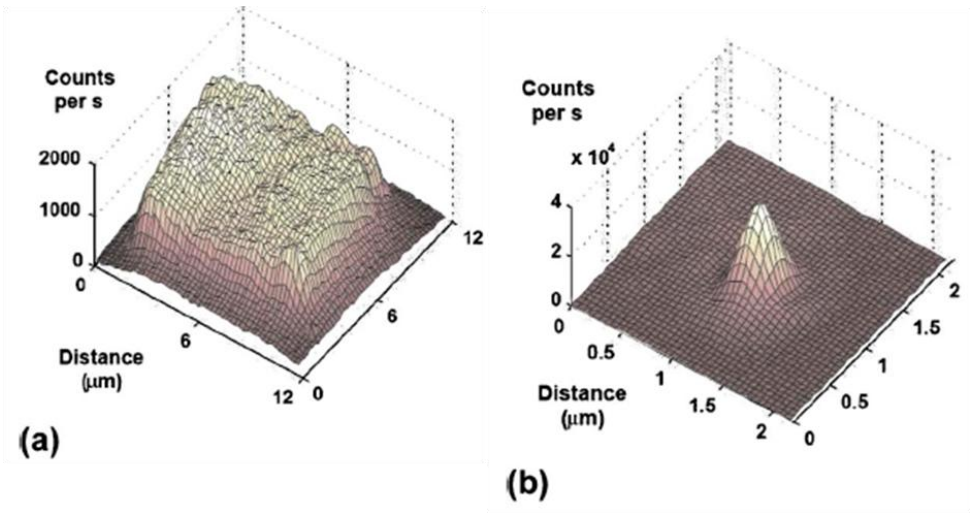

Figure 3.34 – Detection efficiency maps at λ = 470 nm. (a) - Uniform photoresponse from SNSPD, (b) - Non-uniform photoresponse from SNSPD, caused by a constriction [24].

3.8.2 Mapping of Timing Properties

Just like *DE* maps, jitter and output pulse timing delay maps can be measured using a confocal microscope configuration (see Figure 3.35). A jitter map requires a jitter measurement to be taken at each position. Timing jitter (Δt) is the uncertainty or variation between the absorption of a photon and the generation of an output electrical signal. A jitter measurement is carried out using a detector under test and either a 'clock' detector or an electrical clock pulse which is synchronized to the output pulses of the laser and has a constant count rate. Either a fast oscilloscope or a time correlated single-photon counting (TCSPC) card is required for accurate timing measurements.

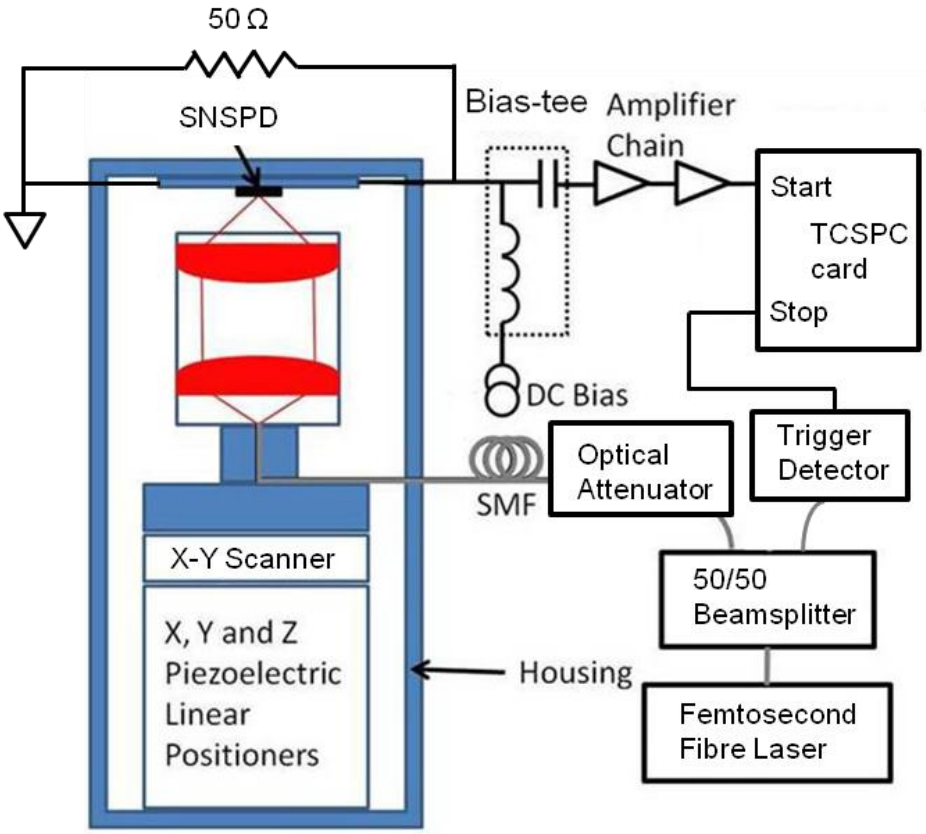

Figure 3.35 – The setup for the mapping of localised SNSPD device properties (*DE, Δt and τ*). Femtosecond fibre laser (50 MHz repetition rate, 2 mW output power), Trigger detector – either an InGaAs fast photodiode (timing jitter 17 ps FWHM) or a fibre-coupled SNSPD (timing jitter 140 ps at FWHM), TCSPC – time correlated single photon counting electronics (PicoQuant PicoHarp); SNSPD – superconducting single photon detector which is under test.

The TCSPC method records the timing interval between two signals ('start' and 'stop') and produces a histogram of the data. It is more common to run the measurement in reverse start-stop mode, which has the signal from the detector under test as the 'start' and the 'clock' detector signal as the stop. This is done because under start-stop mode, the timing electronics starts recording the time between the two signals and sometimes there is no 'stop' signal. This is not a problem for low repetition rate lasers, as the timing electronics will reset the measurement after a specified time. For lasers with higher repetition rates (10s of MHz), this can produce false readings as the measured 'stop' could be in a different clock cycle. Reverse start-stop mode only starts measuring when there is a signal from the detector under test and the 'clock' detector count rate is constant so will provide a 'stop' each time. A histogram is built up giving the instrumental response of the detector, and the fitted FWHM provides the jitter value. The overall jitter value is the convolution (∗) of all sources of jitter in the system

(equation (3.5)), including the laser, the timing electronics and the jitter of the 'clock' detector alongside the jitter of the detector under test.

$$\Delta t_{Total} = \Delta t_{SNSPD} * \Delta t_{Laser} * \Delta t_{TCSPC} \quad . \tag{3.5}$$

In equation 3.5 Δt_{Total} is the overall instrumental response of the system, Δt_{SNSPD} is the instrumental response of the SNSPD, Δt_{Laser} is the instrumental response of the laser and Δt_{TCSPC} is the instrumental response of the TCSPC electronics. When all of the jitter contributions are Gaussian the total timing jitter can be calculated as the sum of the square of all the components:

$$|\Delta t_{Total}|^2 = |\Delta t_{SNSPD}|^2 + |\Delta t_{Laser}|^2 + |\Delta t_{TCSPC}|^2 \tag{3.6}$$

The use of a femtosecond pulse laser and a good quality TCSPC card allows these contributions to be excluded as they are usually very small. For SNSPDs the response shape is Gaussian. This means that having two SNSPDs as the 'start' and 'stop' for the TCSPC card gives an overall Gaussian response.

The jitter maps can relate to differing properties across the SNSPD and provide insights to the understanding of the origin of timing jitter and how the devices actually work.

Output pulse timing delay (τ), or more precisely relative pulse timing delay is the timing delay in pulse peak arrival time in relation to a reference time. The timing delay is measured from the position in time where the peak of the histogram occurs. The pulse timing delay is determined from the histogram from the TCSPC electronics. The timing delay has been observed to be between 0 – 50 ps across a non-uniform SNSPD [25].

Variations in τ shows that differing parts of an SNSPD trigger an output pulse sooner than other parts in a non-uniform device. This difference in output pulse triggering is believed to be caused by differing hotspot resistances. Using SPICE (Simulated Program with Integrated Circuit Emphasis) [26, 27] modelling this can be simulated and investigated. Further detailed explanation is included in section 5.3.3.

3.9 Conclusion

This chapter gives a comprehensive overview of the experimental techniques used in this thesis. The multistep fabrication of bare SNSPD device chips, (provided by NICT, Japan) has been detailed. The in-house preparation and electrical contacting of the bare SNSPD chips using ultrasonic wedge wire-bonding has been described. Two different confocal microscope configurations, one using liquid helium and the other a miniaturized version which is integrated inside a closed-cycle cooler have been detailed. The design of the miniaturized confocal microscope configuration was described in detail along with the optical choices for both setups. The advantages and disadvantages of both methods were also described. The operating principle and the major advantages gained by using the stack of linear positioners and the X-Y scanner were discussed in detail. The optical performance achievable using both configurations were presented with the aid of resolution tests.

Detail of scanning measurements for detection efficiency, jitter and pulse timing delay mapping experiments were presented. The use of time correlated single photon counting (TCSPC) electronics in these measurements was discussed. Electrical and optical characterization measurements used for both rapid screening of large numbers of devices along with detection efficiency measurements to provide detailed performance characteristics were also discussed.

The techniques detailed in this chapter have enabled me to carry out the detailed low temperature nano-optical studies of SNSPD device performance presented in Chapters 4 and 5 of this thesis.

3.10 Chapter 3 References

1. *Powder Diffraction File, Joint Committee on Powder Diffraction Standards, Philadelphia, PA, 1967, Card 38-1155 for NaCl-structured NbN.*
2. *http://www.mt-berlin.com/frames_cryst/descriptions/substrates.htm (Date Accessed 26th January 2011).*
3. S. Miki, M. Fujiwara, M. Sasaki, and Z. Wang, *NbN superconducting single-photon detectors prepared on single-crystal MgO substrates.* IEEE Transactions on Applied Superconductivity, 2007. **17**(2): p. 285-288.
4. S. Miki, M. Fujiwara, M. Sasaki, B. Baek, A.J. Miller, R.H. Hadfield, S.W. Nam, and Z. Wang, *Large sensitive-area NbN nanowire superconducting single-photon detectors fabricated on single-crystal MgO substrates.* Applied Physics Letters, 2008. **92**(6): p. 061116.
5. *SMF-28e optical fiber, www.corning.com.*
6. *Attocube 100 series xy scanner http://www.attocube.com/nanoPOSITIONING/ANSxy100/Specifications_ANSxy100.pdf (Date Accessed 9th February 2011).*
7. K. A. Serrels, E. Ramsay, and D.T. Reid, *70 nm resolution in subsurface optical imaging of silicon integrated-circuits using pupil-function engineering.* Applied Physics Letters, 2009. **94**(7): p. 073113.
8. C. M. Sparrow, *On spectroscopic resolving power.* The Astrophysical Journal, 1916. **44**: p. 76.
9. B. Richards and E. Wolf, *Electromagnetic Diffraction in Optical Systems. II. Structure of the Image Field in an Aplanatic System.* Proceedings of the Royal Society of London. Series A. Mathematical and Physical Sciences, 1959. **253**(1274): p. 358-379.
10. K. A. Serrels, E. Ramsay, P.A. Dalgarno, B.D. Gerardot, J.A. O'Connor, R.H. Hadfield, R.J. Warburton, and D.T. Reid, *Solid immersion lens applications for nanophotonic devices.* Journal of Nanophotonics, 2008. **2**: p. 021854.
11. E. J. Botcherby, R. Juskaitis, and T. Wilson, *Scanning two photon fluorescence microscopy with extended depth of field.* Optics Communications, 2006. **268**(2): p. 253-260.

12. R. H. Hadfield, M.J. Stevens, S.S. Gruber, A.J. Miller, R.E. Schwall, R.P. Mirin, and S.W. Nam, *Single photon source characterization with a superconducting single photon detector.* Optics Express, 2005. **13**(26): p. 10846-10853.
13. S. Miki, M. Fujiwara, M. Sasaki, and Z. Wang, *Development of SNSPD System With Gifford-McMahon Cryocooler.* IEEE Transactions on Applied Superconductivity, 2009. **19**(3): p. 332-335.
14. X. L. Hu, T. Zhong, J.E. White, E.A. Dauler, F. Najafi, C.H. Herder, F.N.C. Wong, and K.K. Berggren, *Fiber-coupled nanowire photon counter at 1550 nm with 24% system detection efficiency.* Optics Letters, 2009. **34**(23): p. 3607-3609.
15. W. E. Gifford and H.O. McMahon, *A new refrigeration process.* 10th Int. Congr. Refrigeration, Copenhagen, Denmark, 1959.
16. H. O. McMahon and W.E. Gifford, *A new low-temperature gas expansion cycle.* Advanced Cryogenic Engineering., 1960. **5**(354–372).
17. R. Radebaugh, *Refrigeration for superconductors.* Proceedings of the IEEE, 2004. **92**(10): p. 1719-1734.
18. W. E. Gifford and R.C. Longsworth, *Pulse tube refrigeration.* Journal of Engineering for Industry-Transactions of the ASME, 1964. **86**: p. 247–258.
19. E. I. Mikulin, A.A. Tarasov, and M.P. Shkrebyonock, *Low temperature expansion pulse tubes.* Advanced Cryogenic Engineering, 1984. **29**: p. 629–637.
20. R. Radebaugh, J. Zimmerman, D.R. Smith, and B. Louie, *A comparison of three types of pulse tube refrigerators: New methods for reaching 60 K.* Advanced Cryogenic Engineering, 1986. **31**: p. 779–789.
21. A. Hogele, S. Seidl, M. Kroner, K. Karrai, C. Schulhauser, O. Sqalli, J. Scrimgeour, and R.J. Warburton, *Fiber-based confocal microscope for cryogenic spectroscopy.* Review of Scientific Instruments, 2008. **79**(2): p. 023709.
22. A. Verevkin, J. Zhang, R. Sobolewski, A. Lipatov, O. Okunev, G. Chulkova, A. Korneev, K. Smirnov, G.N. Gol'tsman, and A. Semenov, *Detection efficiency of large-active-area NbN single-photon superconducting detectors in the ultraviolet to near-infrared range.* Applied Physics Letters, 2002. **80**(25): p. 4687-4689.
23. R. H. Hadfield, *Single-photon detectors for optical quantum information applications.* Nature Photonics, 2009. **3**(12): p. 696-705.

24. R. H. Hadfield, P.A. Dalgarno, J.A. O'Connor, E. Ramsay, R.J. Warburton, E.J. Gansen, B. Baek, M.J. Stevens, R.P. Mirin, and S.W. Nam, *Submicrometer photoresponse mapping of nanowire superconducting single-photon detectors.* Applied Physics Letters, 2007. **91**(24): p. 241108.
25. J. A. O'Connor, M.G. Tanner, C.M. Natarajan, G.S. Buller, R.J. Warburton, S. Miki, Z. Wang, S.W. Nam, and R.H. Hadfield, *Spatial dependence of output pulse delay in a niobium nitride nanowire superconducting single-photon detector.* Applied Physics Letters, 2011. **98**(20): p. 201116-3.
26. L. Nagel and R. Rohrer, *Computer analysis of nonlinear circuits, excluding radiation (CANCER).* IEEE Journal of Solid-State Circuits, 1971. **6**(4): p. 166-182.
27. L. W. Nagel and D.O. Pederson, *SPICE (Simulation Program with Integrated Circuit Emphasis), Memorandum No. ERL-M382.* University of California, Berkeley, 1973.

Chapter 4 Liquid Helium Confocal Microscope Configuration Measurements on SNSPDs at λ = 470 nm and λ = 950 nm

4.1 Introduction

Microscopy techniques are essential in many different applications at the forefront of science and technology, including spectroscopy of semiconductor quantum dots [1-4] and single molecules [5, 6]. These techniques use diffraction-limited focal spot sizes which are sub - µm in size. The application of nano-optical techniques to the study of SNSPD device properties is relatively new. In previous studies using a confocal microscope configuration the photoresponse over the whole of a 10 µm x 10 µm area SNSPD has been measured and a highly constricted area of an SNSPD has been imaged [7]. In this chapter (section 4.3) the photoresponse from larger area (20 µm x 20 µm) SNSPDs was investigated along with polarisation dependent features.

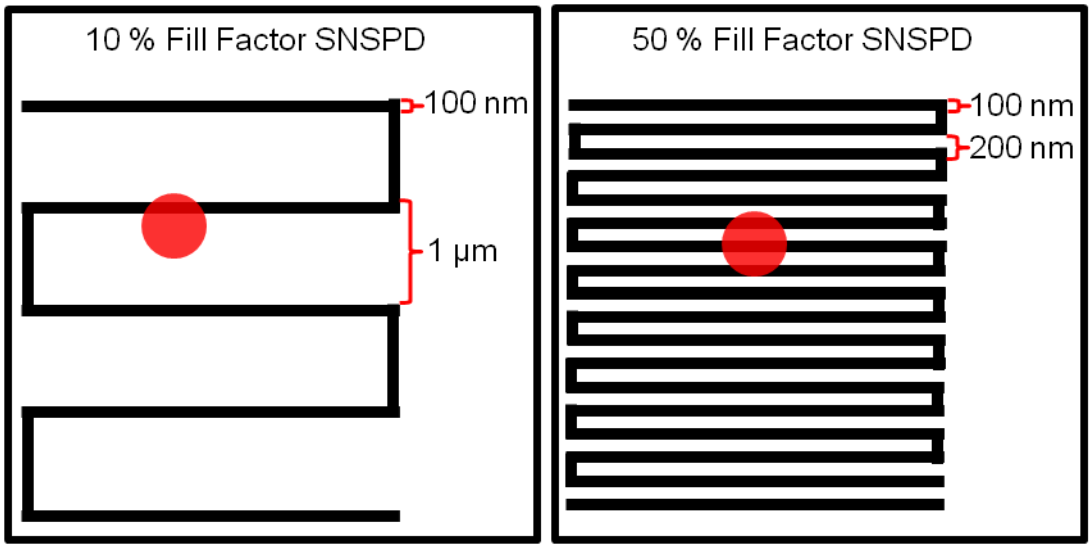

Figure 4.1 – Schematics (not to scale) of 10 % (left) and 50 % (right) fill factor SNSPDs. The red circle is a focal spot (~ 200 nm diameter), showing that only individual nanowires can be illuminated in the 10 % SNSPD.

The resolution tests in section 3.4.3 gave rise to the idea of possibly resolving the individual wires of SNSPDs. To do this we used a specifically designed SNSPD which had a fill factor of 10 % (corresponding to an increased pitch from 200 nm to 1µm) (see Figure 4.1), meaning that a focal spot size of ~ 200 nm should be able to clearly resolve

the individual wires [8]. The imaging of wires and study of polarisation effects in this specifically designed 10 % fill factor SNSPD is discussed in section 4.4. The work in this chapter was carried out with Paul Dalgarno, Richard Warburton and Robert Hadfield.

4.2 Measurement Setup

As described in section 3.4 (see Figure 3.10), a confocal microscope configuration with liquid helium cooling was used to study localized areas of SNSPD devices. The SNSPD was mounted on a stack of piezoelectric linear positioners providing movement in three axes (X, Y, and Z) used for focusing and course positioning and a piezoelectric X-Y scanner, for precision movement of the SNSPD. The X-Y scanner was used to either raster scan across the SNSPD active area producing a photoresponse map, or was used to move precisely to local areas of interest due to the nm movement resolution.

The measurements were performed using continuous wave (CW) lasers of wavelength 950 nm or 470 nm and an objective lens with $NA = 0.65$. This gave diffraction-limited spot resolution of 760 nm and 376 nm FWHM at 950 nm and 470 nm wavelengths respectively without the use of solid immersion lenses (SILs). This provided sufficient optical resolution to accurately map out the photoresponse of SNSPDs.

The system was setup and aligned at room temperature and then placed in a stainless steel tube which is vacuum sealed. The tube was then evacuated down to a pressure of $\sim 10^{-5}$ mbar, and then ~ 20 mbar of helium exchange gas was introduced. It is essential to remove air and moisture from the tube, as upon cooling these could freeze possibly onto the optics, positioners or the SNSPD, potentially breaking these delicate components. The exchange gas was used to provide thermal contact to the liquid helium bath inside the dewar which cools the SNSPD down to ~ 4 K. To prevent extreme changes in the environment seen by the part of the system that is cooled, pre-cooling in liquid nitrogen (77 K) was carried out, before the stainless steel tube was inserted into the liquid helium dewar. This pre-cooling step also reduced the helium boil off rate when the tube was inserted giving a longer measurement time.

The SNSPD biasing and readout was performed utilizing a bias-tee (see Figure 3.10). The bias current was applied through the low frequency port reaching the device through the combined port. This bias current cannot travel through the high frequency port of the bias-tee. The fast voltage pulse produced by the SNSPD detecting a photon travels back through the combined port and out of the high frequency port. The low frequency port blocks the fast voltage pulse from travelling through it. The fast voltage pulse was then amplified using a chain of low noise room temperature amplifiers (RF Bay LNA – 580 and RF Bay LNA – 1000, 580 MHz and 1000 MHz bandwidth respectively) providing a combined gain of 56 dB.

4.3 Photoresponse Mapping Measurements on 50% Fill Factor SNSPD in the Liquid Helium Confocal Microscope Configuration

4.3.1 Electrical Characterisation of the 50% Fill Factor SNSPD

A SNSPD with 50 % fill factor, 100 nm wide wires and 200 nm pitch was selected (see schematic Figure 4.1 right). The device had an active area of 20 µm x 20 µm. This device has an area four times greater than typical 10 µm x 10 µm area SNSPDs [7, 9] and the overall length of the nanowire is four times greater. This large area SNSPD is more susceptible to fabrication errors and thus is more likely to contain constrictions which limit the performance and sensitivity. Electrical and optical characterization measurements were carried out on this device to determine its performance attributes.

Photoresponse mapping and consequently detection efficiency mapping, gives a very accurate overview of the response of the SNSPD to light at the single-photon level. Along with the electrical measurements, these data show if there are any constrictions and if they are confined to one region or are spread out over a larger area of the SNSPD.

The I-V curve of the measurement with a 50 Ω shunt resistor (Figure 4.2) gave an I_c value of 18 µA. The 50 Ω shunt resistor was included to avoid latching as explained in section 3.7.1.

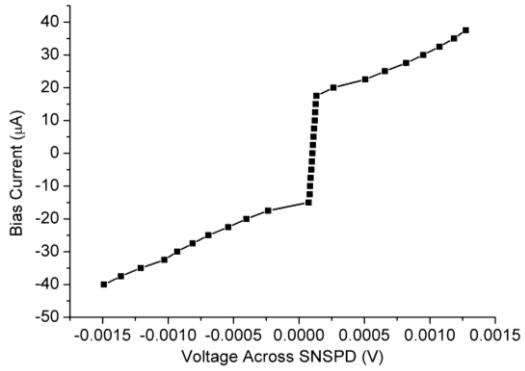

Figure 4.2 – The current - voltage (I-V) characteristics of a 50 % fill factor SNSPD with a 50 Ω shunt resistor in parallel with the SNSPD measured *in situ* in the liquid helium confocal microscope configuration. The critical current for the 50 % fill factor SNSPD is 18 μA.

As shown in Figure 4.3 the upturn in inductance for the measured SNSPD device is shallow (red crosses) compared with the ideal $C = 1$ case (black line). By fitting the measured data to the theoretical curve (red line), the only variable, the degree of constriction C, was found to be 0.376. This suggests that there is either a dense region of constrictions or a range of constrictions covering a larger area of the SNSPD.

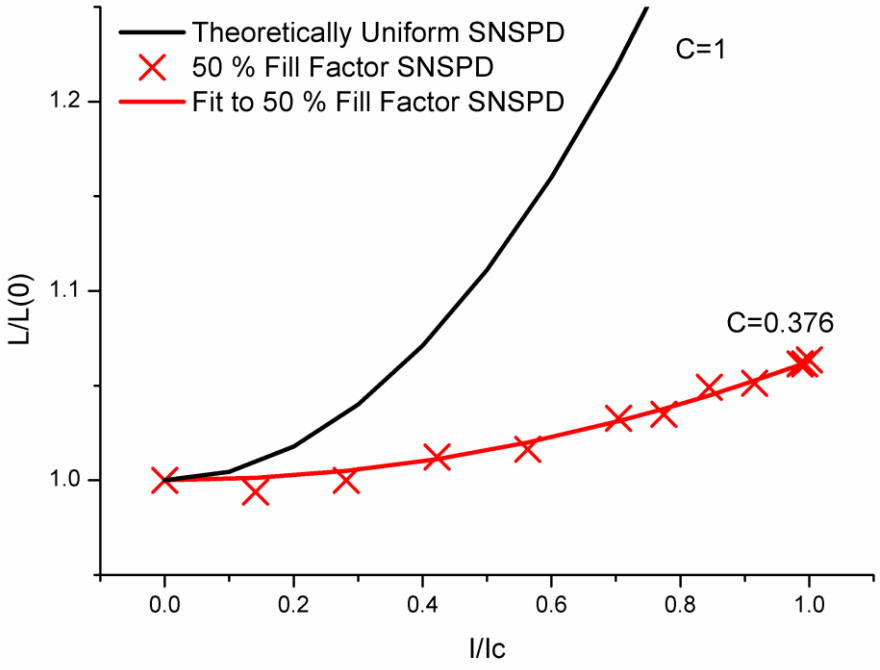

Figure 4.3 – The kinetic inductance and constriction factor *C* measurement of the 50 % fill factor SNSPD. The black line is the theoretical curve for a perfectly uniform SNSPD (*C* = 1). The red crosses are the experimental data showing the upturn in inductance as the bias current is increased. The red line is a theoretical fit giving a constriction factor *C* value of 0.376 for the 50 % fill factor SNSPD.

4.3.2 Photoresponse Mapping of the 50 % Fill Factor SNSPD at λ = 1550 nm in the Liquid Helium Confocal Microscope Configuration

Photoresponse mapping has previously been used to image a highly constricted SNSPD and to compare its response to that of a uniform SNSPD [7, 10]. Photoresponse mapping of the SNSPD was performed in order to determine if the photosensitive area of the device had a large area or was localised at one specific position. By measuring the count rate of detected incident photons at specific positions and knowing the input photon flux, the localized detection efficiency (*DE*) across the SNSPD was found.

The SNSPD was illuminated with light from a CW laser of wavelength 950 nm and a focal FWHM spot size of 760 nm. The photon flux was 1.8 x 10^6 photons per second and the dark count rate (DCR) was 200 Hz.

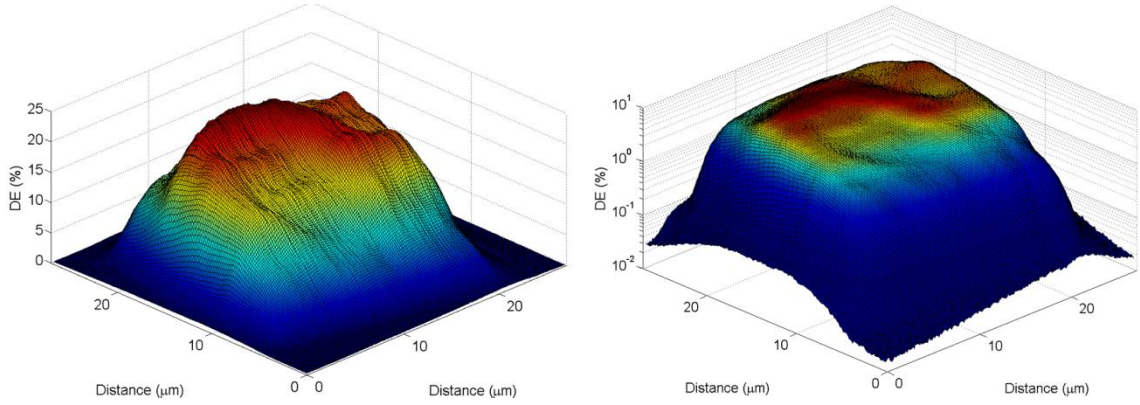

Figure 4.4 – A detection efficiency (DE) map of the 50 % fill factor SNSPD (20 μm x 20 μm area), using 950 nm wavelength light, a photon flux of 1.8 x 10^6 photons per second at 200 Hz dark count rate (DCR). The maximum detection efficiency achieved is 23.8 %. Left – linear scale, Right – logarithmic scale.

The *DE* map [8] (Figure 4.4) shows that the point of lowest *DE* is approximately a quarter of the maximum *DE* point. The *DE* map shows regions of high efficiency compared to the rest of the SNSPD. This shows that the constrictions predicted by the electrical characterization are distributed over a significant region of the total SNSPD device area. The constricted region has a higher current density than the rest of the SNSPD. This higher current density region limits the maximum current biasing that is possible, thus limiting the performance available. The maximum and minimum *DE* measured in this map are 23.8 % and 6.6 % respectively.

4.3.3 The Polarisation Dependence of the 50 % Fill Factor SNSPD at λ = 950 nm

A Glan Taylor polarizer and a half-waveplate was introduced into the measurement setup, in order to investigate polarization dependence in the SNSPD. The Glan Taylor polarizer and the half-waveplate were placed in the collimated beam path with the Glan Taylor polarizer before the half-waveplate. The Glan Taylor polarizer was used to set the polarization state and the half-waveplate to rotate the polarization state of the incident light. The polarization state rotates the electric field of the incident light between orthogonal states with a rotation of 45° (see Figure 4.5).

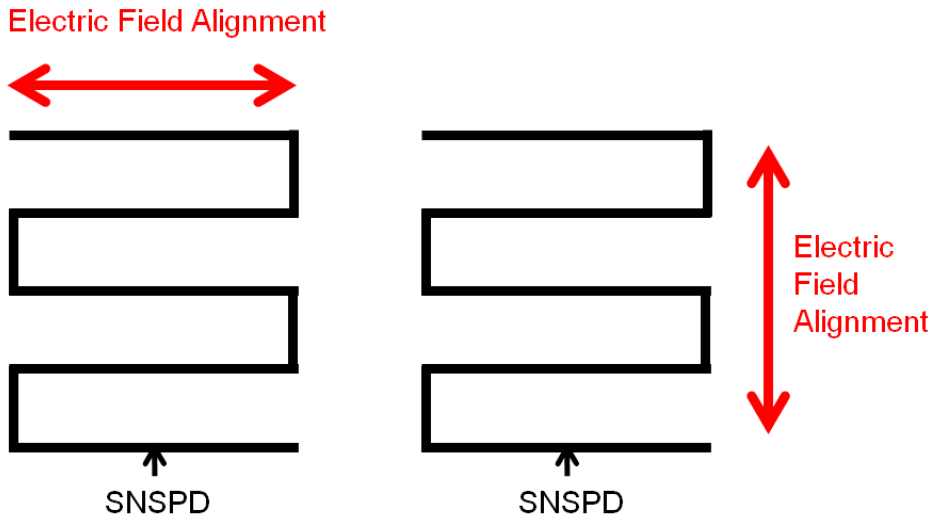

Figure 4.5 – The alignment of the electric field of the incident light when observed at 50° (left) and 95° (right) half waveplate angles (+ integer number of 90°). The SNSPD layout is a schematic (not to scale).

Simulations predicting the absorption of light into SNSPDs (for both 50 % and 10 % fill factor devices) for both parallel and perpendicular polarisations at λ = 470, 900 and 1550 nm were performed by Vikas Anant from MIT. These simulations (see Appendix I) expand on earlier published simulations at a fixed wavelength of λ = 1550 nm [11]. These simulations show that at short wavelengths light perpendicular to the nanowires has a higher absorption compared to light polarised parallel to the nanowires. As the wavelength of light is increased, light polarised parallel to the nanowires is predicted to have higher absorption compared to perpendicularly polarised light. This is true for both 50 % and 10 % fill factor SNSPDs. The difference between the different fill factor devices is that as the wavelength is increased from λ = 470 nm to λ = 1550 nm, the ratio of the absorption between the parallel to perpendicularly polarised light increases to a

differing extent, 0.794 to 2.191 and 0.942 to 1.890 for the 10 % and 50 % fill factor devices respectively.

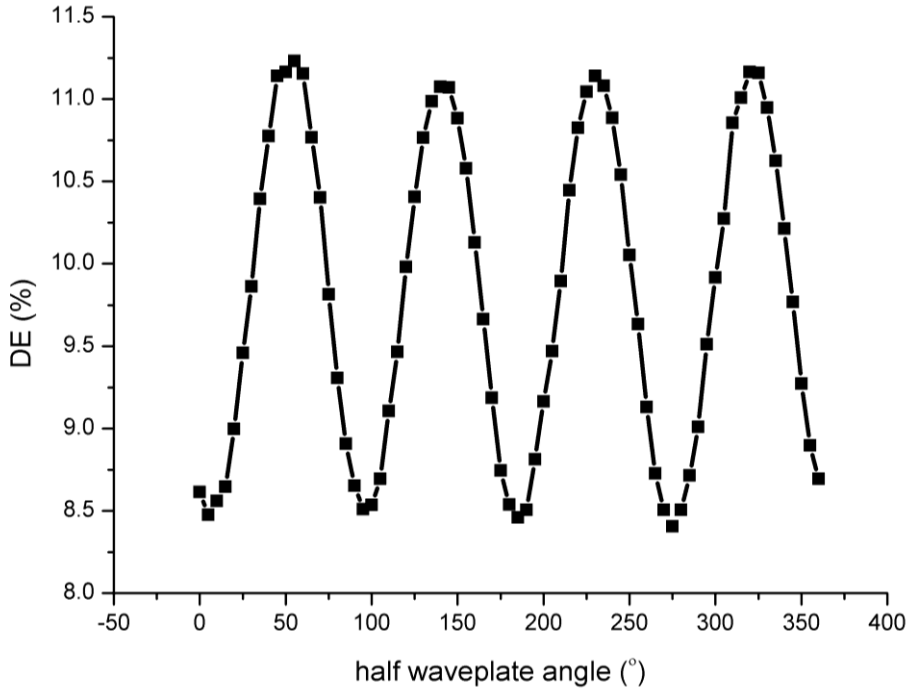

Figure 4.6 – The polarisation dependence of the detection efficiency of the 50 % fill factor SNSPD at λ = 950 nm. With the half waveplate at orientated 50° (+ integer number of 90°) the electric field is aligned parallel to the nanowires, providing increased absorption of incident photons thus increasing the detection efficiency. At an orientation of 95° (+ integer number of 90°) the electric field is aligned perpendicular to the nanowires and the absorption and detection efficiency is minimised.

In Figure 4.6 the maxima in the count rate with varying polarization (50° + integer number of 90°) relate to aligning the electric field parallel to the nanowires of the SNSPD. The minima occur when the electric field is oriented perpendicular to the nanowires. These measurements show that an electric field aligned parallel to the nanowires promotes the absorption of photons. This result agrees qualitatively with experimental and modelling results provided by Anant (Appendix I). We confirmed that the simulations qualitatively agree with fibre coupled polarisation dependent measurements of both 10 % and 50 % fill factor SNSPDs (Appendix I). These measurements follow the same trend as the simulation. The difference between the simulations and the experimental results are due to differences in the input parameters, specifically the values of the real and imaginary parts of the refractive index (*n* and *k*) used for the substrate. The simulation used a sapphire substrate but the measured SNSPD had an MgO substrate. There is the possibility that the *n* and *k* values of the

NbN nanowire are slightly incorrect. These values are determined from ellipsometry measurements on unpatterned NbN films at room temperature [12]. The true values for the patterned nanowires at cryogenic temperatures may differ. The ratio of light aligned with the electric field perpendicular to the nanowires compared to alignment parallel to the nanowires was 0.757, meaning that the low count is 75.7 % of the high count value.

4.4 Photoresponse Mapping Measurements of the 10% Fill Factor SNSPD in the Liquid Helium Confocal Microscope Configuration

4.4.1 Electrical Characterisation of the 10% Fill Factor SNSPD

The optical resolution that can be achieved using the confocal microscope configuration has been detailed in the previous section (section 3.4.3). It was found to be on the scale of a few hundred nanometres. A focal spot of this size can be used to probe localized areas of SNSPDs. It is also potentially possible to resolve individual wires in a SNSPD. For this study a specifically designed 10 % fill factor device (20 μm x 20 μm area with 100 nm wide wires and a 1 μm period) was chosen. From the Sparrow Criterion (see equation (2.9)) an objective lens with NA = 0.65 at λ = 950 nm should give a focal spot of 760 nm FWHM, giving sufficient resolution to resolve the individual wires.

In order to resolve individual nanowires the meander wire must be uniform as constrictions will limit the photosensitivity of any non-constricted regions of the SNSPD. To determine if the SNSPD is a good candidate for resolving individual wires, electrical characterization was performed as for the 50 % fill factor SNSPD (section 4.3).

The critical current (I_c) was determined from the current-voltage (I-V) characteristics of the SNSPD (see Figure 4.7) and found to be 28 μA. This gave the range of current biasing values for the inductance and the degree of constriction measurements (see Figure 4.8). The significance of a higher value of I_c between the 50 % and 10 % fill factor SNSPDs relates to the uniformity of the SNSPDs. Non-uniform or constricted SNSPDs, specifically at the constricted regions, cannot support high current densities

without switching into the resistive state. At the other less or non-constricted regions of the SNSPD the current density is lower and thus the sensitivity to incident photons is lower. The overall length of the nanowire in the 50 % fill factor SNSPD is 2 mm, whereas the nanowire length of the 10 % fill factor SNSPD is 0.4 mm. Thus the variation in I_c seen between these SNSPDs indicates that the shorter nanowires is more uniform.

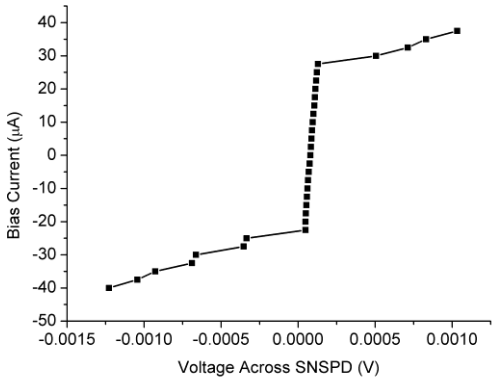

Figure 4.7 – The current – voltage (I-V) characteristics of the 10 % fill factor SNSPD with 50 Ω shunt resistor in parallel with the SNSPD measured *in situ* in the liquid helium confocal microscope configuration. The critical current for the 10 % fill factor SNSPD is 28 μA.

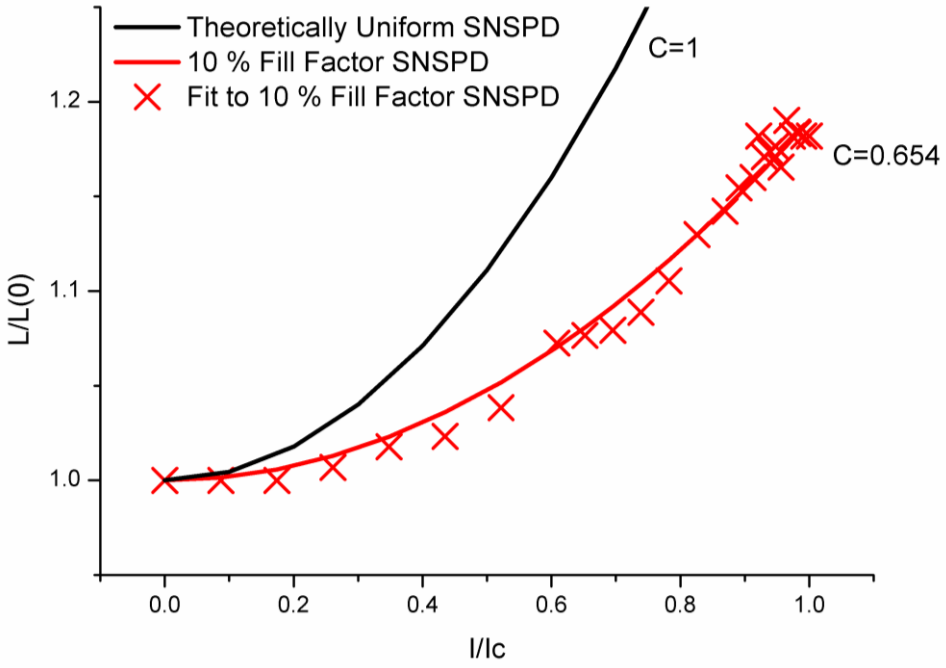

Figure 4.8 – The kinetic inductance and constriction factor *C* measurement for the 10 % fill factor SNSPD. The black line is the theoretical curve for a perfectly uniform SNSPD. The red crosses are the experimental data showing the upturn in inductance with increasing bias current. The red line is the measured fit giving a constriction factor *C* value of 0.654 for the 10 % fill factor SNSPD.

The SNSPD has a critical current value of 28 µA and a constriction factor C = 0.654. This C value is a high value, such that the response from the SNSPD should be sufficiently uniform to resolve the individual wires. This SNSPD device was selected as the ideal candidate for use in the resolution of individual wires.

4.4.2 Photoresponse Mapping of the 10 % Fill Factor SNSPD at λ = 950 nm

The SNSPD was illuminated with light from a CW laser of wavelength 950 nm and a focal FWHM spot size of 760 nm. The photon flux was 1.8 x 10^6 photons per second and the dark count rate (DCR) was 200 Hz.

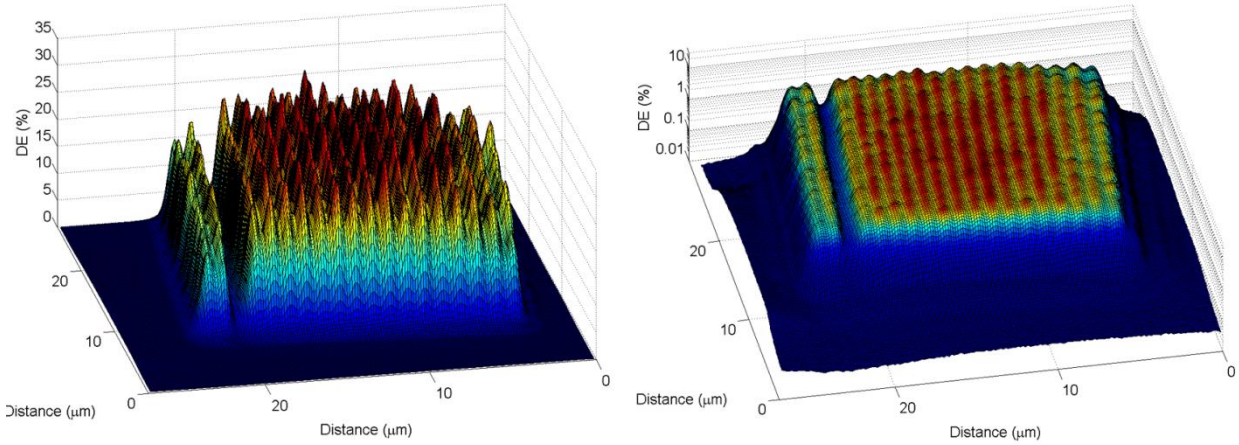

Figure 4.9 – A detection efficiency (*DE*) map of the 10 % fill factor SNSPD (20 µm x 20 µm area), using 950 nm wavelength light, photon flux of 1.8 x 10^6 photons per second at 200 Hz dark count rate (DCR). The maximum detection efficiency achieved is 28.6 %. Left – linear scale, Right – logarithmic scale.

The *DE* map (Figure 4.9) clearly shows the individual wires of the SNSPD [8]. The expected profile is the convolution of a Gaussian profile with a step profile due to the focal spot being Gaussian and the nanowires acting as a step function (see Figure 4.10). We expect the *DE* to drop to 60 % of the peak value in the gaps between the wires following the simulations in Figure 4.11; in practice in the meander in Figure 4.9 we observe a value of 78 % of the maximum in the gaps.

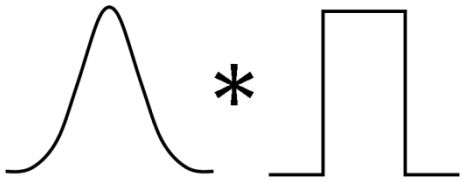

Figure 4.10 – The convolution of Gaussian profile (representing the optical spot profile) with a step function (the absorption cross-section of the nanowire).

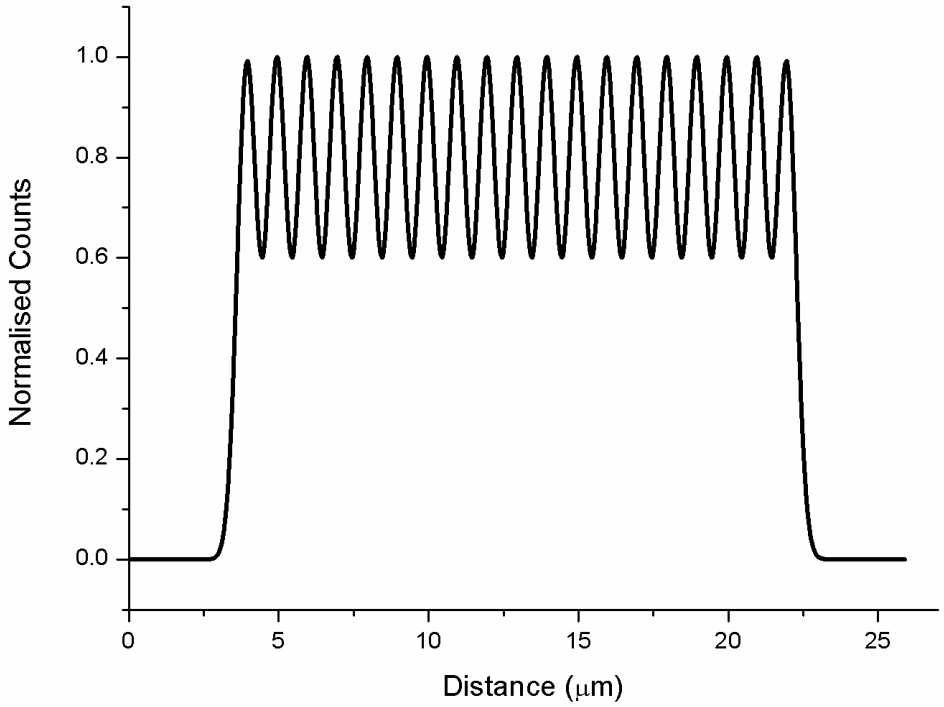

Figure 4.11 – A one-dimensional (1D) simulation of the expected line scan profile of the 760 nm FWHM spot size traversing the 10 % fill factor SNSPD perpendicular to the nanowires. The simulation is the convolution of a Gaussian profile with a FWHM spot size of 760 nm with a step function for each nanowire.

Figure 4.11 shows the convolution of the periodic step function of the 10 % fill factor SNSPD with a Gaussian beam. The Gaussian beam had a FWHM spot size of 760 nm, which matches the measured spot size in Figure 4.9. The underlying reason for this effect may be because the space between the wires is not empty. The SNSPD has the same pattern with 100 nanowires (for a 50 % fill factor SNSPD) but only every tenth nanowire is connected in the meander pattern. Scattering may occur from the redundant wires and reflections may also occur from the back surface of the substrate due to the a mismatch in refractive indices. Both of these mechanisms could provide a larger than expected signal between the nanowires.

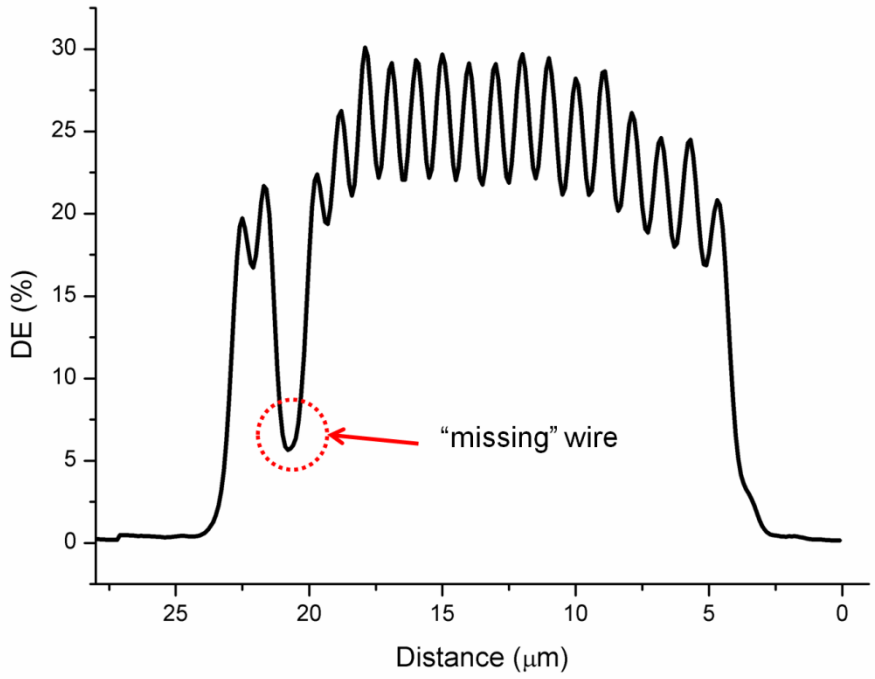

Figure 4.12 – A single line scan perpendicular to the direction of the nanowires of the 10 % fill factor SNSPD, at a wavelength of 950 nm, 200 Hz dark count rate, and a spot size of 760 nm FWHM. A "missing" nanowire with reduced detection efficiency at 20 μm distance is indicated (red dashed circle).

The most startling thing about the *DE* map (Figure 4.9) is the 'missing' wire. This wire must still be electrically connected in the meander wire. The probable reason for the wire being 'missing' from the response map (Figure 4.9) is a fabrication error. This segment of wire must be wider than the rest of the wire so was not current biased to the same current density as the rest of the nanowire. This severely reduces its sensitivity to photons causing it to respond with very poor *DE*. The maximum detection efficiency observed in the 10 % fill factor SNSPD was 28.6 % at 200 Hz dark count rate using light of 950 nm wavelength. A single line scan (Figure 4.12) taken through the middle of the SNSPD perpendicular to the direction of the nanowires clearly illustrates the missing wire position (red dashed circle).

4.4.3 Photoresponse Mapping of the 10 % Fill Factor SNSPD at λ = 470 nm

To determine if better resolution between the nanowires could be achieved, a smaller focal spot was used. To achieve this smaller focal spot the wavelength of incident light was reduced to 470 nm, because from the Sparrow Criterion (see equation (2.9)), a shorter wavelength reduces the focal spot size. A focal spot size of 370 nm FWHM was achieved.

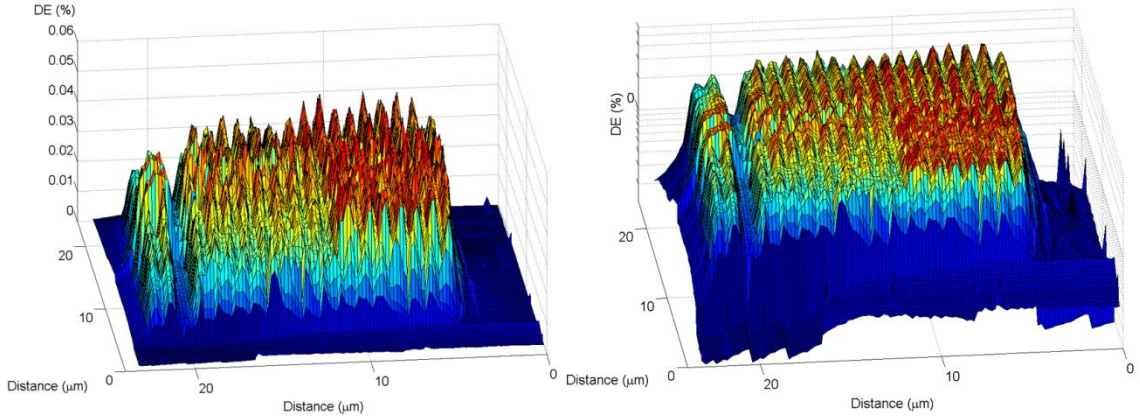

Figure 4.13 – A detection efficiency map (*DE*) of the 10 % fill factor SNSPD (20 µm x 20 µm area), using 470 nm wavelength light, a photon flux of 5 x 10^9 photons per second at 10 kHz dark count rate (DCR). The maximum *DE* achieved is 0.06 %. Left – linear scale, Right – logarithmic scale.

The detection efficiency map in Figure 4.13 is the combination of four smaller detection efficiency maps. This is because during the measurements at 470 nm wavelength the X-Y scanner only had a scan range of 12 µm x 12 µm (the larger area X-Y scanner was unavailable). The 10 % fill factor SNSPD has a maximum detection efficiency of 0.06 % at 470 nm at 10 kHz dark count rate. This value is significantly lower than expected, most likely due to the very high a photon flux (~ 5 x 10^9 photons per second) incident on the SNSPD. With this high photon flux the sample temperature would increase leading to poorer performance. The optical power incident on the SNSPD at λ = 470 nm was 2.11 nW, which is four orders of magnitude larger than at λ = 950 nm (incident power = 0.37 pW).

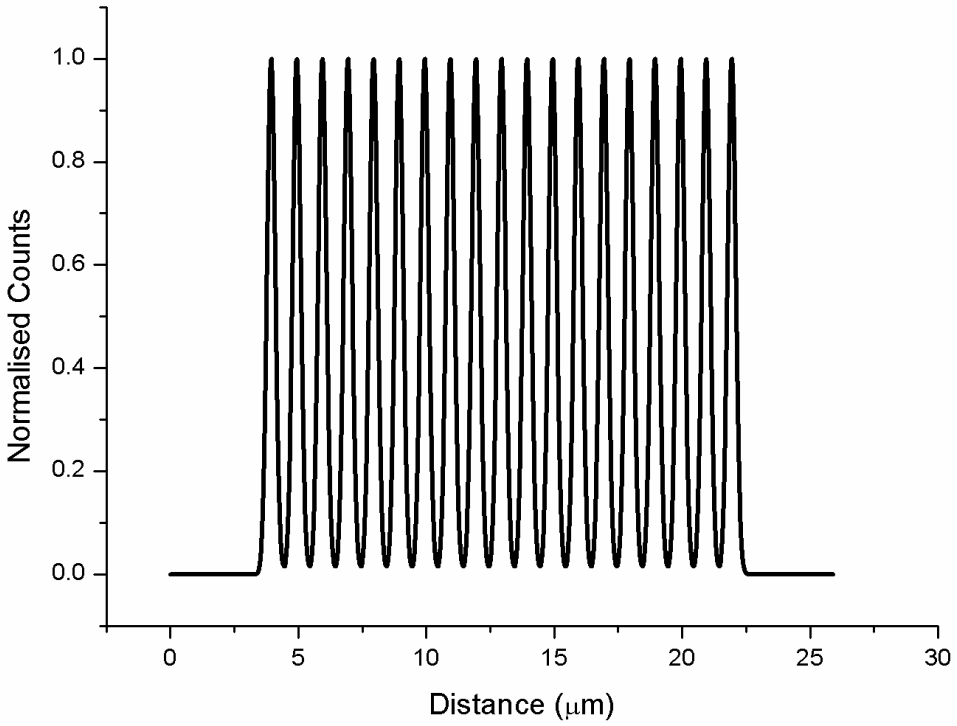

Figure 4.14 – A one dimensional (1D) simulation of the expected line scan profile of 370 nm FWHM spot (diffraction limit from the Sparrow criterion) moved across the 10 % fill factor SNSPD perpendicular to the nanowires. The simulation is the convolution of a Gaussian profile with a spot size of 370 nm FWHM with a step function for each nanowire.

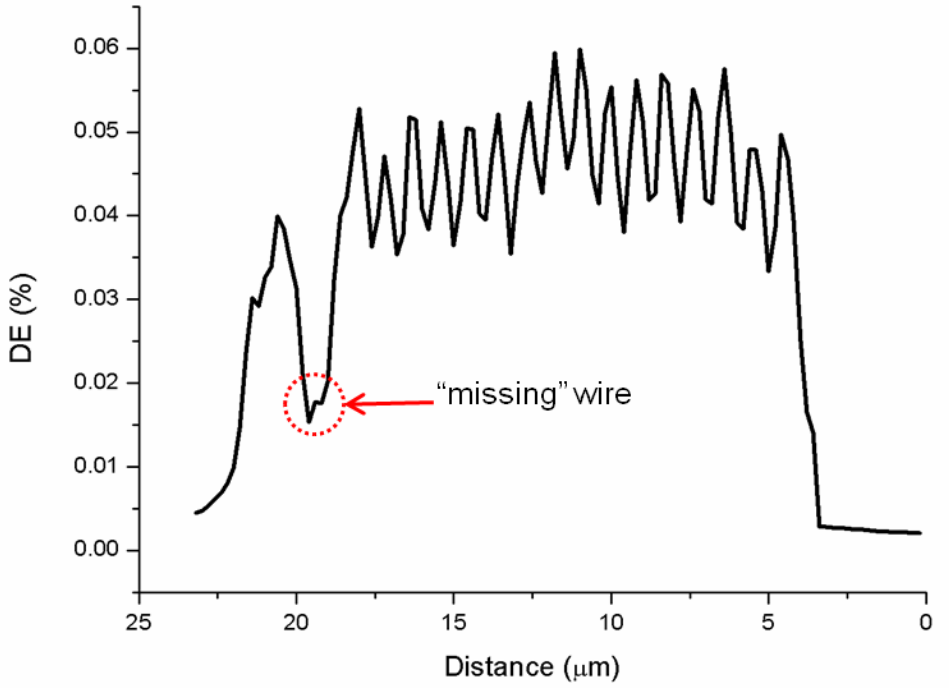

Figure 4.15 – A line scan perpendicular to the nanowires of the 10 % fill factor SNSPD. Measured at a wavelength of 470 nm, 10 kHz dark count rate, and a spot size of 370 nm FWHM (diffraction limit from the Sparrow criterion). Once again the "missing" nanowire is visible with reduced detection efficiency at 20 µm distance (red dashed circle).

The depths of the troughs of the line scan are only 35 % of the peak value (see Figure 4.14). Again the detection efficiency (see Figure 4.15) does not drop to zero in the troughs.

4.4.4 Photoresponse Mapping of the 10 % Fill Factor SNSPD at λ = 470 nm with a Hemispherical Solid Immersion Lens (h-SIL)

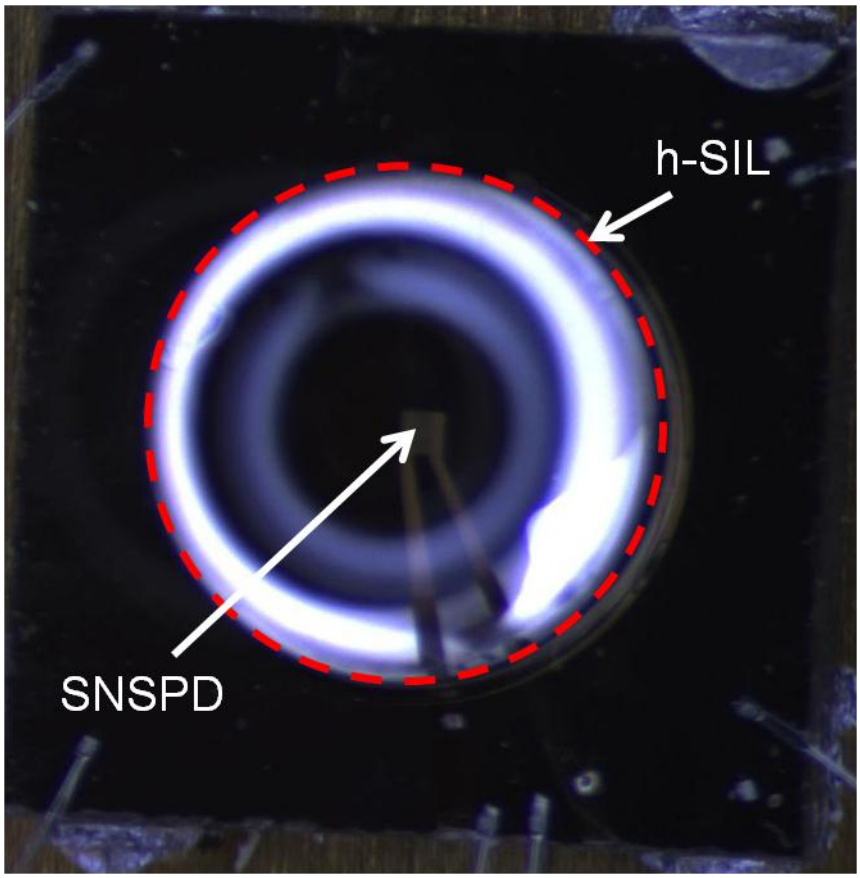

Figure 4.16 –A stereo optical microscope image of a h-SIL mounted on top of 10 % fill factor SNSPD. The h-SIL diameter is 2 mm and the overall size of the SNSPD chip is 3 mm x 3 mm.

A second method using a glass h-SIL (see Figure 4.16) with a refractive index of 2 was implemented to achieve greater resolution. This gave a focal spot size of 300 nm at FWHM at λ = 470 nm. When using an h-SIL the range of the X-Y scanner is reduced by a factor of the refractive index of the h-SIL. Only one position, covering a 4 µm x 4 µm area, was measured due to the short supply of liquid helium. The depth contrast between the nanowires was increased to 70 % of the peak value (see Figure 4.18) with this reduced focal spot size. Again a maximum detection efficiency of

0.06% at a dark count rate of 10 kHz and λ = 470 nm (see Figure 4.17) was measured in this SNSPD with the implementation of an h-SIL.

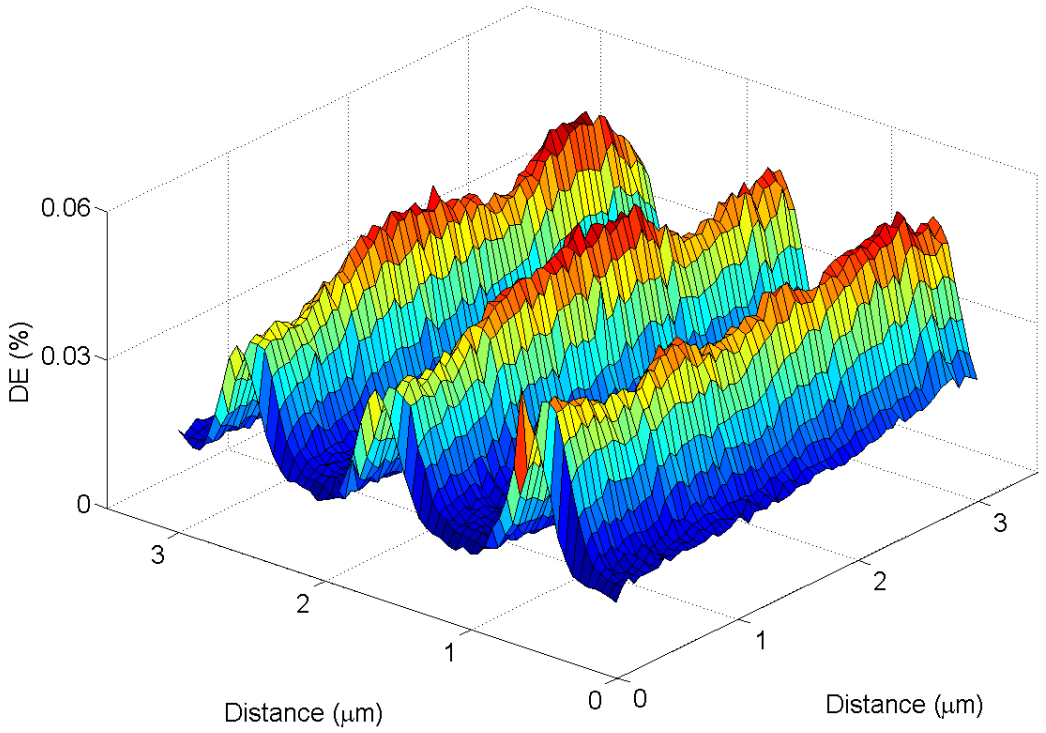

Figure 4.17 – A detection efficiency (*DE*) map of a small section of the 10 % fill factor SNSPD, using a hemispherical solid immersion lens (h-SIL), 470 nm wavelength light, a photon flux of 5 x 10^9 photons per second at 1 kHz dark count rate (DCR). The photon flux was 5 x 10^9 photons per second. The maximum *DE* achieved is 0.06 %.

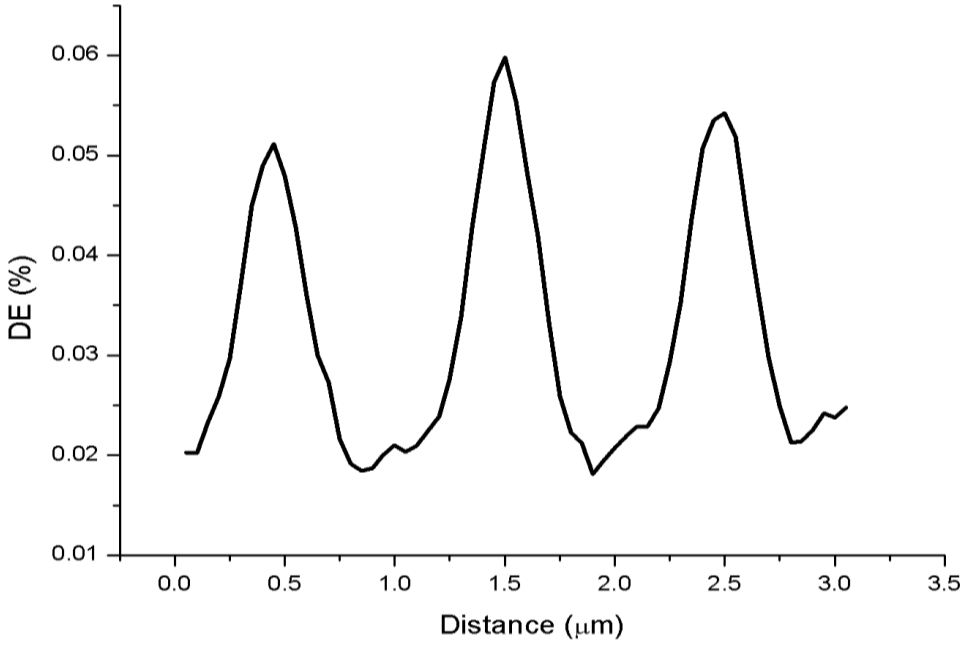

Figure 4.18 – A line scan perpendicular to the nanowires of the 10 % fill factor SNSPD using an h-SIL. These measurements were taken at a wavelength of 470 nm, 10 kHz dark count rate, and a spot size of 300 nm FWHM. The photon flux was 5 x 10^9 photons per second.

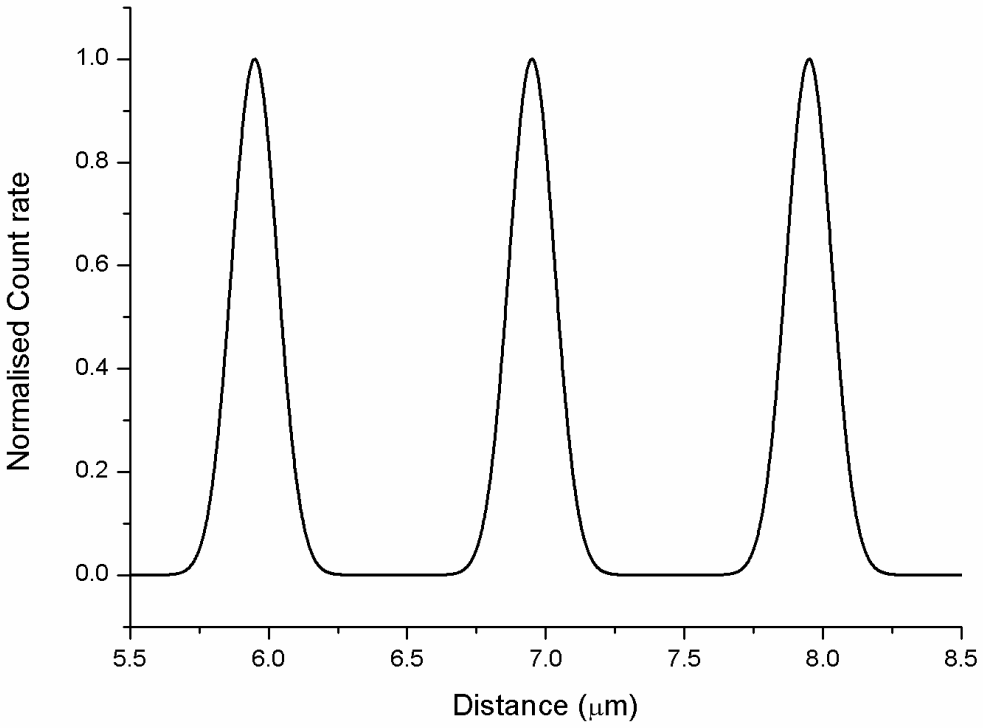

Figure 4.19 – A one dimensional (1D) simulation of the expected line scan profile of 300 nm FWHM spot size (calculated using the h-SIL at λ = 470 nm) moved across the 10 % fill factor SNSPD perpendicular to the nanowires. The simulation is the convolution of a Gaussian profile with a FWHM spot size of 300 nm with a step function for each nanowire.

The background level does not drop to zero between the nanowires (see Figure 4.18) due to the scattering and reflections from the backside of the substrate detailed earlier.

4.4.5 The Polarisation Dependence of the 10 % Fill Factor SNSPD at λ = 950 nm

As for the 50 % fill factor SNSPD measured in section 4.3.3 polarisation dependence measurements were also performed on the 10 % fill factor SNSPD. Due to the wider spacing between the nanowires, the SNSPD should be less susceptible to the electric field orientation. As before the half-waveplate was rotated to vary the polarisation. Again the results show that a higher count rate is observed with the electric field aligned parallel to the nanowires, meaning that the photon sensitivity is increased in this orientation.

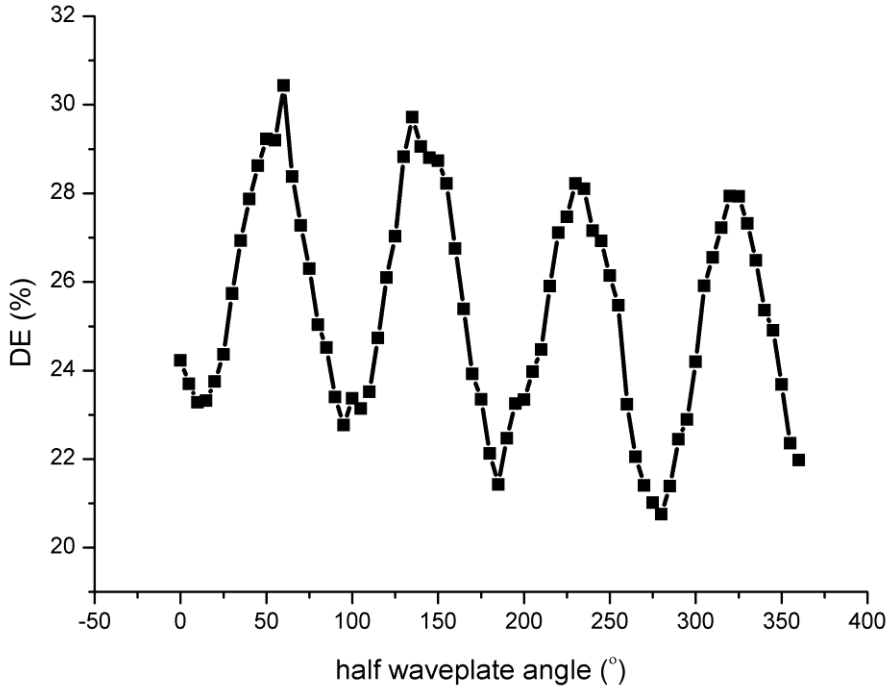

Figure 4.20 – The polarisation dependence of the 10 % fill factor SNSPD using 950 nm wavelength light at 1 kHz dark count rate. The photon flux was 1.8 x 10^6 photons per second.

The ratio of light absorbed with the electric field aligned perpendicular to the nanowires compared to electric field alignment parallel to the nanowires was 0.686 (see Figure 4.20), meaning that the low count is 68.6 % of the high count value. This shows that there was a smaller contrast between the high and low counts for the 10 % SNSPD compared to the 50 % fill factor SNSPD. This agrees qualitatively with simulations performed by Vikas Anant at MIT (see Appendix I). The simulations were performed at λ = 900 nm and determine the theoretical absorption of photons into the SNSPD. The results showed that for the 10 % fill factor SNSPD light polarised with the electric field aligned perpendicular to the nanowires would absorb a larger number of photons compared to when the electric field is aligned parallel to the nanowires (ratio of perpendicular to parallel polarised light is 1.09). This agrees with the simulations for the 10 % fill factor SNSPD as they show that below $\lambda \sim$ 950 nm, there is higher absorption from light which is polarised perpendicular to the nanowires.

4.5 Comparison of 50 % and 10 % Fill Factor SNSPDs

A comparison between the characteristics of the 50 % and 10 % fill factor SNSPDs was made to show the relative merits of both SNSPDs.

	50 % Fill Factor SNSPD	10 % Fill Factor SNSPD
I_c (μA)	18	28
C	0.376	0.686
DE (Maximum) (%) at λ = 950 nm	23.8	28.6
Ratio of Parallel to Perpendicular Polarisation *DE* at λ = 950 nm (Experimental)	0.757	0.686
Ratio of Parallel to Perpendicular Polarisation *DE* at λ = 900 nm (Simulation)	1.096	0.915

Table 4.1 – A comparison of the characteristics of the 50 % and the 10 % fill factor SNSPDs measured in the liquid helium confocal microscope configuration.

Table 4.1 shows that the 10 % SNSPD has better performance characteristics compared to the 50 % fill factor SNSPD. The increased critical current (I_c) allows for increased current biasing which increases the sensitivity and detection efficiency (*DE*) of the SNSPD. The degree of constriction factor (*C*) shows that the 10 % fill factor SNSPD is more uniform, containing less constricted regions which improve the overall *DE*. The ratio of the parallel to perpendicular *DE* values of the 10 % fill factor SNSPD is lower than the 50 % fill factor SNSPD. This shows that the 10 % fill factor SNSPD is more

polarisation sensitive than the 50 % fill factor SNSPD for λ = 950 nm. Simulations performed by Vikas Anant do not completely agree qualitatively with this (see Appendix I). Fibre-coupled measurements of polarisation dependence on 10 % and 50 % fill factor SNSPDs at λ = 830, 1310 and 1550 nm give better qualitative agreement with the simulations. These measurements and simulations also show that at ~ λ = 950 nm, the polarisation alignment that is preferential for absorption swaps from parallel to perpendicularly polarised light as the wavelength is increased.

4.6 Instrumental Response Function (Timing Jitter) of the 50 % and 10 % Fill Factor SNSPDs

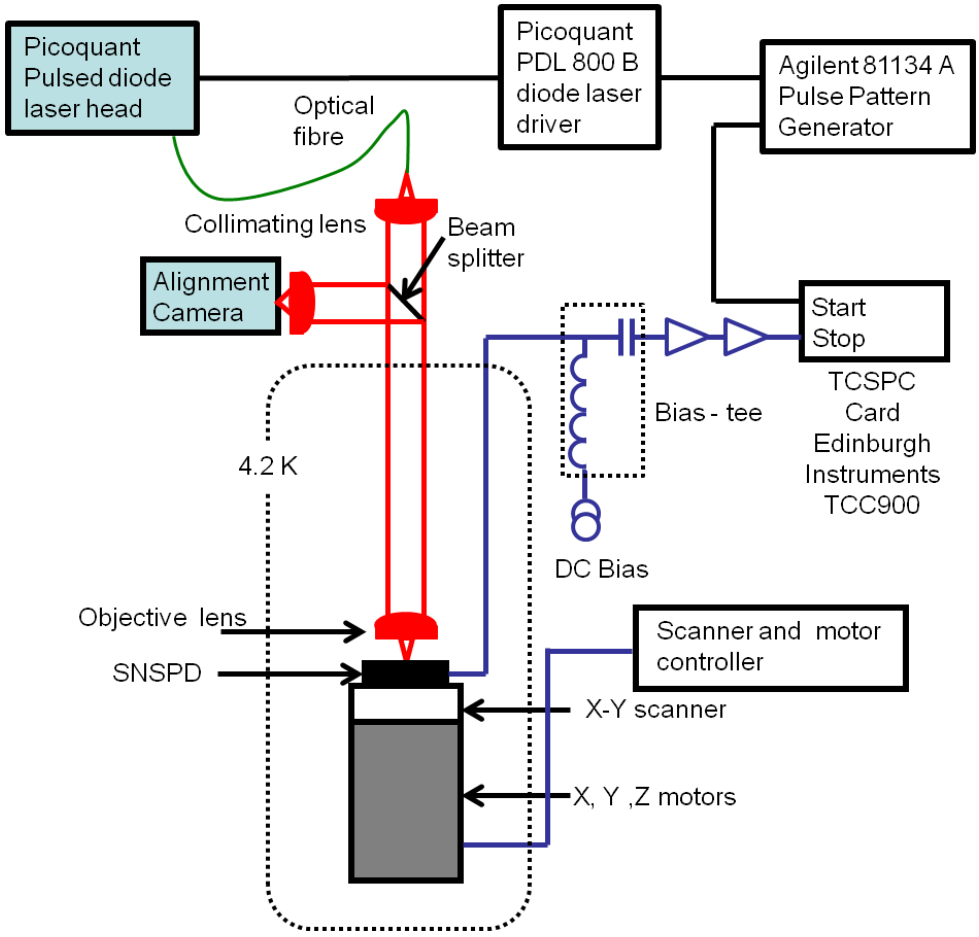

Figure 4.21 – Jitter measurements in the liquid helium confocal microscopy configuration. The Agilent 81134 A pulse pattern generator (PPG) is used to drive the pulsed diode laser (λ = 405 nm for the 10 % fill factor SNSPD and λ = 975 nm for the 50 % fill factor SNSPD) at a frequency of 20 MHz. The light from the pulsed diode laser is incident on the SNSPD, the output pulses are read out through the bias – tee and into the "stop" trigger of the TCSPC card. The "start" trigger is connected to the synchronised output from the PPG, which is synchronised with the laser pulses.

Initial measurements of the instrumental responses of both the 50 % and 10 % fill factor SNSPDs were carried out.

Figure 4.21 details the measurement setup. The pulse pattern generator output connection (PPG) (Agilent 81134 A) was used to drive the 975 nm wavelength pulsed diode laser at a clock rate of 20 MHz. The synchronised output from the PPG was used as the "start" trigger on the time correlated single-photon counting (TCSPC) card (Edinburgh Instruments TCC 900) and the output pulse from the detection of photons of the SNSPD was used as the "stop" trigger. A Gaussian jitter histogram (corresponding to the overall instrumental response function) was recorded by the TCSPC electronics. The histogram was fitted and the full width at half maximum (FWHM) value is the timing jitter of the SNSPD.

The focal spot was positioned over the centre of the SNSPD. This was done by two separate methods, using the piezoelectric X-Y scanner to move the focal spot very accurately to the centre of the SNSPD, and using the X and Y piezoelectric linear positioners to move more roughly to the centre of the SNSPD.

For the 50 % fill factor SNSPD, the timing jitter of the whole system was found to be 187 ps FWHM (see Figure 4.22). This is higher than the sub 100 ps FWHM jitter expected [13]. This increased timing jitter was caused by electrical pick-up from the piezoelectric X-Y scanner connections. Having the X-Y scanner connected to the scanner driver highlighted that the grounding of the electrical connections in the system was not perfect, and was causing ground loops which were affecting the timing jitter measurements. Simply disconnecting the X-Y scanner connection to the scanner driver improved the system timing jitter to 144 ps FWHM (see Figure 4.22).

The electrical grounding to the SNSPD was investigated to try and improve this further. Different arrangements of linking ground connections together and even electrically isolating the SNSPD so it was *floating* electrically were all investigated. None of these improved the value of the system timing jitter. 144 ps FWHM was the smallest system jitter value achieved. Since the system timing jitter is the convolution of all jitter sources, the timing jitter of just the SNSPD was calculated by deconvolving the jitter values of the other timing jitter sources (see equation (3.6)). To do this, the timing jitter

of the pulsed diode laser and the PPG and TCSPC card combined was measured. The timing jitter of the PPG and the TCSPC card were found by connecting the synchronised output of the PPG to the "start" trigger of the TCSPC card and connecting the output connection of the PPG to the "stop" trigger of the TCSPC card. The jitter histogram produced from this measurement gave the combined timing jitter of the PPG and the TCSPC card of 17 ps at FWHM. The timing jitter of the pulsed diode laser was measured by recording the diode laser output pulse shape on a 12 GHz photo receiver (New Focus 1554 – A 12 GHz Vis-IR photo receiver) on an oscilloscope. The FWHM of the Gaussian fitted to the peak of the pulse shape gave the timing jitter of the diode laser. The timing jitter of the pulsed diode laser was 65 ps FWHM. By taking into account the timing jitter of the PPG, TSCPC card and the pulsed diode laser, the minimum achieved timing jitter of the 50 % fill factor SNSPD was found to be 127 ps FWHM.

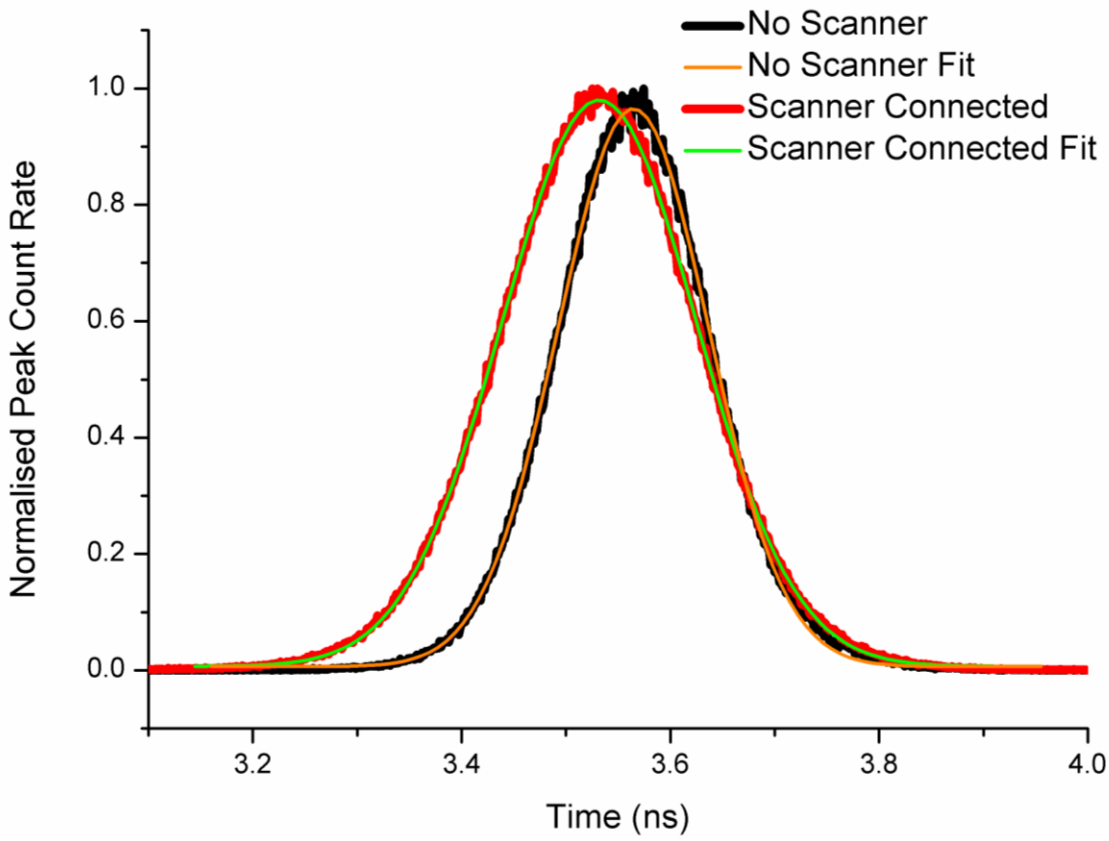

Figure 4.22 - Timing jitter histograms for the 50 % fill factor SNSPD with (red line) and without (black line) the X-Y piezoelectric scanner connected at λ = 975 nm. The green line is the fit to the histogram with the X-Y scanner connected and the orange line is the fit to the histogram without the X-Y scanner. The timing jitter for both cases with and without the X-Y scanner connected are 187 and 144 ps FWHM respectively.

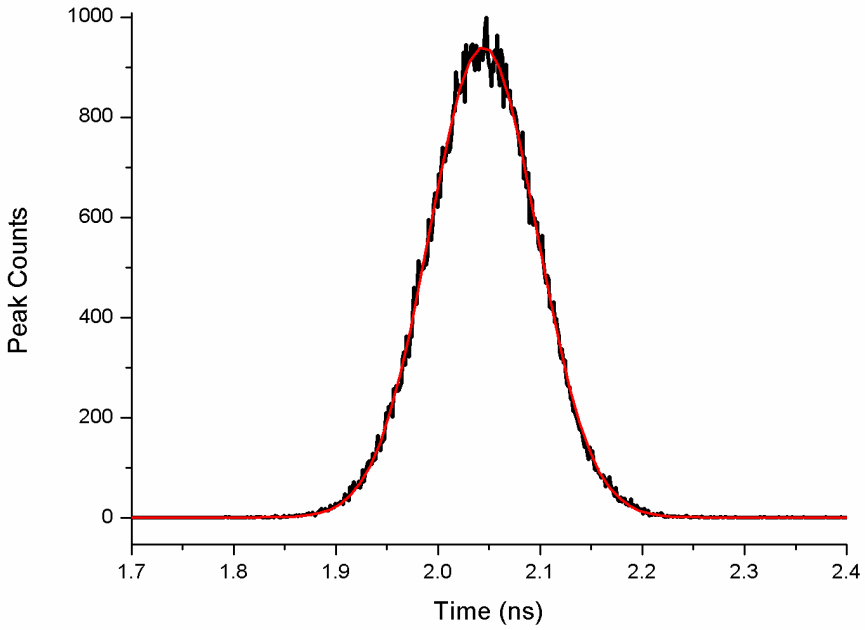

Figure 4.23 – The timing jitter histogram measured of the 10 % fill factor SNSPD without the piezoelectric X-Y scanner connected at λ = 405 nm. The black line gives the raw data, and the red line shows a Gaussian fit to the raw data. The timing jitter value of measurement system is 124 ps FWHM.

For the 10 % fill factor SNSPD a minimum system timing jitter of 124 ps FWHM was measured (see Figure 4.23). Again the system timing jitter is the combination of all jitter sources. The timing jitter of just the SNSPD was calculated by deconvolving the jitter values of the other timing jitter sources. The timing jitter of the PPG and the TCSPC card was found to be 17 ps FWHM. The timing jitter of the pulsed diode laser in the specifications was 70 ps FWHM [14]. The timing jitter of the 405 nm pulsed diode laser was not measured with the visible-IR photoreceiver as the photoreceiver can not detect light at a wavelength shorter than 450 nm.

Deconvolving the timing jitter (section 3.8.2) of the PPG, TSCPC card and of the pulsed diode laser from the complete system timing jitter measured, the minimum achieved timing jitter of the 10 % fill factor SNSPD was found to be 101 ps FWHM. This is an improvement on the jitter of the 50 % fill factor SNSPD (144 ps FWHM). The major difference between the two different SNSPD devices in this context is that the 10 % fill factor SNSPD has a higher critical current (28 µA compared to 18 µA), giving larger pulses and better timing jitter.

4.7 Conclusion

In conclusion photoresponse mapping was carried out on both a 50 % and a 10 % fill factor SNSPD using the liquid helium cooled confocal microscope configuration. The 50 % fill factor SNSPD was found through electrical tests to be partially constricted. Detection efficiency mapping showed that the constrictions contained in the device were distributed over a large area of the SNSPD. This variation in detection efficiency was from 6.6 to 23.6 % at 200 Hz dark count rate at a wavelength of 950 nm. The 50 % fill factor SNSPD had a polarisation dependence ratio of perpendicular to parallel polarised light of 0.757. The 10 % fill factor SNSPD had a maximum detection efficiency of 28.6 % at 200 Hz dark count rate using light of 950 nm wavelength. The individual wires of this SNSPD were resolved owing to the very good device uniformity. These data showed the startling fact that there was a 'missing' wire on the device that is wider than the rest of the SNSPD. This wire section was very poor at detecting photons compared to the rest of the SNSPD, due to the bias current density being smaller in this region compared to the rest of the SNSPD. The polarisation dependence ratio of perpendicularly polarised light to parallel polarised light was 0.686. Timing jitter measurements were performed yielding an overall system timing jitter of 187 ps FWHM for the 50 % fill factor SNSPD. Deconvolving the timing jitter of the electronics and the laser, provided a timing jitter value of 144 ps FWHM for the 50 % fill factor SNSPD alone. Timing jitter measurements were performed on the 10 % fill factor SNSPD, yielding an overall value of 124 ps FWHM. Deconvolving the timing jitter of the electronics and the laser a value of 101 ps FWHM for the SNSPD contribution was found. Electrical grounding issues with the piezoelectric positioners and scanner in the liquid helium confocal microscopy configuration indicate that this was not the minimum possible timing jitter of this SNSPD.

4.8 Chapter 4 References

1. V. Zwiller and G. Bjork, *Improved light extraction from emitters in high refractive index materials using solid immersion lenses.* Journal of Applied Physics, 2002. **92**(2): p. 660-665.
2. S. Moehl, H. Zhao, B.D. Don, S. Wachter, and H. Kalt, *Solid immersion lens-enhanced nano-photoluminescence: Principle and applications.* Journal of Applied Physics, 2003. **93**(10): p. 6265-6272.
3. P. A. Dalgarno, J. McFarlane, B.D. Gerardot, R.J. Warburton, K. Karrai, A. Badolato, and P.M. Petroff, *Decay dynamics of the positively charged exciton in a single charge tunable self-assembled quantum dot.* Applied Physics Letters, 2006. **89**(4): p. 043107.
4. K. A. Serrels, E. Ramsay, P.A. Dalgarno, B.D. Gerardot, J.A. O'Connor, R.H. Hadfield, R.J. Warburton, and D.T. Reid, *Solid immersion lens applications for nanophotonic devices.* Journal of Nanophotonics, 2008. **2**: p. 021854.
5. M. J. Rossow, J.M. Sasaki, M.A. Digman, and E. Gratton, *Raster image correlation spectroscopy in live cells.* Nature Protocols, 2010. **5**(11): p. 1761-1774.
6. L. M. Davis, B.K. Canfield, J.A. Germann, J.K. King, W.N. Robinson, A.D. Dukes, S.J. Rosenthal, P.C. Samson, and J.P. Wikswo, *Four-focus single-particle position determination in a confocal microscope.* Single Molecule Spectroscopy and Imaging Iii, J. Enderlein, Z.K. Gryczynski, and R. Erdmann, Editors. 2010. p. 757112.
7. R. H. Hadfield, P.A. Dalgarno, J.A. O'Connor, E. Ramsay, R.J. Warburton, E.J. Gansen, B. Baek, M.J. Stevens, R.P. Mirin, and S.W. Nam, *Submicrometer photoresponse mapping of nanowire superconducting single-photon detectors.* Applied Physics Letters, 2007. **91**(24): p. 241108.
8. J. A. O'Connor, P.A. Dalgarno, M.G. Tanner, R.J. Warburton, R.H. Hadfield, B. Baek, S.W. Nam, S. Miki, Z. Wang, and M. Sasaki, *Nano-optical studies of superconducting nanowire single photon detectors.* Quantum Communication and Quantum Networking, O. Akan, et al., Editors. 2009, Springer Berlin Heidelberg. p. 158-166.
9. A. Verevkin, J. Zhang, R. Sobolewski, A. Lipatov, O. Okunev, G. Chulkova, A. Korneev, K. Smirnov, G.N. Gol'tsman, and A. Semenov, *Detection efficiency of*

large-active-area NbN single-photon superconducting detectors in the ultraviolet to near-infrared range. Applied Physics Letters, 2002. **80**(25): p. 4687-4689.

10. B. Baek, E.J. Gansen, M.J. Stevens, R.P. Mirin, S.W. Nam, R.H. Hadfield, P.A. Dalgarno, J.A. O'Connor, E. Ramsay, and R.J. Warburton, *Investigation of local photon detection efficiency distributions in nanowire superconducting single-photon detectors.* 2008 Conference on Lasers and Electro-Optics & Quantum Electronics and Laser Science Conference, Vols 1-9, 2008: p. 3233-3234.
11. V. Anant, A.J. Kerman, E.A. Dauler, J.K.W. Yang, K.M. Rosfjord, and K.K. Berggren, *Optical properties of superconducting nanowire single-photon detectors.* Optics Express, 2008. **16**(14): p. 10750-10761.
12. J. A. Woollam, *VASE Measurements of Various Thin Films*. 7th June 2004.
13. C. M. Natarajan, M.M. Härtig, R.E. Warburton, G.S. Buller, R.H. Hadfield, B. Baek, S.W. Nam, S. Miki, M. Fujiwara, M. Sasaki, and Z. Wang, *Superconducting Nanowire Single-Photon Detectors for Quantum Communication Applications.* Quantum Communication and Quantum Networking, A. Sergienko, S. Pascazio, and P. Villoresi, Editors. 2010, Springer Berlin Heidelberg. p. 225-232.
14. *http://www.picoquant.com/datasheets/laser/LDH_Series.pdf (Date Accessed 5th May 2011).*

Chapter 5 Miniature Confocal Microscope Configuration Measurements on SNSPDs at λ = 1550 nm

5.1 Introduction

The liquid helium confocal microscopy configuration measurements described in Chapter 4 were performed at wavelengths below 1 μm. Studies at telecommunications wavelengths are not easy to perform without significant changes to the experimental setup. These changes include the optics and the alignment camera which would incur great expense. In addition to the setup changes, electrical grounding issues as seen in section 4.6 limit the ability to perform timing jitter and output pulse delay measurements. In spite of measures taken, blackbody radiation led to a device temperature above 4.2 K. This necessitated the design of a miniature confocal microscope configuration for telecommunications wavelengths which is integrated with a closed cycle refrigerator [1, 2]. The design of the miniature confocal microscope configuration is described in section 3.6.

In this Chapter two superconducting nanowire superconducting single-photon detectors (SNSPDs) of area 20 μm x 20 μm, 100 nm linewidth and 50 % fill factor (provided by NICT, Japan) were mapped (measurements were performed with Dr Michael Tanner). One device was constricted [3, 4] (see section 5.3) and the second device was highly constricted (see section 5.4). Localised information of detection efficiency (*DE*), timing jitter (Δt) and output pulse timing delay (τ) was measured. The two SNSPDs were specifically chosen to give variations in properties across the active area of the SNSPD. The properties of both SNSPDs are listed in Appendix II. To understand the variations in properties across the device, the leading edge of the output pulses were recorded and a PSPICE model was developed [5, 6] (see sections 5.3.3 and 5.4.3) (PSPICE model developed by Chandra Mouli Natarajan). By correct choice of characteristic variables (inductance, hotspot resistance, filtering due to bandwidth limitations etc) it was found that the hotspot resistance ($R_{hotspot}$) caused the variations in device properties across the active area of the SNSPD [2].

5.2 Measurement Setup

The setup described in section 3.6 (see Figure 3.24), was used to study localised areas of SNSPDs at telecommunications wavelengths. The setup was used to produce detection efficiency, timing jitter and output pulse delay maps of the SNSPD. To do this the output pulse from a femtosecond fiber laser (50 MHz, repetition rate, 2 mW output power) was split in two. One part was attenuated to the single photon level and was used to illuminate the SNSPD using the miniature confocal microscope. The other part of the pulse illuminated a "trigger" detector (either a fibre coupled SNSPD with the light attenuated down to the single photon regime, or an InGaAs fast photodiode (Thorlabs™ DET 10C/M). The output from the SNSPD was used as the "start" for the time correlated single photon counting (TCSPC) electronics (Picoquant™ Picoharp) and the "trigger" detector was used as the "stop" for the TCSPC electronics. The TCSPC electronics recorded a jitter histogram (Figure 5.1) which was fitted to provide the total number of counts, the timing jitter and the peak position.

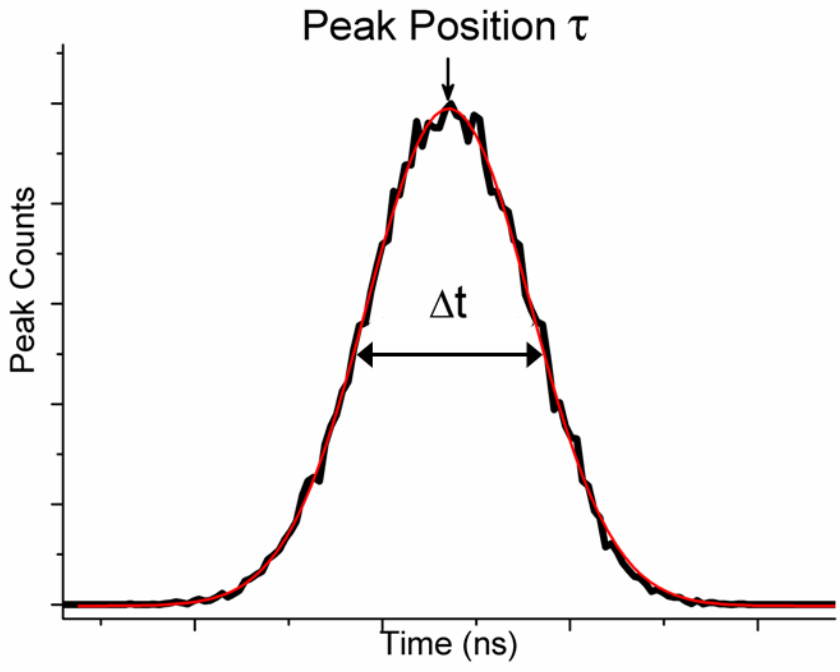

Figure 5.1 – An example of a timing jitter histogram (black line) and Gaussian fit to the histogram (red line). The peak position *τ* corresponds to the top of the histogram and the timing jitter *Δt* is defined as the full width at half maximum (FWHM) of the fitted histogram.

The resolution tests in section 3.6.2 at λ = 1550 nm used an objective lens with *NA* = 0.68, and a spot size of 1094 ± 127 nm FWHM was measured without the vibrations from the operation of the closed cycle refrigerator. This agrees with the diffraction limit of 1185 nm at FWHM predicted from the Sparrow criterion [7]. Integration into the closed cycle refrigerator led to vibrations in the miniature confocal microscope configuration, widening the focal spot to 1305 ± 363 nm FWHM. Part of this discrepancy is due to the fact that the illumination is by a Gaussian beam and not a plane wave as assumed in the Sparrow criterion.

5.3 Measurements on a Constricted Superconducting Nanowire Single-Photon Detector (SNSPD)

A constricted 50 % fill factor SNSPD with 100 nm wide wires and 200 nm pitch covering 20 µm x 20 µm area was selected to give variations in device properties across the SNSPD [2]. Electrical and optical characterisation measurements were performed to determine the extent of constriction of the SNSPD. The current-voltage (I-V) measurement (see Figure 5.2) along with inductance measurements provide a measure of how constricted the SNSPD is.

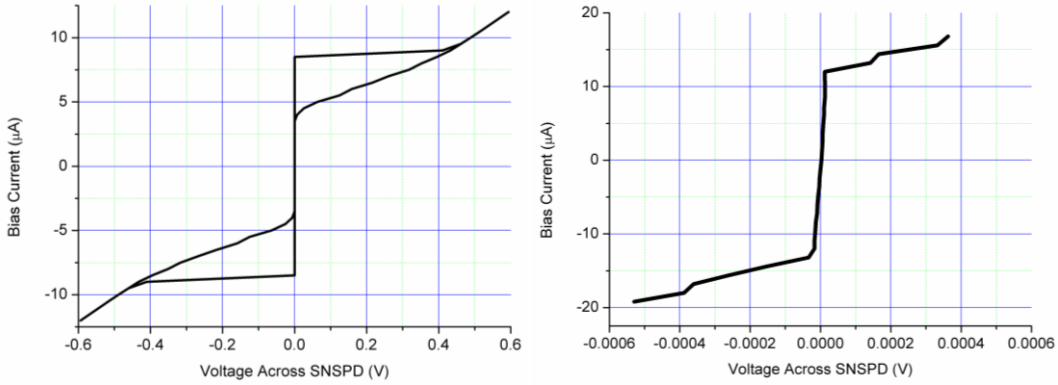

Figure 5.2 – The current – voltage (I-V) characteristic of the constricted SNSPD measured in the closed cycle refrigerator at T ~ 3 K. Left - no shunt resistor is used giving a critical current of 8 µA. Right - using a 50 Ω shunt resistor in parallel with the SNSPD, gives a critical current of 12 µA.

The I-V curve of the SNSPD with a 50 Ω shunt resistor in parallel with the SNSPD (Figure 5.2 Right) gives a critical current (I_c) value of 12 µA. The curve is not perfectly vertical while the SNSPD is in the superconducting state. This is likely due to a series resistance because the measurement was a two wire measurement.

By taking inductance (L) measurements at differing bias currents (I) up to I_c and plotting I/I_c against L/L_0 (Figure 5.3) where L_o is the inductance at zero bias current, fitting to a theoretical curve (equation (3.1)) gave the degree of constriction factor C [3, 8].

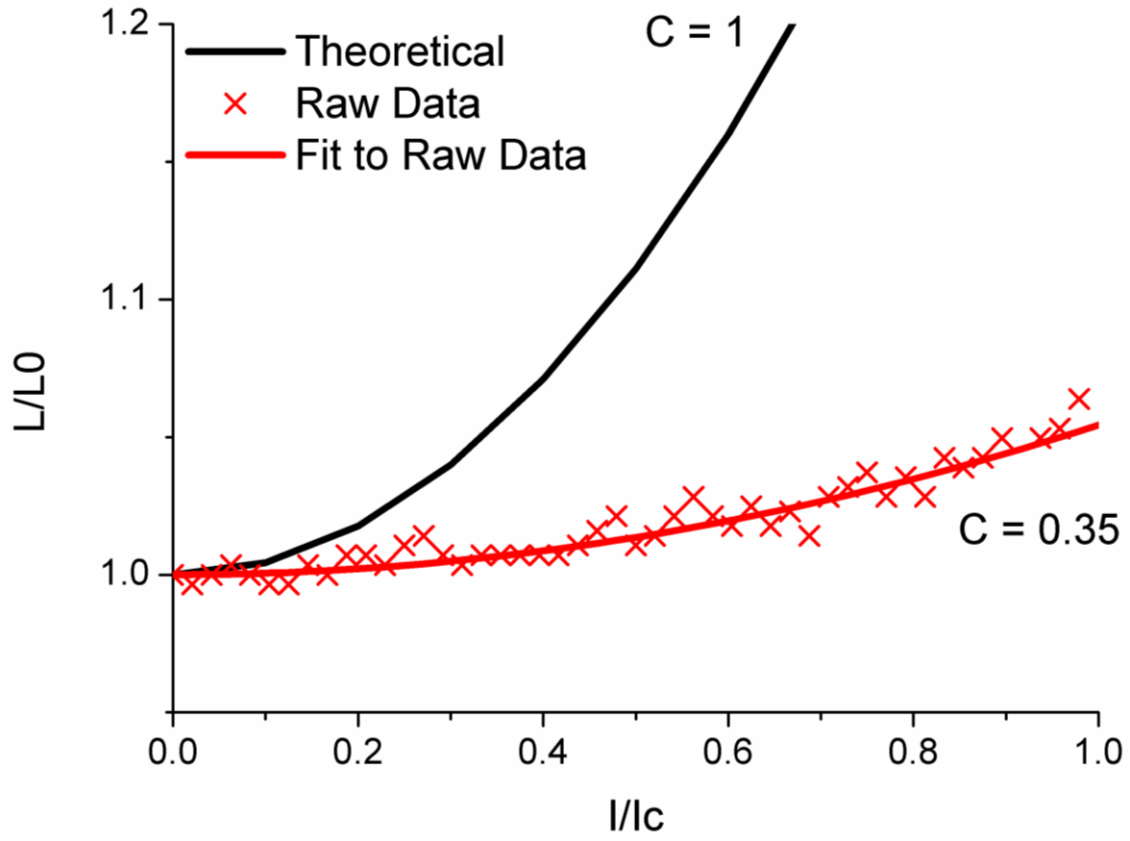

Figure 5.3 – The normalised kinetic inductance (L/L_0) and constriction factor C measurement of the constricted SNSPD. The black solid line is the theoretical curve for a perfectly uniform SNSPD. The red crosses are the measured data. The red solid line is a theoretical fit to the experimental data giving a constriction factor C value of 0.35 for the constricted SNSPD.

The upturn in inductance is shallow compared to the ideal curve, giving a C factor of 0.35. This indicates that there is either a significant constriction or a region of constrictions, which will provide a variation in the device properties across the SNSPD.

5.3.1 Detection Efficiency Mapping

The localised detection efficiency of the SNSPD was mapped and showed a broad peak in the efficiency (Figure 5.4). The broad peak is not at a single point ruling out one significant constriction in the SNSPD. The FWHM width of the photoresponse region is larger than the FWHM focal spot size, 8.9 µm compared to 1.3 µm. This indicates that the constriction predicted by the constriction factor (C = 0.35) is in fact a region of constrictions, which are constricted to a similar degree.

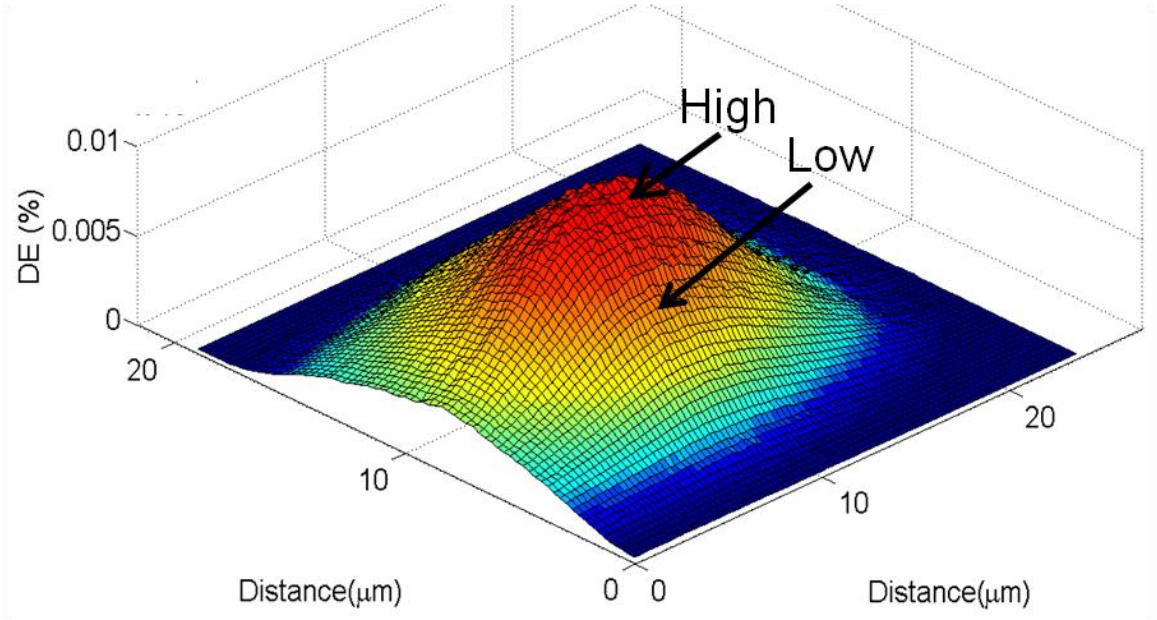

Figure 5.4 – The detection efficiency (*DE*) map of the constricted SNSPD measured in the miniature confocal microscope configuration inside a closed cycle refrigerator at T ~ 3 K. The broad peak of the response of the SNSPD is wider than the focal spot size (8.9 µm compared to 1.3 µm), indicating a region of similarly sized constrictions. The maximum *DE* achieved is 0.01 % at 1 kHz dark count rate and a wavelength of 1550 nm.

The constricted region is due to an effective narrowing in the cross sectional area of the nanowire. This may be a physical narrowing in either the thickness (~ 4 nm) or the width (100 nm) of the nanowire, which would be caused by an error in the fabrication process such as imperfect proximity effect correction leading to incorrect electron beam exposure. Also the composition of the superconducting film may have varied across the area of the film limiting the current density in some areas of the SNSPD.

The maximum *DE* achieved (both in measurements using miniature confocal microscope configuration and conventional fibre-coupling (see section 2.4.1)) was 0.01 % at 1 kHz dark count rate at a wavelength of 1550 nm.

5.3.2 Mapping of the Temporal Response of the Constricted SNSPD

As explained in section 5.2 timing jitter histograms were recorded for each position as the focal spot was scanned across the device. For each point on the device the FWHM timing jitter (Δt) and the peak position (τ) in relation to time was found by fitting a Gaussian to the histogram. For these measurements the "stop" trigger for the TCSPC electronics was a fibre-coupled SNSPD (130 ps FWHM timing jitter). To ensure a consistent and accurate Gaussian fit to the timing jitter histogram, the acquisition of data at each point was set to accumulate equal peak counts of 5000 (4 ps time bins). If this was not reached in 5 seconds the data was discarded and not used.

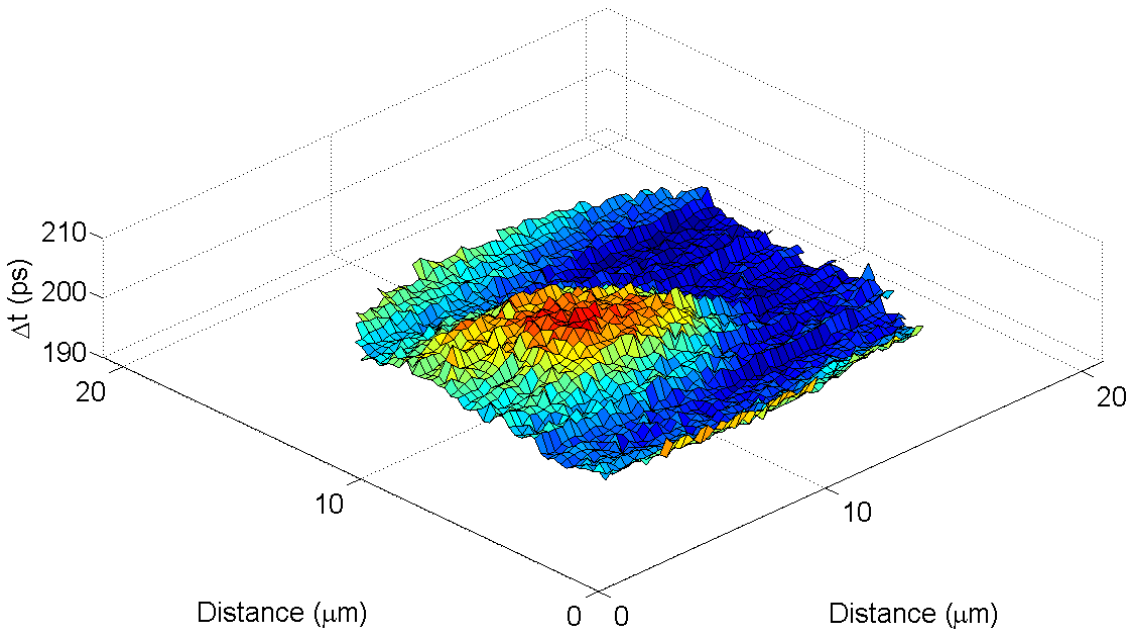

Figure 5.5 – The timing jitter map of the constricted SNSPD. The FWHM timing jitter (Δt) at each position across the SNSPD was found. The variation in Δt seen across the SNSPD is only ± 5 ps which is comparable with the time binning of the TCSPC electronics (4 ps time bins).

Figure 5.5 shows the FWHM timing jitter map for the constricted SNSPD. The variation across the SNSPD is only ± 5 ps (200 ± 5 ps) which are comparable to the time binning size used. It can be concluded that the variation in FWHM timing jitter across the SNSPD is negligible. The minimum timing jitter seen across the SNSPD is 195 ps FWHM. This is the combination of both the constricted SNSPD and the fibre-coupled SNSPD used as the "stop" trigger. This gives a timing jitter value of 145 ps FWHM for the SNSPD under test.

The Gaussian fit of the timing jitter histogram also provided the histogram peak position in time. The peak position is converted to delay (τ) with comparison to a reference time chosen such that $\tau = 0$ for the fastest responding part of the device.

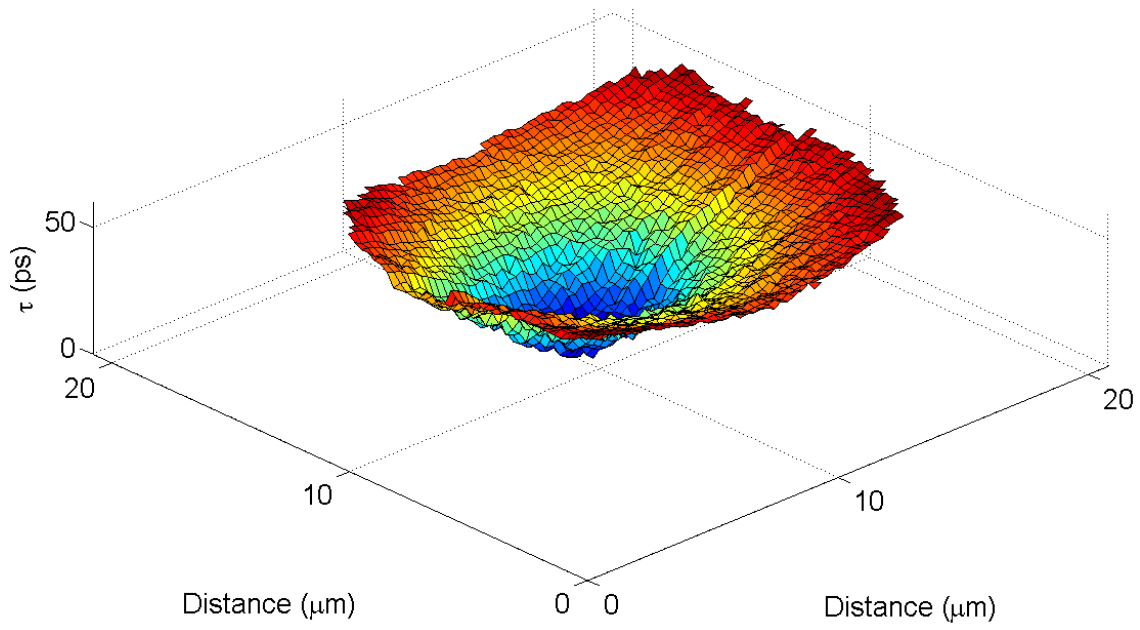

Figure 5.6 – A map of the output pulse timing delay across the constricted SNSPD. The relative output pulse timing delay (τ) at each position across the SNSPD was found from the timing jitter histograms. The variation in τ is 0 – 50 ps across the SNSPD. This variation shows that different parts of the SNSPD respond sooner than other parts of the SNSPD.

Figure 5.6 shows the relative output pulse delay (τ) across the constricted SNSPD. The variation in output pulse delay is 0 – 50 ps. It was observed that the minimum timing delay corresponds to the position of maximum detection efficiency at the centre of the device. Line-scans of *DE* and τ (Figure 5.7) through the middle of the SNSPD show

this more clearly. The line-scan profile clearly shows that as the *DE* increases from its minimum value to its maximum value, τ decreases from its maximum value to zero delay.

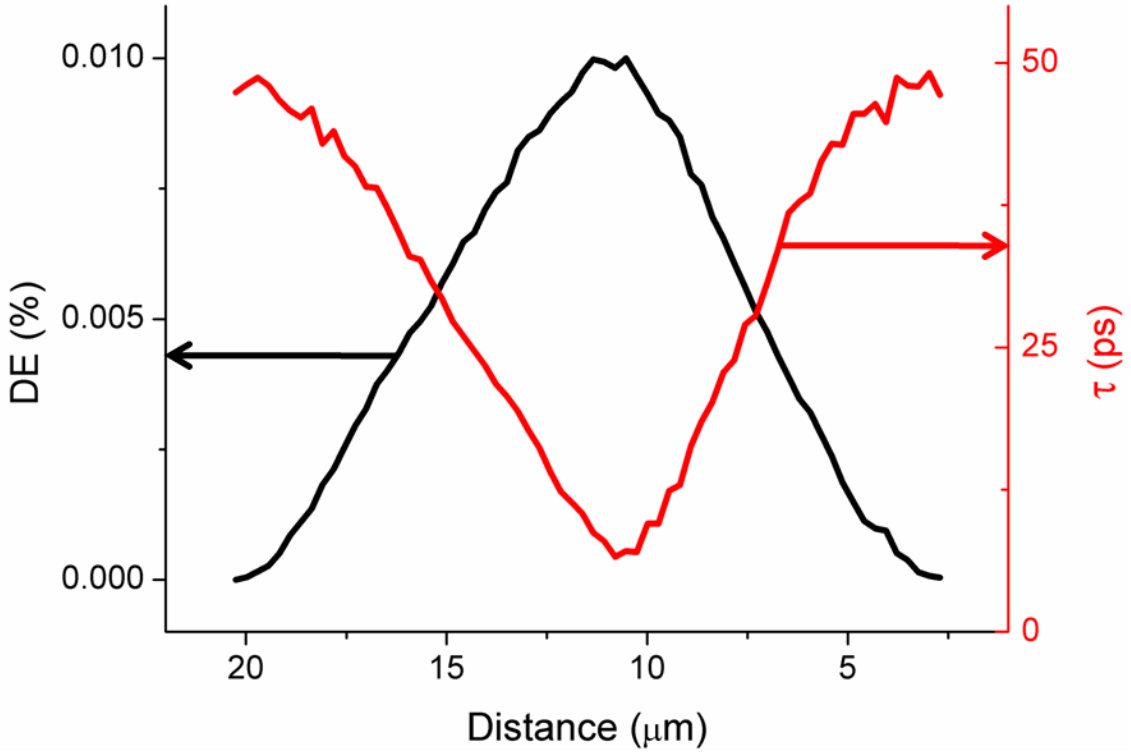

Figure 5.7 – Line scans of the detection efficiency (*DE*) (black line) and the output pulse timing delay (τ) (red line) through the middle of the constricted SNSPD. It is clear to see that as *DE* increases τ decreases so that τ is at a minimum when *DE* is at a maximum. This indicates that the regions of the SNSPD which are more constricted (high *DE* regions) respond sooner that the other regions of the SNSPD.

To confirm the observations that the spatial variation in τ was a real property of the SNSPD and not an effect of the measurement setup, both the bias current (0.01 – 50 kHz dark count rate) and photon flux (30 dB range, 0.01 – 10 photons per pulse) were varied. The same behaviour was seen over a wide photon flux range confirming that this observation is a real property of the SNSPD and not an artefact of our measurement setup.

5.3.3 Output Pulse Shapes and PSPICE Model of the Constricted SNSPD

The observed variation in τ across the SNSPD, led us to consider if these variations would correspond to a variation in the shape of the leading edge of the output pulse,

depending on which parts of the SNSPD were under illumination. Initially this appeared doubtful due to the relatively low bandwidth of the amplifier chain (the initial amplifier has a 3 dB roll off at 580 MHz). Nonetheless, precise measurements of averaged leading edge shapes of output pulses (averaged over 256 shots on an oscilloscope with 8 GHz bandwidth) from high and low *DE* regions of the SNSPD (marked on Figure 5.4) show a distinctive variation in the output pulse rise time (Figure 5.9) between these regions.

To understand the reasons behind the variation of the output pulse rise times at the high and low *DE* regions a PSPICE [9, 10] simulation was developed (by Chandra Mouli Natarajan). The PSPICE simulation (Figure 5.8) is based upon a simple but highly effective phenomenological circuit model of the SNSPD. The phenomenological model states that the time constant of the leading edge of the output pulse is given by $L/R_{hotspot}$, where L is the total inductance of the SNSPD and $R_{hotspot}$ is the resistance of the hotspot formed by the absorption of photons.

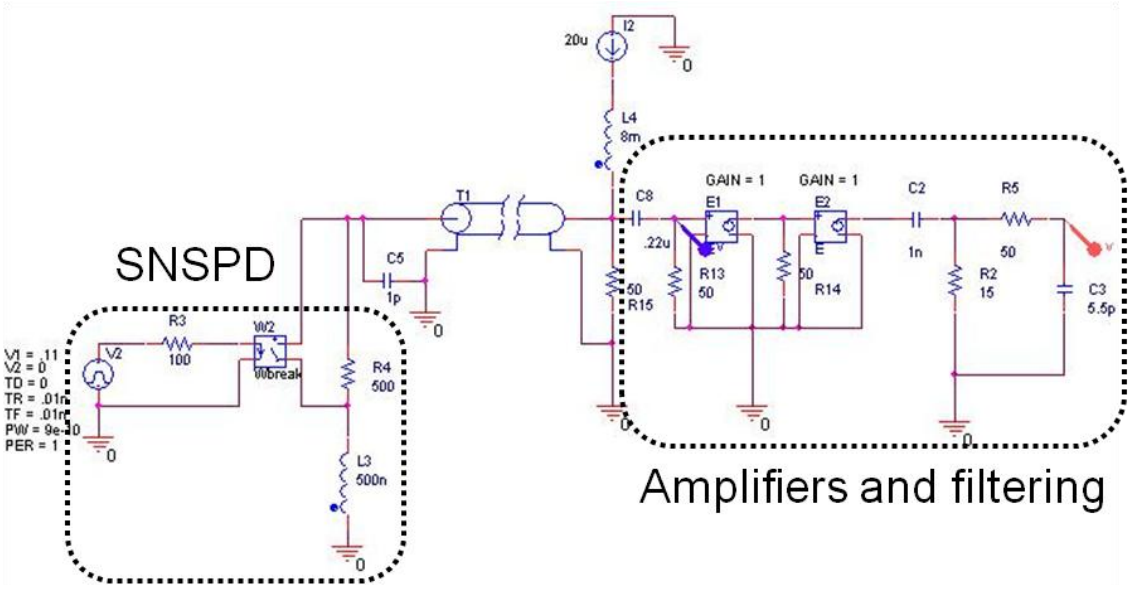

Figure 5.8 – The PSPICE model of the SNSPD taking into account the biasing circuitry, transmission lines and the output amplifiers which act as filters. The SNSPD and amplifiers are labelled. The values that are varied to simulate the output pulse are L3 which is the kinetic inductance of the whole SNSPD and R4 the hotspot resistance ($R_{hotspot}$).

The PSPICE simulation takes into account all aspects of the electrical circuit including the SNSPD, the current bias circuitry, the transmission lines, and the amplifier chain

which act as a series of low pass filters. This approach takes into account the bandwidth of the amplifiers (3 dB roll off at 580 and 1000 MHz for the initial and final amplifiers respectively). The SNSPD is simulated as a controllable voltage pulse and a time controlled switch. The switch is opened for a specified time allowing the formation of the leading edge; when the switch is closed the voltage dissipates providing the falling slope.

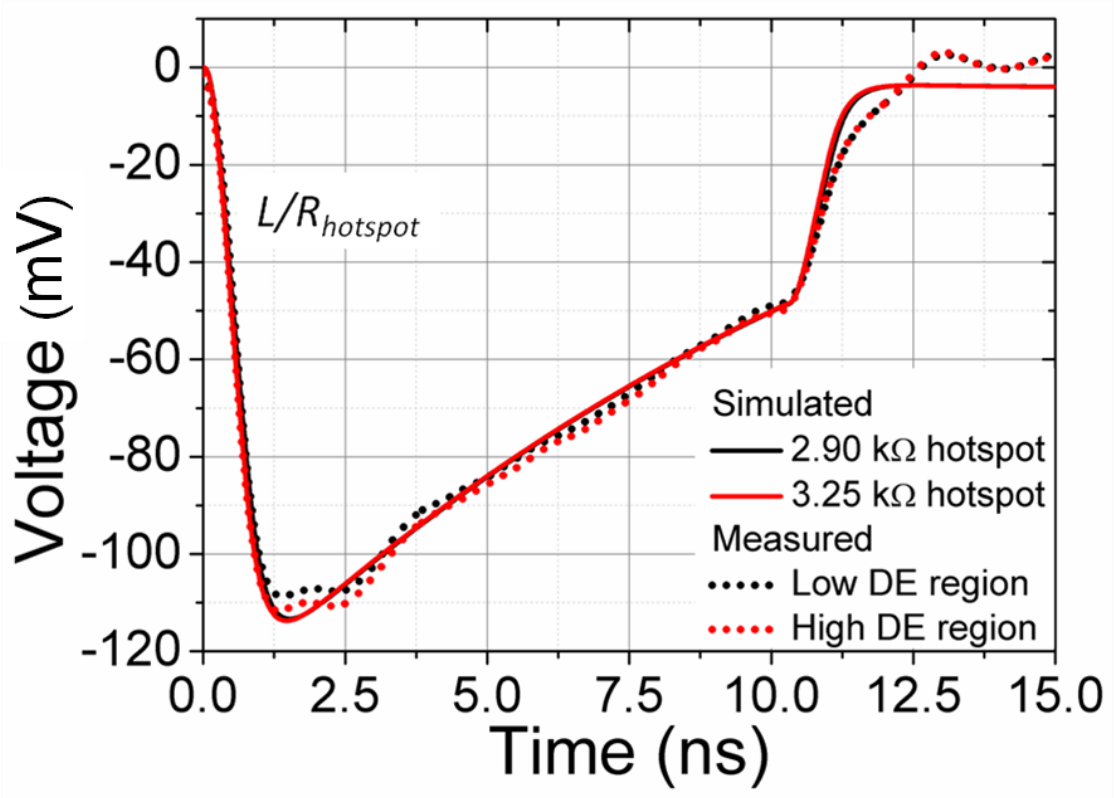

Figure 5.9 – The output pulse shapes from the constricted SNSPD at both the high (red solid line) and low (black solid line) detection efficiency (*DE*) regions (marked on Figure 5.4) of the constricted SNSPD. The PSPICE simulation of both high (red dotted line) and low (black dotted line) *DE* regions are shown. The fitted values of $R_{hotspot}$ from the simulations are 3.25 kΩ and 2.90 kΩ for the high and low *DE* regions respectively.

Figure 5.9 shows the output pulse shapes from both the high and low *DE* regions (solid lines). The dashed lines are the fit to the PSPICE simulation. As stated above, the expected variation is apparent in the leading edges of the output pulse shapes. The leading edge slope is defined by $L/R_{hotspot}$. The sudden change in slope at time ~ 10 ns is caused by reflections from the T piece used to mount the DC 50 Ω shunt resistor in parallel with the SNSPD. The shunt resistor was used to prevent the SNSPD latching into the resistive state. It does this by providing a path of lower resistance for the bias

current when the SNSPD is resistive (50 Ω compared to kΩs). This allows the SNSPD to recover into the superconducting state.

By only looking at the leading edge (0 – 1.4 ns range see Figure 5.11) it was possible to see the variation in the output pulse shapes. The discrepancies between the PSPICE simulation and the measured output pulse shapes arise due to the fact that a fixed value of $R_{hotspot}$ was assumed in the model. The model did not take into account any possible evolution of $R_{hotspot}$ with time [11].

Reference [11] describes a detailed thermal and electrical model of SNSPDs. The model allows the growth of a resistive hotspot in a SNSPD to be simulated. This model shows that the resistance of the SNSPD grows from zero to a maximum value in the normal state. The resistance then drops back to zero as the SNSPD recovers into the superconducting state (Figure 5.10). This model indicates that the resistive hotspot evolves along the length of the nanowire up to a maximum value driven by Joule heating from the bias current.

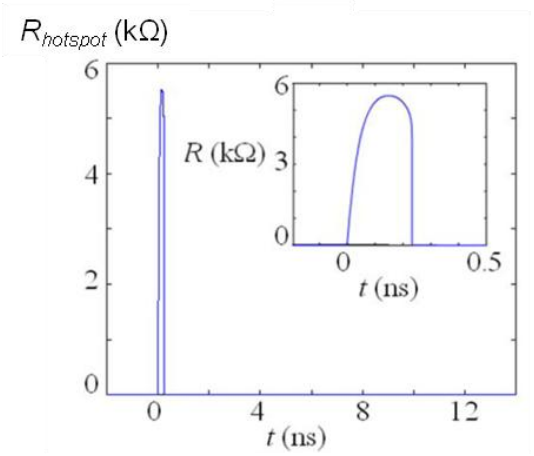

Figure 5.10 – Simulation of hotspot resistance ($R_{hotspot}$) versus time reported by *Yang et al.*[11]. The inset shows a gradual increase of resistance at t = 0 and a sharp drop in resistance as the SNSPD recovers into the superconducting state at t = 230 ps.

The model predicts $R_{hotspot}$ values of 3.25 and 2.90 kΩ for the high and low *DE* regions respectively. This is only a difference of 12 % in $R_{hotspot}$. The PSPICE simulation predicts that τ between the high and low *DE* regions should be ~ 30 ps. The timing jitter histograms taken at the high and low *DE* regions in section 5.3.2 (Figure 5.12) show a timing delay between the peaks of the histograms to be ~ 30 ps. Our PSPICE simulation confirms that τ is caused by a variation in $R_{hotspot}$ across the SNSPD.

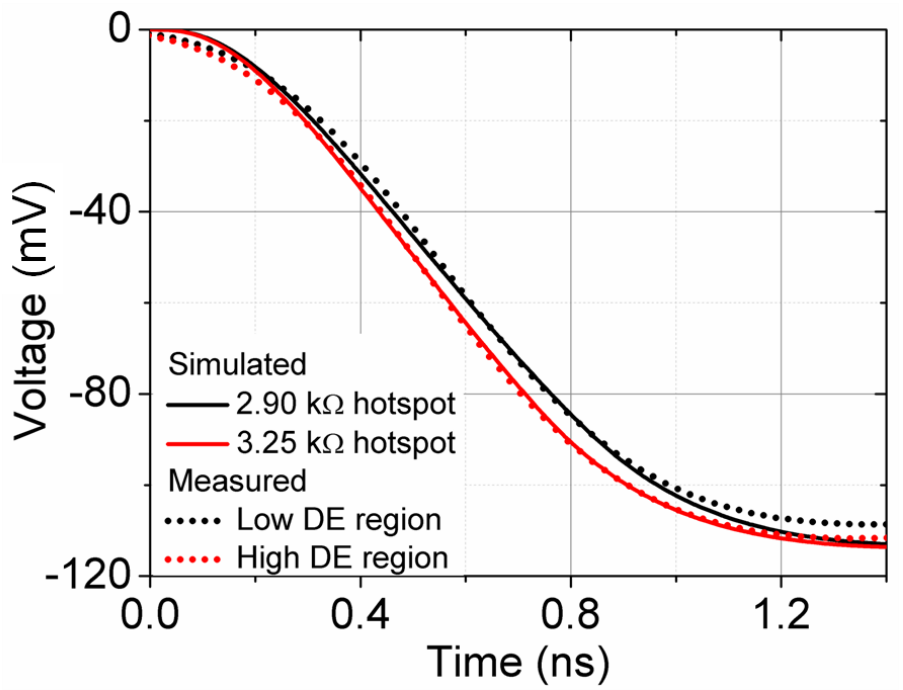

Figure 5.11 – The leading edges of the output pulse shapes at the high and low detection efficiency regions (*DE*) of the constricted SNSPD. The PSPICE simulation fits to the leading edges of the output pulse shapes reasonably well. However at the beginning and end of the leading edges the simulation does not fully match the output pulse shape. This is because the PSPICE model assumes a fixed value of $R_{hotspot}$ and not an evolving $R_{hotspot}$, which causes the discrepancies between the fit and the experimental pulse shapes.

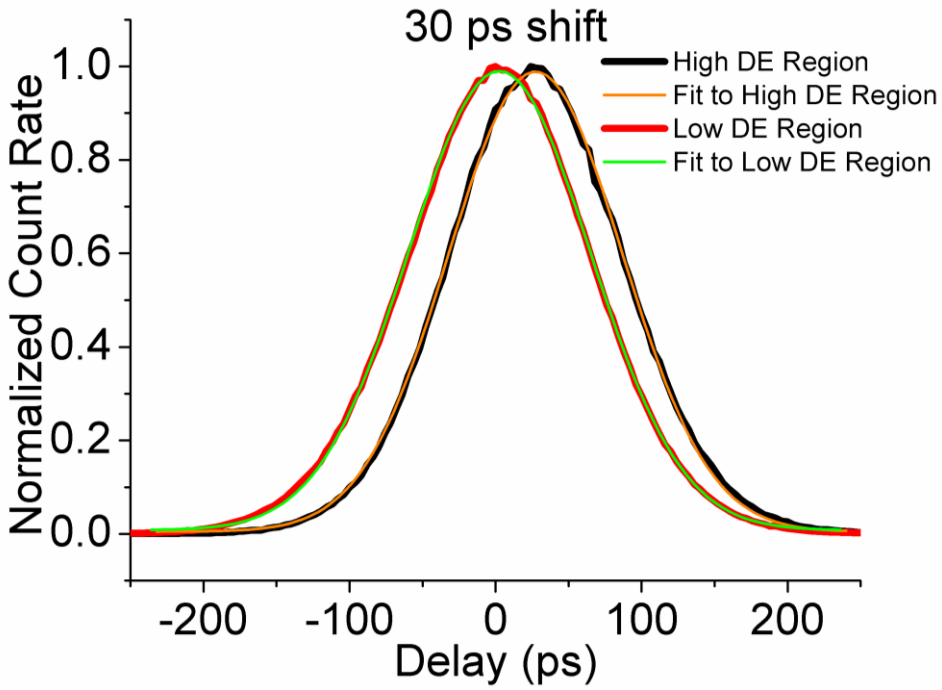

Figure 5.12 - Normalised timing jitter histograms at both high (black line) and low (red line) *DE* regions of the constricted SNSPD. The fits to both the high (orange line) and low (green line) *DE* region histograms are shown. The timing jitter (Δt) values of the high and low *DE* regions are 140 and 146 ps FWHM respectively. The fast peak occurs at $\tau = 0$ and the peak corresponding to the slower part of the device occurs at $\tau = 30$ ps.

5.4 Measurements on the Highly Constricted Superconducting Nanowire Single-Photon Detector (SNSPD)

In order to see if the variation in $R_{hotspot}$ was an actual effect and not just particular to the SNSPD chosen in section 5.3, a second more highly constricted 50 % fill factor (100 nm wide wires, 200 nm pitch) SNSPD covering 20 µm x 20 µm was chosen to give even more variation in device properties across the SNSPD. Again electrical and optical characterisation measurements were performed to determine the extent of the constriction of the SNSPD. The current-voltage (I-V) measurement (see Figure 5.13) along with inductance measurements provided a measure of how constricted the SNSPD is (see Figure 5.14).

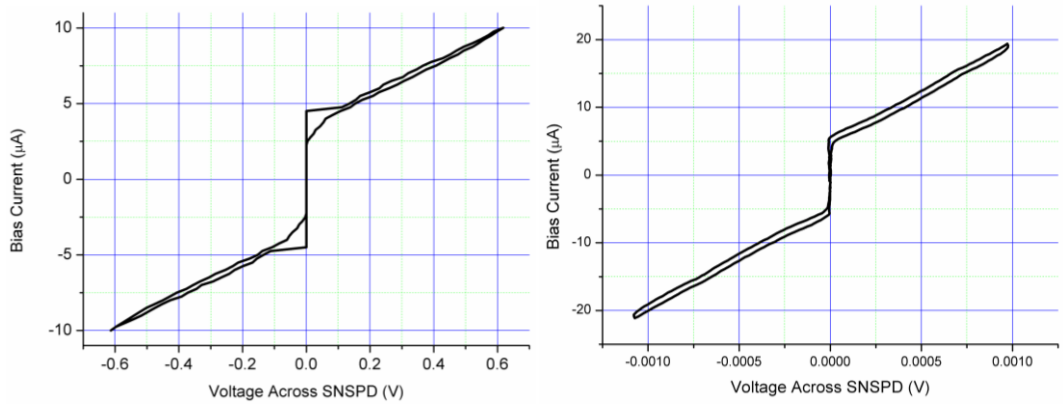

Figure 5.13 – The current – voltage (I-V) characteristic of the highly constricted SNSPD measured in the miniature confocal microscope configuration inside a closed cycle refrigerator at T ~ 3 K. Left - no shunt resistor used giving a critical current of 4.5 µA. Right - using a 50 Ω shunt resistor in parallel with the SNSPD, giving a critical current of 6.5 µA.

The I-V curve of the SNSPD with a 50 Ω shunt resistor gives a critical current (I_c) value of 6.5 µA. The degree of constriction factor C was measured as detailed in section 5.3.

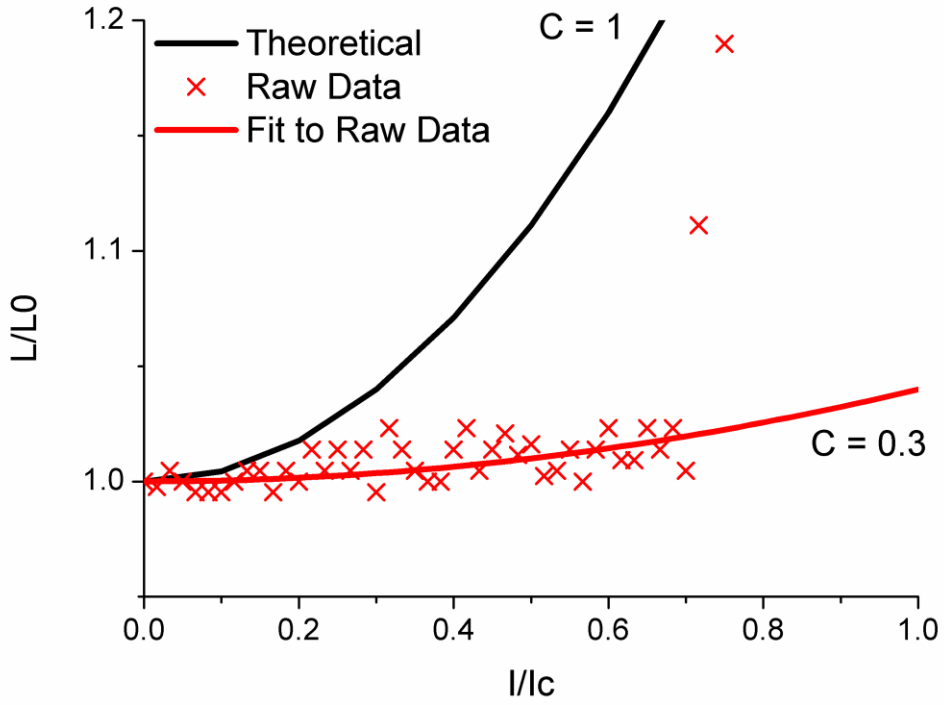

Figure 5.14 – The normalised kinetic inductance (L/L_0) and constriction factor *C* measurement of the highly constricted SNSPD. The black solid line is the theoretical curve for a perfectly uniform SNSPD. The red crosses are the measured data. The red solid line is the theoretical fit to the experimental data giving a constriction factor *C* value of 0.3 for the highly constricted SNSPD.

The upturn in inductance is even shallower compared to the theoretical curve than the SNSPD in section 5.3, giving a *C* factor of 0.3. This indicates that there is either a significant constriction or a region of constrictions, which are greater compared to the SNSPD in section 5.3 and will provide a greater variation in the device properties across the SNSPD.

5.4.1 Detection Efficiency Mapping

Again the localised *DE* of the highly constricted SNSPD was mapped (Figure 5.15). This time the *DE* map showed two peaks. The two peaks have differing heights. This indicates that the device (with an overall constriction factor $C = 0.3$) has in fact two regions of constrictions, which are constricted to differing extents. This provides good variation in timing jitter and output pulse delay across the SNSPD.

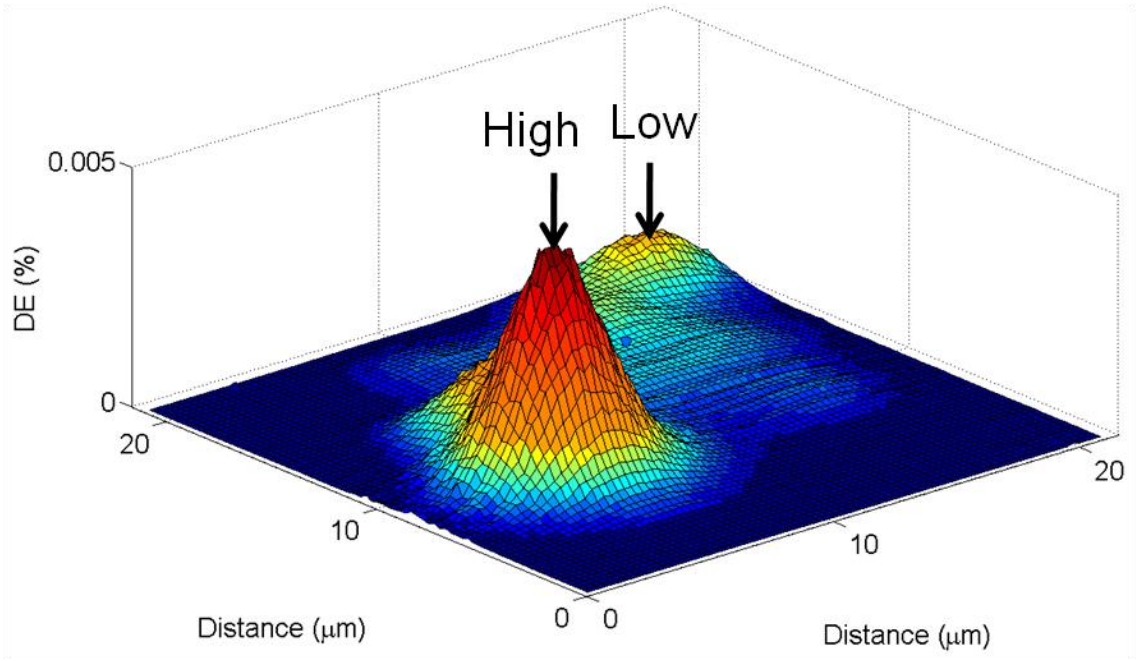

Figure 5.15 – The detection efficiency (*DE*) map of the highly constricted SNSPD at λ = 1550 nm in the miniature confocal microscope configuration inside a closed cycle refrigerator at T ~ 3 K. The FWHM resolution of the microscope is 1300 nm. The two peaks in the response of the SNSPD indicate two regions of constrictions. The differences in heights of the peaks also indicate that the regions are constricted to differing degrees. The maximum *DE* achieved is 0.005 % at 1 kHz DCR and a wavelength of 1550 nm.

As the constricted regions are not in the middle of the device, the effective narrowing of the nanowire causing the constrictions are less likely to be due to incorrect proximity effect correction during electron beam patterning. This is because with over exposure of the electron beam narrowing the nanowires is to be expected more in the middle of the SNSPD. Another possible reason for this pattern of constrictions is defects or thickness variations in the superconducting film itself. The maximum detection efficiency was 0.005 % at 1 kHz dark count rate at a wavelength of 1550 nm.

5.4.2 Mapping of the Temporal Response of the Highly Constricted SNSPD

Again as in section 5.3.2 timing jitter histograms were recorded for each position on the highly constricted device. The FWHM timing jitter (Δt) and the peak position (τ) in relation to time were found by fitting a Gaussian to the timing jitter histogram recorded at each point as illustrated in Figure 5.1. These measurements used a fibre-coupled SNSPD (130 ps FWHM timing jitter) as the "stop" trigger for the TCSPC electronics.

The acquisition of data at each position was set to accumulate peak counts of 5000 (4 ps time bins). If 5000 peak counts were not reached in 5 seconds the data was discarded and not used (as in section 5.3.2). This was to ensure sufficient data accumulation for a consistent Gaussian fit.

Figure 5.16 shows the timing jitter map for the highly constricted SNSPD. The variation in Δt across the SNSPD is now significant (350 – 600 ps at FWHM) compared to the constricted SNSPD. The low critical current of the device (6.5 μA) leads to increased timing jitter. The timing jitter map has two interfaces or edges which separate three regions of significantly different jitter. What is happening in these regions is that the focal spot is illuminating several regions with a sizeable difference in the local timing delay. This means that the points of highest timing jitter are taking contributions from multiple regions with varying speeds increasing the uncertainty between the absorption of a photon and the generation of an output voltage pulse. The minimum timing jitter seen across the SNSPD was 350 ps FWHM; this is the combination of both the constricted SNSPD and the fibre-coupled SNSPD used as the "stop" trigger. Correcting for the contribution of the trigger detector gave a minimum timing jitter value of 325 ps FWHM for the highly constricted SNSPD under test.

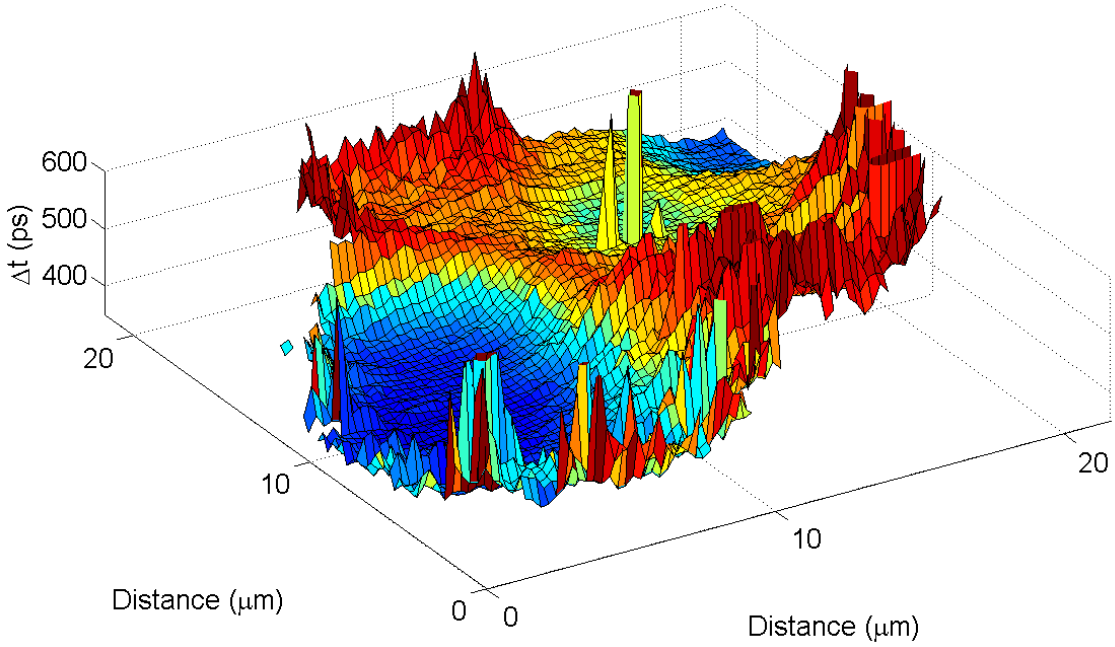

Figure 5.16 – The timing jitter map of the highly constricted SNSPD. The timing jitter (Δt) at each position across the SNSPD was found. The variation in Δt seen across the SNSPD is ~ 350 – 600 ps. The two interfaces which have higher Δt values suggest that at these positions the focal spot is illuminating regions with significant variation in Δt, resulting in increased overall Δt.

The Gaussian fit of the timing jitter histogram provided the histogram peak position. It is useful to consider the absolute variation in the peak positions as in section 5.3.2. The output pulse delay (τ) is calculated as before.

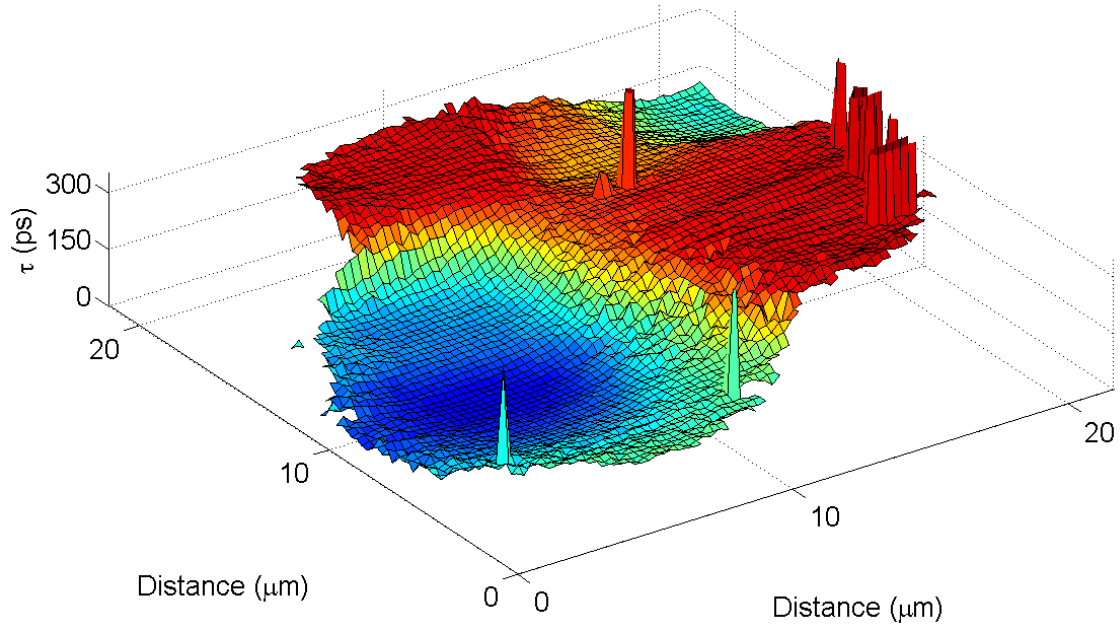

Figure 5.17 – The output pulse timing delay (τ) map of the highly constricted SNSPD. The relative output pulse timing delay (τ) at each position across the SNSPD was found from the timing jitter histograms. The fastest responding part of the device sets τ = 0. The variation in τ is 0 – 300 ps across the SNSPD. This variation shows that certain parts of the SNSPD respond sooner than other parts. By comparison with Figure 5.16 we see that illuminating regions of the SNSPD that respond at significantly varying delay times increases the timing jitter at these regions.

Figure 5.17 shows the output pulse delay (τ) across the highly constricted SNSPD. The variation in τ is 0 – 300 ps. As seen in the constricted SNSPD the minimum τ for the highly constricted SNSPD corresponds to the position of maximum *DE*. Line scans of *DE*, Δt and τ (Figure 5.18) between the high and low points (see Figure 5.15) of the SNSPD show this more clearly. The line scan profile clearly shows that as the *DE* increases from its minimum value to its maximum value, τ decreases from its maximum value to zero relative delay just like the constricted SNSPD.

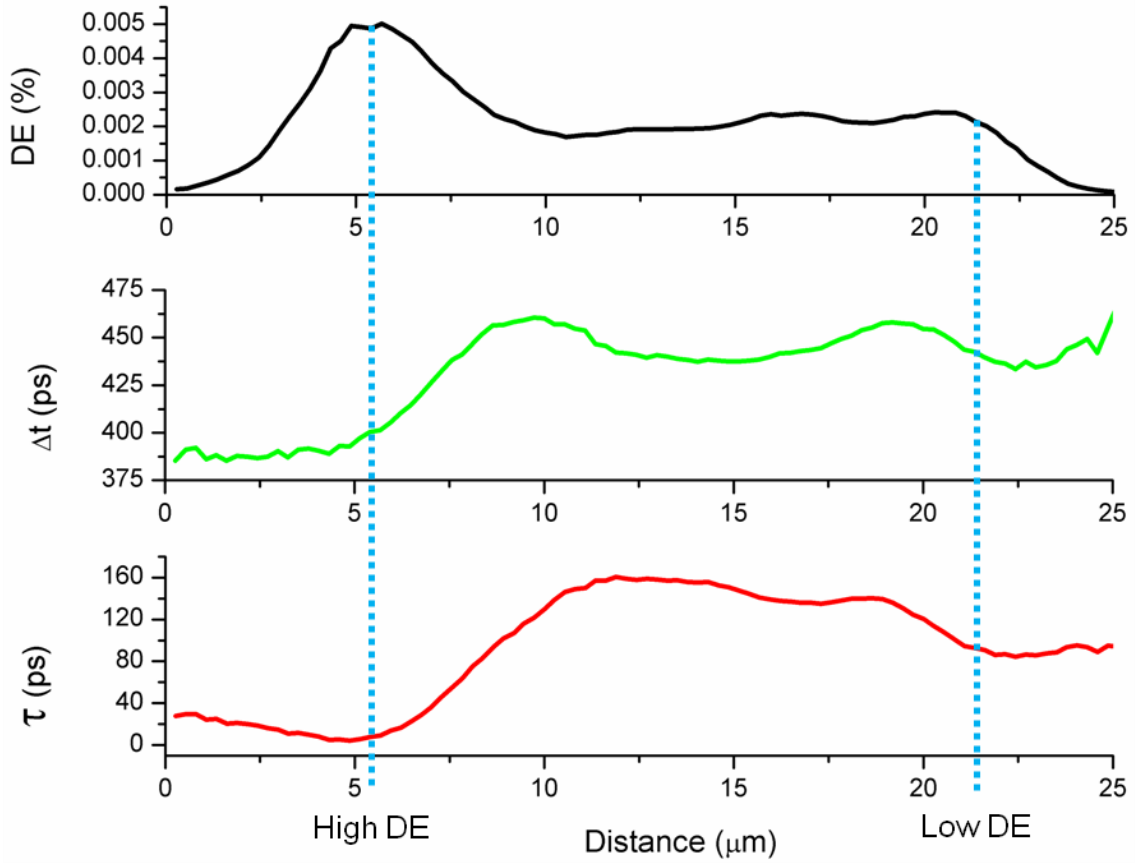

Figure 5.18 – Single line scans of detection efficiency (*DE*) (black line), FWHM timing jitter (*Δt*) (green line) and output pulse timing delay (*τ*) (red line) through the middle of the highly constricted SNSPD. As *DE* increases *τ* decreases so that *τ* is at a minimum when DE is at a maximum. This measurement also suggests that the regions of the SNSPD which are more constricted (the highest DE regions seen in Figure 5.15) respond sooner that the other regions of the SNSPD.

Figure 5.18 also clearly shows that *τ* plot inversely matches the *DE* plot. This confirms that this is a genuine effect in non-uniform SNSPDs and not just the constricted SNSPD measured in section 5.3.

Furthermore the line scans of *Δt* and *τ* between points of high and low *DE* show that the peak timing jitter values correspond to the locations of highest variation (10 and 18 μm) of *τ*. The variation in *τ* shows the variation in the speed at which the SNSPD responds. This indicates that at the positions of maximum *Δt* the focal spot simultaneously illuminates regions of the SNSPD which respond at differing speeds. This observation is a powerful insight into the origins and causes of timing jitter in SNSPDs.

5.4.3 Output Pulse Shapes and PSPICE Model of the Highly Constricted SNSPD

Again as in section 5.3.3, by looking closely at the leading edge (0 – 1 ns range) it is possible to see the variation in the output pulse shapes (see Figure 5.19). The discrepancies between the PSPICE simulation and the output pulse shapes was due to using a fixed value of $R_{hotspot}$ and not taking into account the evolution of $R_{hotspot}$ over time. What is clear from examining the pulse shape leading edges at the beginning and the end of the pulse shape was that the PSPICE simulation does not perfectly match the experimental data. This discrepancy highlights the limitations of the PSPICE model, which does not take into account the evolution of the resistive hotspot over time.

The electrical and thermal evolution of the hotspot has been modelled by *Yang et al* [11]. It was shown that the incident photon hits the nanowire forming a resistive hotspot. This hotspot grows both to the edge of the nanowire and along the length of the nanowire due to Joule heating driven by the bias current. This sequence of events trigger an output voltage pulse. The growth of the hotspot impedes the bias current and allows the temperature of the nanowire to decrease. The nanowire switches back into the superconducting state and the bias current recovers (limited by the inductance of the nanowire) and the SNSPD is ready to detect another incident photon.

The PSPICE model predicts $R_{hotspot}$ values of 2.30 and 2.20 kΩ for the high and low *DE* regions respectively. This is only a difference of 4 % in $R_{hotspot}$. The timing jitter histograms at high and low *DE* regions in section 5.4.2 (Figure 5.20) show a timing delay difference between the peaks of the histograms to be 85 ps.

The PSPICE model does not take into account the evolution of $R_{hotspot}$ over time. This explains the variation between the model and experimental pulse shapes at the beginning and end of the leading edge. This effect is also observed in the PSPICE fit to the pulse shapes of the constricted SNSPD (section 5.3.3). This is because the thermal model presented by *Yang et al* [11] shows that $R_{hotspot}$ grows rapidly but dissipates more slowly (~100 ps) without plateauing as a steady $R_{hotspot}$ value.

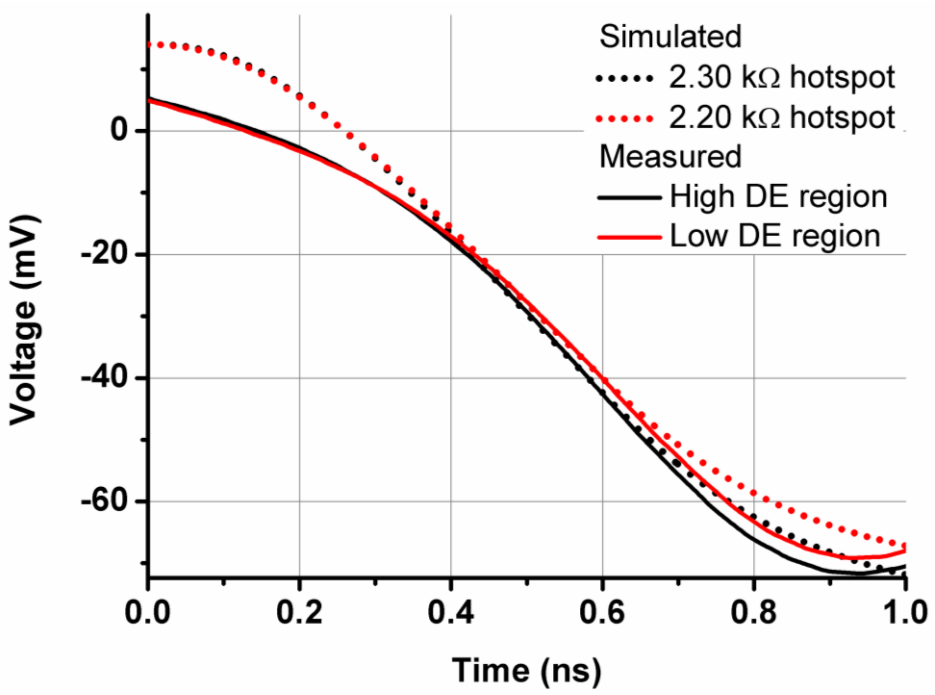

Figure 5.19 – The leading edges of the output pulse shapes at the high and low detection efficiency (*DE*) regions of the highly constricted SNSPD (see Figure 5.15). The PSPICE simulation fit to the leading edges of the output pulse shapes does not follow the measured data as well as before (Figure 5.11). This is because the PSPICE model assumes a fixed value of $R_{hotspot}$ and not an evolving $R_{hotspot}$, which causes the discrepancies between the fit and the experimental pulse shapes. This shows the limitations of the PSPICE model and that the fitted values of 2.30 and 2.20 kΩ for the high and low detection efficiency regions respectively may be inexact.

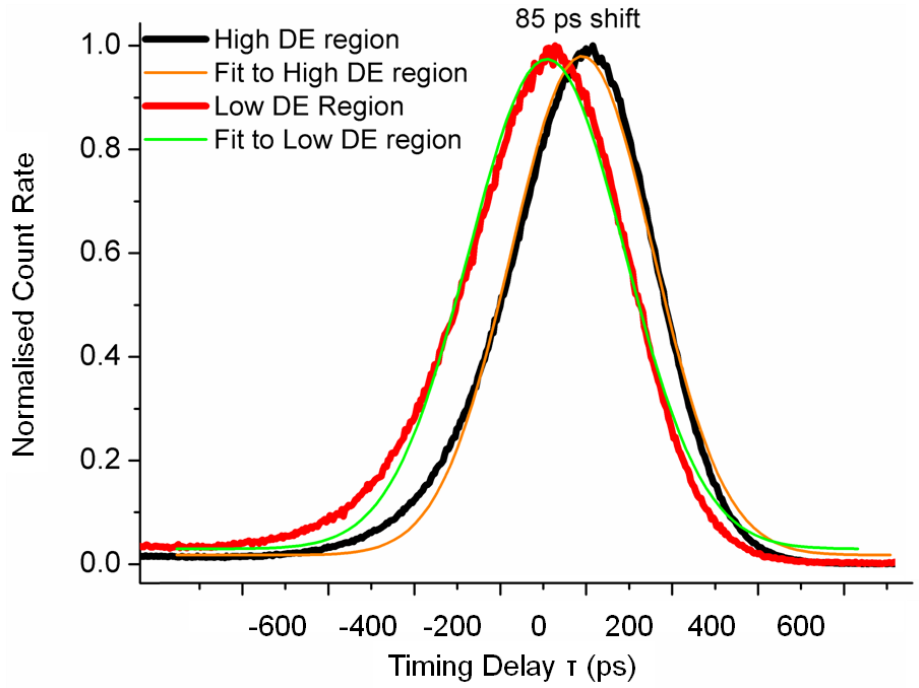

Figure 5.20 – Normalised timing jitter histograms at both high (black line) and low (red line) DE regions of the highly constricted SNSPD. The fits to both the high (orange line) and low (green line) DE region histograms are shown. The timing jitter (Δt) values of the high and low DE regions are 389 and 427 ps FWHM respectively. The faster peak occurs at $\tau = 0$ and the slower peak occurs at $\tau = 85$ ps.

5.5 Conclusion

Two constricted 50 % fill factor SNSPDs were spatially mapped to provide localised information on detection efficiency (*DE*), timing jitter (Δt) and output pulse timing delay (τ). The first SNSPD device has a *C* value of 0.35 and is referred to as the "constricted" device. The second SNSPD device had a *C* value of 0.3 is referred to as the "highly constricted" device. At λ = 1550 nm the constricted SNSPD showed little variation in Δt across the SNSPD (Δt variation was only ± the time bin size of the TCSPC electronics). The variation in τ (0 – 50 ps) was shown to inversely follow the localised *DE* such that the minimum τ occurs at the position of maximum detection efficiency. At the position of maximum *DE* (0.01 % at 1 kHz dark count rate and at 1550 nm wavelength), the SNSPD was more constricted compared to the rest of the device, and thus has a higher current density. This shows that at a constriction the SNSPD responds sooner to the absorption of a photon.

The highly constricted SNSPD is less homogeneous and showed a wider variation in behaviour. However the main variations in τ and *DE* can be understood in terms of local variations in $R_{hotspot}$. This was shown more clearly in this SNSPD as the variation in τ was larger (0 – 300 ps) and the *DE* profile contained two peaks of varying heights with a maximum *DE* of 0.005 % at l kHz dark count rate and at 1550 nm wavelength. For this device the Δt map showed a large variation (350 – 600 ps FWHM) across the SNSPD. The regions of highest Δt are those where multiple regions with varying τ are illuminated by the focal spot. So Δt at these regions has contributions from regions which respond with differing speeds, increasing Δt.

To understand the variation in τ more clearly, output pulse shapes averaged over 256 shots were taken at high and low *DE* regions for both SNSPDs and fitted to a PSPICE model. This comparison showed that the variation in τ at each position was governed by the value of $R_{hotspot}$. For the constricted SNSPD the values of $R_{hotspot}$ were 3.25 and 2.90 kΩ for the high and low detection efficiency regions respectively. The PSPICE model did not exactly match the pulse shapes due to the assumption of a fixed $R_{hotspot}$, which did not take into account any evolution of $R_{hotspot}$ over time. For the highly constricted SNSPD, the PSPICE model fit gave a poorer match to the pulse shape. This

indicates that in the highly constricted SNSPD the $R_{hotspot}$ evolution must play a significant role.

The variations in Δt, τ and $R_{hotspot}$ observed here provide an important new insight into understanding the device physics of SNSPDs. This study the indicates that for minimal timing jitter values, the SNSPD must to be uniform and not constricted.

This effect may be able to allow photon energy or photon number information to be extracted from $R_{hotspot}$ variations. Next generation device designs have the potential to exploit this effect in spectroscopy applications, if adequate timing resolution can be achieved. Applications such as imaging may also be possible (see section 6.2), if spatial variations in τ without a reduction in *DE* can be engineered.

5.6 Chapter 5 References

1. A. Hogele, S. Seidl, M. Kroner, K. Karrai, C. Schulhauser, O. Sqalli, J. Scrimgeour, and R.J. Warburton, *Fiber-based confocal microscope for cryogenic spectroscopy.* Review of Scientific Instruments, 2008. **79**(2): p. 023709.
2. J. A. O'Connor, M.G. Tanner, C.M. Natarajan, G.S. Buller, R.J. Warburton, S. Miki, Z. Wang, S.W. Nam, and R.H. Hadfield, *Spatial dependence of output pulse delay in a niobium nitride nanowire superconducting single-photon detector.* Applied Physics Letters, 2011. **98**(20): p. 201116-3.
3. A. J. Kerman, E.A. Dauler, J.K.W. Yang, K.M. Rosfjord, V. Anant, K.K. Berggren, G.N. Gol'tsman, and B.M. Voronov, *Constriction-limited detection efficiency of superconducting nanowire single-photon detectors.* Applied Physics Letters, 2007. **90**(10): p. 101110.
4. R. H. Hadfield, *Single-photon detectors for optical quantum information applications.* Nature Photonics, 2009. **3**(12): p. 696-705.
5. A. J. Kerman, E.A. Dauler, W.E. Keicher, J.K.W. Yang, K.K. Berggren, G. Gol'tsman, and B. Voronov, *Kinetic-inductance-limited reset time of superconducting nanowire photon counters.* Applied Physics Letters, 2006. **88**(11): p. 111116.
6. R. H. Hadfield, A.J. Miller, S.W. Nam, R.L. Kautz, and R.E. Schwall, *Low-frequency phase locking in high-inductance superconducting nanowires.* Applied Physics Letters, 2005. **87**(20): p. 203505.
7. C. M. Sparrow, *On spectroscopic resolving power.* The Astrophysical Journal, 1916. **44**: p. 76.
8. M. G. Tanner, C.M. Natarajan, V.K. Pottapenjara, J.A. O'Connor, R.J. Warburton, R.H. Hadfield, B. Baek, S. Nam, S.N. Dorenbos, E.B. Urena, T. Zijlstra, T.M. Klapwijk, and V. Zwiller, *Enhanced telecom wavelength single-photon detection with NbTiN superconducting nanowires on oxidized silicon.* Applied Physics Letters, 2010. **96**(22): p. 221109.
9. L. Nagel and R. Rohrer, *Computer analysis of nonlinear circuits, excluding radiation (CANCER).* IEEE Journal of Solid-State Circuits, 1971. **6**(4): p. 166-182.

10. L. W. Nagel and D.O. Pederson, *SPICE (Simulation Program with Integrated Circuit Emphasis), Memorandum No. ERL-M382.* University of California, Berkeley, 1973.
11. J. K. W. Yang, A.J. Kerman, E.A. Dauler, V. Anant, K.M. Rosfjord, and K.K. Berggren, *Modeling the electrical and thermal response of superconducting nanowire single-photon detectors.* IEEE Transactions on Applied Superconductivity, 2007. **17**(2): p. 581-585.

Chapter 6 Conclusion and Outlook

6.1 Summary of Thesis Work

The work in this thesis has demonstrated two new and robust methods for studying localized areas of superconducting nanowire single-photon detectors (SNSPD) from visible to telecommunication wavelengths (see Chapter 3). Firstly a liquid helium (LiHe) based confocal microscopy configuration was used for studies at visible and near infrared wavelengths. The achievable optical resolution of this system can be approximated by the Sparrow criterion (see equation (2.9)) [1]. The second method utilised a fibre based miniature confocal microscope configuration [2] which was designed, tested [3] and integrated into a Gifford-McMahon (GM) closed-cycle refrigerator [4]. This system provided the advantage of not requiring liquid cryogen handling, which would otherwise limit the maximum continuous measurement time. Furthermore a lower SNSPD sample temperature is achieved when using the closed-cycle refrigerator (base operating temperature of ~ 3 K).

The initial stages of this thesis work (see Chapter 4) utilised the LiHe based confocal microscope configuration to study SNSPDs. SNSPD devices based on patterned NbN nanowires on MgO substrates (supplied by NICT, Japan) were used in initial photoresponse mapping measurements using the LiHe confocal microscope configuration [5]. Detection efficiency (*DE*) mapping of the 50 % fill factor SNSPD (20 μm x 20 μm area, 100 nm wide wires and period of 200 nm) showed a maximum *DE* of 23.8 % (at λ = 950 nm and 200 Hz dark count rate) with variations in *DE* across the area of the SNSPD. A 10 % fill factor (20 μm x 20 μm area, 100 nm wide wires and a period of 1 μm) SNSPD was specifically fabricated to allow imaging of the individual wires. The wires were clearly imaged and gave a uniform response (*DE* = 28.6 % at λ = 950 nm and 200 Hz dark count rate), with the exception of one 'missing' wire which was electrically connected but was not as responsive as the other nanowires. This would not have been seen without the high optical resolution of this nano-optical technique and shows the advantages it has over broad illumination using fibre-coupling.

The latter stages of this thesis work were to design a miniaturized confocal microscope configuration for use in experiments at telecommunications wavelengths (1310 and 1550 nm) (see Chapter 5). The design was based upon the LiHe low temperature confocal microscope design used in Chapter 4. The simple two-lens system was designed to have a high optical resolution using commercially available and cost effective aspheric lenses. The end of standard single mode telecommunications optical fibre (SMF-28) [6] was used as the aperture in the confocal microscope system. The collimating lens is selected as to maintain efficient coupling of light. The numerical aperture (*NA*) of the collimating lens must closely match that of the optical fibre (*NA* = 0.14). From the Sparrow criterion (equation (2.9)), an objective lens with a high *NA* provides higher resolution. The collimating lens *NA* = 0.15 and a focal length of 18.4 mm. The objective lens had *NA* = 0.68 and a focal length of 3.1 mm. To allow for simple sample exchange moveable optics and a fixed sample was chosen. The optics were mounted in a titanium holder and affixed on top of a commercially available stack of slip-stick X, Y and Z piezoelectric linear positioners. This provided a translation distance of 5 mm in each axis, allowing for focusing and positioning of the focal spot. The achievable full width at half maximum (FWHM) focal spot was 1305 ± 363 nm at λ = 1550 nm, which is larger than the diffraction limit FWHM spot size predicted by the Sparrow criterion [1] (1185 nm). This may be due to the vibrations of the GM coldhead widening the focal spot. Also the Sparrow criterion predicts a focal spot size assuming plane wave illumination whereas in practice a truncated Gaussian beam was used. A piezoelectric X-Y scanner was used to provide precision movement across the area of the SNSPD, covering a range of 30 μm x 30 μm with sub-nanometre resolution [7].

The movement from the LiHe confocal microscope configuration to the miniature confocal microscope configuration provided many improvements and benefits. One major advantage was that electrical grounding issues (encountered in the LiHe setup) were eliminated. This had previously limited the characterisation of the temporal response of SNSPDs. The miniature confocal microscope configuration provided a common electrical ground for all of the electrical connections within the system. This improved low temperature nano-optical testing setup, combined with the use of time correlated single-photon counting (TCSPC) electronics, has provided a robust platform for studying the temporal response across the whole area of the SNSPD with high

resolution [3]. This setup allowed the temporal properties of two constricted SNSPDs to be mapped out. The first constricted SNSPD (*DE* = 0.01 % at λ = 1550 nm and 1 kHz dark count rate) had little variation in the FWHM timing jitter in comparison with the time binning resolution of the TCSPC electronics but showed a variation in the output pulse timing delay between the positions of high and low *DE* of 0 – 50 ps [3]. The second SNSPD was highly constricted (*DE* = 0.005 % at λ = 1550 nm and 1 kHz dark count rate) and showed a larger variation in the output pulse timing delay (0 – 300 ps) between areas of varying *DE*. The FWHM timing jitter of this highly constricted SNSPD varied significantly across the SNSPD (350 – 600 ps). The points of increased Δt correspond to the simultaneous illumination of regions of the device that respond at differing speeds. This means that Δt had contributions from both fast and slow responding regions. The development of a PSPICE [8-10] model of the SNSPD allowed careful fitting to the output voltage pulse shapes at differing regions of the SNSPDs. It was found that the output pulse timing delay was caused by a variation in the hotspot resistance ($R_{hotspot}$). This discovery has provided an important step forward in the understanding of the underlying physics of SNSPDs. These experiments give new insights into the origins of Δt and why non-uniform SNSPDs have poor Δt.

6.2 Extensions of this Work

Integration of the miniature confocal microscope configuration into a low vibration closed-cycle refrigerator to improve the FWHM focal spot size is underway (see Figure 6.1). The low vibration system designed by Dr Michael Tanner uses a Pulse Tube (PT) coldhead to provide cooling without the aid of a mechanical displacer reducing vibrations caused by the coldhead. In addition the PT refrigerator has a remote motor separated from the coldhead to further reduce vibrations. The PT refrigerator is designed to sit on bellows to damp vibrations in the system. Isolating the two cooling stages of the coldhead (40 K and 4 K) from the SNSPD sample by using flexible copper braid reduces (but does not completely remove) vibrations from the coldhead caused by the displacement of helium gas used to cool the system. Measurements (performed by Dr Mike Tanner) using an accelerometer show that the vibrations reduce from ~ 1 g (acceleration due to gravity) using the GM closed cycle refrigerator to < 0.1 g using the

PT closed cycle refrigerator (the actual value is lower than the minimum resolution achievable from the accelerometer). All of these improvements limit vibrations coupling to the miniature confocal microscope configuration. This in turn improves the optical resolution as the focal spot is not widened by vibrations from the closed-cycle refrigerator.

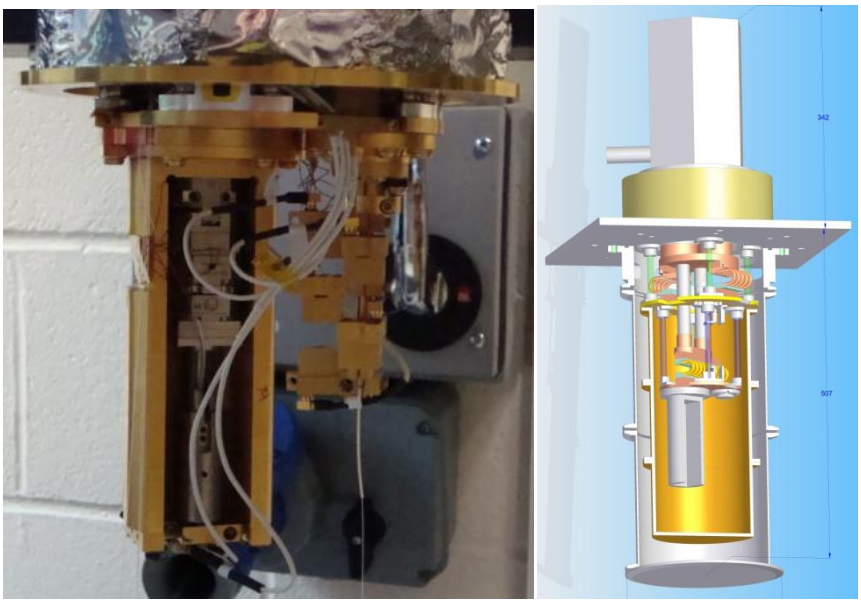

Figure 6.1 – Miniature confocal microscope configuration mounted inside a pulse tube (PT) closed-cycle refrigerator designed and constructed by Dr Michael Tanner. The PT must be mounted pointing downwards for operation, so the miniature confocal microscope configuration is required to be mounted pointing downwards. Left – photograph of the miniature confocal microscope configuration mounted in PT closed-cycle refrigerator. Right – a cut-out design drawing of whole PT refrigerator and miniature confocal microscope configuration.

The variation in $R_{hotspot}$ giving a measurable difference in the output pulse timing delay is an effect that could be potentially exploited to possibly give spectral or photon number information. Measurements at differing photon energies may give a variation in $R_{hotspot}$ allowing photon energy information to be gained. $R_{hotspot}$ may also vary depending upon the number of absorbed photons providing a method for producing a detector with photon number resolving capabilities.

The variation in τ due to a varying $R_{hotspot}$ could also be potentially exploited to extract spatial information for use in imaging. By controlling the localised properties of the

SNSPD, the location of an incident photon striking the SNSPD could be determined from the output pulse timing delay.

One possible method of achieving this is varying the width of the nanowire (see Figure 6.2).

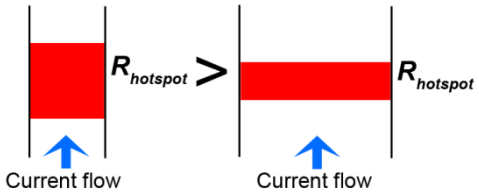

Figure 6.2 – Varying the width of a superconducting nanowire to vary $R_{hotspot}$. The nanowire on the left is narrower than the nanowire on the right, thus having a higher value of $R_{hotspot}$.

For this to be practical, next generation device designs will have to have a large τ variation without compromising key performance parameters such as *DE* and Δt. Varying the width of the nanowire will result in variations in *DE* and poor Δt. Both of these new applications depend crucially on the mechanism of hotspot formation and evolution. Yang *et al* [11] have shown that $R_{hotspot}(t)$ is driven by Joule heating due to the bias current. Understanding this effect is crucial to the realisation of new types of SNSPD devices.

6.3 Conclusion

Significant experimental advances have been made during this thesis work. Initial nano-optical studies of SNSPDs were carried out using a liquid helium confocal microscope configuration at visible and near infrared wavelengths. A state-of-the-art high resolution miniature confocal microscope system for use at telecommunications wavelengths was developed at Heriot-Watt University. This setup allows greater understanding of the underlying device physics of SNSPDs to be gained. The system is used to study the properties (*DE*, Δt and τ) of SNSPDs at localised areas across the whole device area at telecommunication wavelengths. As a result significant insights have been gained into the underlying device physics of SNSPDs. These studies open the pathway to the development of next generation SNSPDs with improved characteristics.

6.4 Chapter 6 References

1. C. M. Sparrow, *On spectroscopic resolving power.* The Astrophysical Journal, 1916. **44**: p. 76.
2. A. Hogele, S. Seidl, M. Kroner, K. Karrai, C. Schulhauser, O. Sqalli, J. Scrimgeour, and R.J. Warburton, *Fiber-based confocal microscope for cryogenic spectroscopy.* Review of Scientific Instruments, 2008. **79**(2): p. 023709.
3. J. A. O'Connor, M.G. Tanner, C.M. Natarajan, G.S. Buller, R.J. Warburton, S. Miki, Z. Wang, S.W. Nam, and R.H. Hadfield, *Spatial dependence of output pulse delay in a niobium nitride nanowire superconducting single-photon detector.* Applied Physics Letters, 2011. **98**(20): p. 201116-3.
4. R. Radebaugh, *Refrigeration for superconductors.* Proceedings of the IEEE, 2004. **92**(10): p. 1719-1734.
5. J. A. O'Connor, P.A. Dalgarno, M.G. Tanner, R.J. Warburton, R.H. Hadfield, B. Baek, S.W. Nam, S. Miki, Z. Wang, and M. Sasaki, *Nano-optical studies of superconducting nanowire single photon detector.* Quantum Communication and Quantum Networking, O. Akan, et al., Editors. 2009, Springer Berlin Heidelberg. p. 158-166.
6. *SMF-28e optical fiber, www.corning.com.*
7. *Attocube 100 series xy scanner http://www.attocube.com/nanoPOSITIONING/ANSxy100/Specifications_ANSxy100.pdf (Date Accessed 9th February 2011).*
8. L. W. Nagel and D.O. Pederson, *SPICE (Simulation Program with Integrated Circuit Emphasis), Memorandum No. ERL-M382.* University of California, Berkeley, 1973.
9. R. H. Hadfield, A.J. Miller, S.W. Nam, R.L. Kautz, and R.E. Schwall, *Low-frequency phase locking in high-inductance superconducting nanowires.* Applied Physics Letters, 2005. **87**(20): p. 203505.
10. A. J. Kerman, E.A. Dauler, W.E. Keicher, J.K.W. Yang, K.K. Berggren, G. Gol'tsman, and B. Voronov, *Kinetic-inductance-limited reset time of superconducting nanowire photon counters.* Applied Physics Letters, 2006. **88**(11): p. 111116.

11. J. K. W. Yang, A.J. Kerman, E.A. Dauler, V. Anant, K.M. Rosfjord, and K.K. Berggren, *Modeling the electrical and thermal response of superconducting nanowire single-photon detectors.* IEEE Transactions on Applied Superconductivity, 2007. **17**(2): p. 581-585.

Appendix I Simulation of Polarisation Dependent Absorption in SPSNDs and Comparison with Experimental Results

Simulations of the absorption (*A*) of light into a 4 nm thick and 100 nm wide niobium nitride (NbN) nanowire superconducting single-photon detector (SNSPD) at both orthogonal polarisation states, were carried out on our behalf by Vikas Anant from Massachusetts Institute of Technology (MIT), USA. The simulation method was a finite element analysis using COMSOL [1]. Both a 50 % (100 nm wide wires and 200 nm pitch) and a 10 % (100 nm wide wires and 1 μm pitch) fill factor SNSPD were simulated.

Refractive Indices Used

Wavelength (nm)	*n* (NbN)	*k* (NbN)	*n* (Sapphire substrate)
470	2.2	2.77	1.78
900	3.6	4.52	1.76
1550	5.23	5.82	1.75

Table AI.1 - The input material parameters for the simulation of absorption in SNSPDs.

Simulation Results

Fill Factor	Wavelength (nm)	*A* parallel (%)	*A* perpendicular (%)	*A* parallel / *A* perpendicular
50 %	470	13.0	13.8	0.942
50 %	900	17.3	15.8	1.096
50 %	1550	18.7	9.9	1.890
10 %	470	2.2	2.8	0.794
10 %	900	3.4	3.7	0.915
10 %	1550	4.2	1.9	2.191

Table AI.2 - Simulation results of polarisation dependence of the absorption of light by 50 % and 10 % fill factor SNSPDs. λ = 470 nm, 900 nm and 1550 nm were simulated.

Comparison with Experimental Results

DE of a fibre-coupled 50 % fill factor SNSPD was measured at 830, 1310 and 1550 nm. *DE* was measured at both orthogonal polarisation states, using a fibre based polariser. The fibre based polariser does not determine explicitly polarisation state the incident light is in. By maximising or minimising the count rate one of the orthogonal polarisation states is selected. For comparison with simulations (see Table AI.1) the ratio of high to low polarisation states are compared. The following table (Table AI.2) shows *DE* at both polarisation states along with the high to low ratios of the 50 % fill factor SNSPD. The high to low absorption ratio from the simulations is also included.

Comparison of Experimental and Simulated Polarisation Dependence

Wavelength (nm)	High *DE* (%)	Low *DE* (%)	High *DE* / Low *DE*	*A* High / *A* Low
470	N/A	N/A	N/A	1.062
830	9.6	8.7	1.103	N/A
900	N/A	N/A	N/A	1.096
1310	3.9	2.6	1.5	1.554
1550	1.8	0.85	2.117	1.889

Table AI.3 – A comparison of experimental and simulated polarisation dependence measurements of 50 % fill factor SNSPD with varying wavelength.

Plotting the results (see Figure AI.1) from the above table shows that the experimental results of polarisation dependence closely match the simulations. The variation between the experimental and simulated results is most likely due to a variation in the input parameters (see Tabl), specifically the *n* and *k* values of the substrate. The simulation uses values for sapphire while the measured SNSPD used MgO as the substrate.

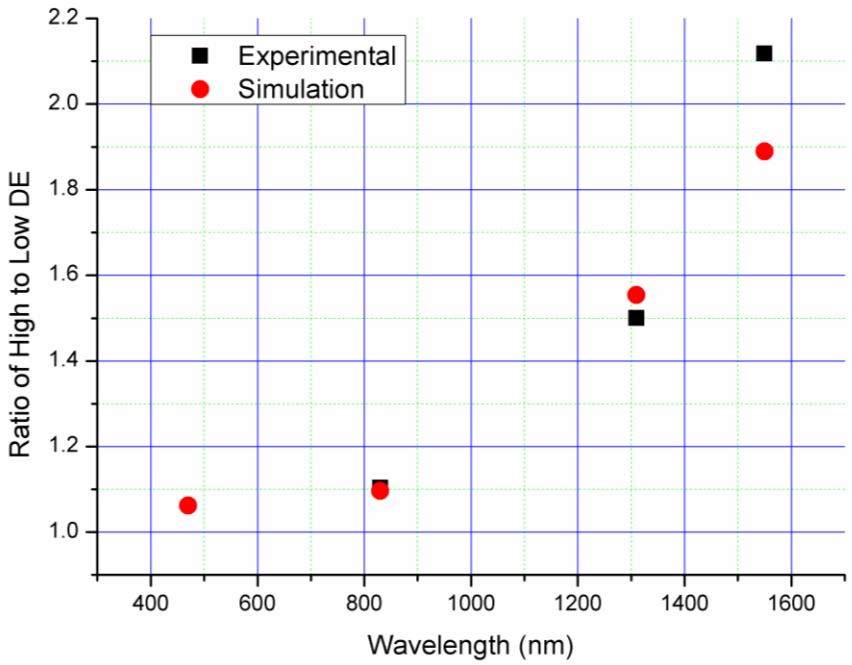

Figure AI.1 – A comparison of the experimental and simulated polarisation dependence of a 50 % fill factor SNSPD with varying wavelength.

Wavelength (nm)	High *DE* (%)	Low *DE* (%)	High *DE* / Low *DE*	*A* High / *A* Low
470	N/A	N/A	N/A	1.27
830	0.098	0.094	1.042	N/A
900	N/A	N/A	N/A	1.08
1310	0.058	0.054	1.074	N/A
1550	1.06	0.943	1.124	2.191

Table AI.4 – A comparison of experimental and simulated polarisation dependence measurements of a 10 % fill factor SNSPD with varying wavelength.

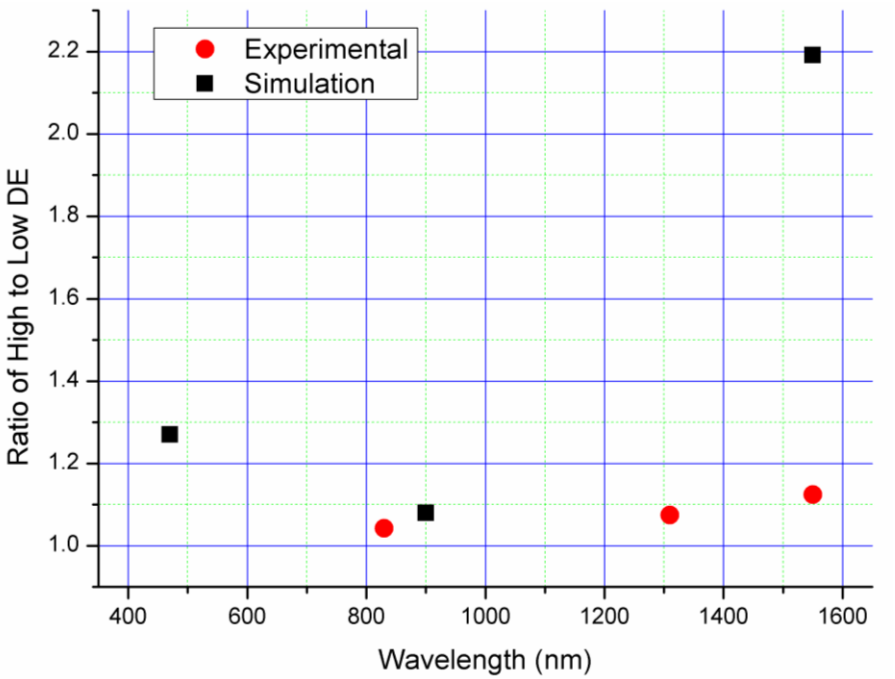

Figure AI.2 – A comparison of the experimental and simulated polarisation dependence of a 10 % fill factor SNSPD with varying wavelength.

The polarisation dependence measurements for the 10 % fill factor SNSPD (see Figure AI.2) agree qualitatively but not quantitatively with the simulation results. This discrepancy is possibly due to the input parameters of the materials in the simulations as described earlier. The difference is also possibly due to the fact a focused spot of light was used in the measurements rather than broad illumination from the end of an optical fibre.

Appendix II Summary of SNSPD Characteristics from Chapter 5

A list of properties for both SNSPDs (constricted and highly constricted) measured in Chapter 5 is given here. The measurements were carried out in the miniature confocal microscope configuration in a GM closed-cycle refrigerator at T ~ 3K. The key properties shown in Table AII.1 are the critical current (I_c), constriction factor (C), detection efficiency (DE) at λ = 1550 nm, minimum timing jitter (Δt), range of output pulse timing delay (τ) and the device area.

Property	Constricted SNSPD	Highly Constricted SNSPD
I_c (μA)	12.0	6.5
C	0.35	0.30
DE at λ = 1550 nm (%)	0.010	0.005
Δt (ps)	140	300
Range of τ (ps)	0 – 50	0 – 300
Area (μm^2)	20 x 20	20 x 20

Table AII.1 – A summary of device properties for the constricted and highly constricted SNSPDs measured in Chapter 5.

Appendix References

1. V. Anant, A.J. Kerman, E.A. Dauler, J.K.W. Yang, K.M. Rosfjord, and K.K. Berggren, *Optical properties of superconducting nanowire single-photon detectors.* Optics Express, 2008. 16(14): p. 10750-10761.